Revealing Deformation and Damage Micromechanisms in Composites by X-ray Computed Tomography and Digital Volume Correlation

A Dissertation

Presented to

the faculty of the School of Engineering and Applied Science

University of Virginia

in partial fulfillment
of the requirements for the degree

Doctor of Philosophy

by

Brendan P Croom

May 2019

APPROVAL SHEET

This Dissertation
is submitted in partial fulfillment of the requirements
for the degree of
Doctor of Philosophy

Author Signature: ______________________

This Dissertation has been read and approved by the examining committee:

Advisor: Xiaodong Li, PhD

Committee Member: Devin Harris, PhD

Committee Member: Helena Jin, PhD

Committee Member: Osman Ozbulut, PhD

Committee Member: Baoxing Xu, PhD

Committee Member: ______________________

Accepted for the School of Engineering and Applied Science:

Craig H. Benson, School of Engineering and Applied Science

May 2019

Abstract

The mechanical performance of composite materials is intricately related to the arrangement of reinforcing constituents and defects within a matrix material. In particle-reinforced syntactic foam composites, as well as fiber-reinforced polymer- and ceramic-matrix composites, damage tends to propagate rapidly from pores, cracks or other intrinsic weak points in the material, such that composites express strong flaw sensitivity. As conventional, surface-based experimental measurement techniques cannot access these internal features, it has been challenging to precisely quantify the influence of defects on the overall mechanical response of the composite. To address this limitation, a new 3D, quantitative experimental technique based on *in situ* X-ray Computed Tomography (XCT) mechanical testing coupled with Digital Volume Correlation (DVC) has been developed. The *in situ* XCT volumetric images capture the composite's original microstructure as well as damage features that develop under mechanical loading, while DVC provides local deformation measurements in the vicinity of these key microstructural features. In this way, the coupled *in situ* XCT/DVC approach can uniquely establish the influence of microstructural features on the damage behavior.

This dissertation develops the *in situ* XCT/DVC technique to study the damage behavior in syntactic foams, polymer-matrix composites and ceramic matrix composites. First, the accuracy of DVC in these materials is validated experimentally, numerically and theoretically, since the microstructures of these materials violate commonly held requirements for accurate DVC measurement. Next, this approach is applied to study the damage mechanisms in elastomer-matrix syntactic foams with glass microballoon (GMB) reinforcement. Through quantitative assessment of the original GMB arrangement, measurements of the deformed GMB shapes, and the DVC strain fields, we show that the damage is strongly influenced by the original

arrangement of GMBs. Collapse is favored in tightly-packed, transverse “chains” of GMBs, such that a striated strain pattern develops in the DVC measurement. Further experiments showed that this trend held for syntactic foams over a range of GMB volume fractions, suggesting that damage is explained not only by the global volume fraction of reinforcement but also by the particle clustering. Next, *in situ* experiments on stir-processed polymer matrix composites identified that local metallic particles controlled the compression response and onset of buckling. Finally, expanding plug tests of braided ceramic matrix composite tubes revealed that damage initiated at tow overlaps, and was influenced by irregular spacing between adjacent tows. These experiments demonstrate the ability of *in situ* XCT/DVC techniques to capture the effects of local microstructure on damage in composites, and offer new routes to validate numerical and analytical models of composite performance.

Table of Contents

Acknowledgements

First, I must thank Prof. Xiaodong Li for being an exceptional advisor. Your patient mentorship and optimism have been integral to my graduation, and have made me a better person and scholar. I also thank my committee members, Dr. Helena Jin, and Profs. Devin Harris, Osman Ozbulut and Baoxing Xu. In particular, Dr. Jin has become a close mentor, and has warmly welcomed me into the Society of Experimental Mechanics.

The many members of Prof. Li's laboratory have served as an inexhaustible resource of creativity, entertainment and support. Formally, my name appears on various papers with Jamison Bartlett, Kenneth Brown, Clifton Bumgardner, Diana Burden, Dr. Zan Gao, Michael Heim, Dr. Yellapu Murty, Yosyp Schwab, Ningning Song, Dr. Liwen Zhang, Yunya Zhang and Dr. Jiadeng Zhu; but my friendships with all are equally imprinted on my academic and personal growth.

Throughout this journey, I have been able to count on a large and loving network of family and friends to support my academic endeavors. My mother, Sharon Sengelaub, is the strongest woman I know, and my father, Rusty Croom, has been steadfast in his support of my ambitions. I'd also like to thank Jeremy and Hilary Croom, as well as the louder half of my family – Hari, Malini and Sree Sarma – for knowing when to offer support, reassurance or distraction from my studies. And dearest to me, I thank my partner in the greatest experiment of all, Mallika Sarma. She inspires me to dream of stars, while reminding me to stay grounded.

Finally, I acknowledge funding from numerous sources. My education was generously supported by the National Science Foundation (NSF GFRP, DGE-1842490), the Virginia Space Grant Consortium, as well as various University of Virginia School of Engineering and Applied Science sources. Specific research activities in this dissertation were funded by Sandia National

Laboratories (Chapters 2-4); the National Science Foundation (CMMI-1363468, 1358673 and 1418696) and Ford Motor Company (Chapter 5); and Westinghouse Electric Company (Chapter 6). Special thanks are given to Prof. Jingjing Li of Pennsylvania State University (Chapter 5) and General Atomics (Chapter 6) for providing materials. Richard White, Diane Dickie and the Nanoscale Materials Characterization Facility have provided expert training and assistance with X-ray Computed Tomography and microscopy equipment at the University of Virginia. Additional research activities not reported in this dissertation have been funded by Department of Energy (NEUP, Project 17-13080) and the Commonwealth Center for Advanced Manufacturing, and has benefitted from beamline access at the Advanced Photon Source at Argonne National Laboratory and National Synchrotron Light Source II at Brookhaven National Laboratory. Sandia National Laboratories is a multimission laboratory managed and operated by National Technology and Engineering Solutions of Sandia, LLC., a wholly owned subsidiary of Honeywell International, Inc., for the U.S. Department of Energy's National Nuclear Security Administration under contract DE-NA-0003525. This dissertation describes objective technical results and analysis. Any subjective views or opinions that might be expressed in the dissertation do not necessarily represent the views of the U.S. Department of Energy or the United States Government.

List of Figures

List of Tables

Chapter 1: Introduction

1. The role of microstructural variation on the performance of composites

By carefully engineering two or more unique constituents into a single material, composites can achieve unrivaled mechanical properties. Carbon-fiber reinforced polymer matrix composites have among the highest strength-to-weight ratio of bulk materials, and the addition of SiC fibers to a brittle SiC matrix creates a strong composite that can operate sustainably at temperatures above 1200°C. However, in these and other composites, damage and failure can propagate rapidly from local defects. Indeed, the performance of these materials exhibit very large statistical variation between specimens and also have pronounced size effects [1,2], which are both related to the statistical likelihood of flaws being present in the material. This is manifested in relatively low fracture toughness compared to other high-performance engineering materials such as steels, although these properties are better than the composite's individual constituents: $K_{IC} \approx 30\ MPa\sqrt{m}$ for glass-fiber composites, $K_{IC} \approx 20\ MPa\sqrt{m}$ for ceramic matrix composites, and $K_{IC} > 150\ MPa\sqrt{m}$ for some steels [3–5]. In other words, microstructural variation is the primary source of the deviation in performance between composite specimens.

In practical terms, this means that the performance of composites statistically varies between specimens, and structures must be "over-designed" to account for this variability. This scenario is commonly encountered in ceramic-matrix composites (CMCs), polymer-matrix composites (PMCs) and syntactic foams, which serve as the three model materials for the proposed research. For example, it has been shown that CMCs exhibit strong statistical variation in mechanical strength, which is often modeled using Weibull statistics [2]. Recent flexural testing on braided CMCs for nuclear fuel cladding applications have revealed standard deviations of up to 10% of the average tensile strength [6]. Using the reported statistical distribution, a design stress of 45% of the average strength would still produce failure in 1 in 1000 components. This requires CMC and other composite components to incorporate large factors of safety in the design, resulting in heavier, more expensive, less efficient and otherwise lower performance CMC components.

Some sources of the variation are intrinsic to the composite, such as random fluctuations in reinforcement strength and flaw distributions in the matrix. On the other hand, some of the variation can also be attributed to irregular arrangement of reinforcement within the matrix or other "controllable" microstructural defects. Continuing the example of CMCs, full-field strain measurements have shown that irregular tow spacing can locally amplify strains and microcrack density [7–9], and recent simulations have shown that randomness in tow placement reduces strength by up to 10% [10]. Such features could reasonably be controlled or monitored through manufacturing quality control processes, thereby condensing the statistical variation in measured material properties. This would allow lighter, more efficient and more reliable composite structures and would realize substantial economic benefit.

To help realize this goal, the aim of this dissertation is to develop new 3D quantitative experimental tools to directly assess the role of microstructural defects on the properties. Such data can characterize the flaw population and (more importantly) its effect on deformation, damage and failure. Conventional experimental tools cannot directly resolve the effect of these *internal* defects on the deformation and damage behavior. This data is essential to calibrating continuum-scale damage tools, validating micromechanics models, and designing stronger composites.

This dissertation presents new *in situ* X-ray Computed Tomography (XCT) mechanical testing techniques with coupled image analysis and Digital Volume Correlation (DVC) as a tool to reveal quantitative relationships between microstructure, deformation, and damage within three types of model materials, described below. XCT reconstructs a sample's interior structure from a series of 2D radiographic projections acquired at many orientations [11], and provides high-resolution 3D images (tomograms) of the interior structure of engineering materials. Typical spatial resolutions range from <1 μm to 10 μm, which compare favorably with the dimensions of key composite features and damage structures. Correlation of *in situ* tomograms using DVC algorithms provides high-resolution, full-field, local and quantitative deformation, strain and damage measurements, which can be directly superimposed on the underlying microstructural images to establish high-fidelity microstructure-deformation-damage relationships. These measurements reveal the source of variation in mechanical performance, and therefore support the design of higher performance and more reliable composite structures.

2. Overview of model materials

The damage micromechanisms of three model materials are studied with *in situ* XCT mechanical testing. These materials include a syntactic foam, a polymer matrix composite (PMC), and a ceramic matrix composite (CMC). Each material exhibits very unique microstructures, mechanical properties, and damage mechanisms, so they serve as interesting case studies for the newly developed *in situ* XCT / DVC techniques.

The first model material in this dissertation is an elastomer-matrix syntactic foam (Fig. 1.1) filled with hollow glass microballoons (GMBs), which is being developed for use as an electronic packing material. The stiff GMBs are designed to reinforce the soft matrix, but also crush at high stress. In this way, the resulting syntactic foam achieves high stiffness and energy absorption at low density. Additionally, the low thermal expansion and superior dielectric properties of the GMBs make a unique soft composite with ideal properties for a packaging material. While the damage mechanisms of syntactic foams with rigid thermoset matrices (*e.g.*, epoxy or vinyl ester) have been studied, the effect of a hyperelastic and soft elastomer matrix on the damage behavior is unknown. Due to the very low compliance, the elastomer matrix is expected to change the damage behavior. Particular interest is devoted to the role of irregular GMB clustering on the damage mechanisms, which is shown to significantly alter the strength and ductility of other types of syntactic foams [12]. As evident in Fig. 1.1, the GMBs are not homogeneously dispersed, but tend to agglomerate in chains of closely-spaced GMBs.

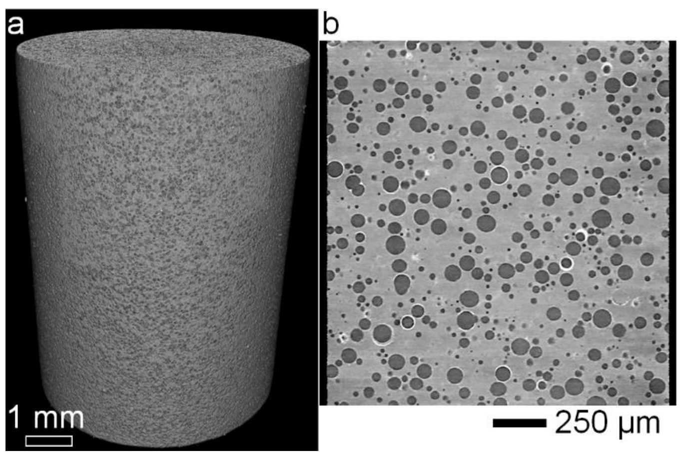

Fig. 1.1. Structure of elastomer matrix syntactic foams. (a) 3D rendering of syntactic foam specimen, and (b) XCT cross-section showing hollow GMBs embedded in an elastomer matrix.

The second model material is an injection-molded, chopped-fiber PMC material that has been joined to an aluminum alloy sheet using a friction-stir blind rivet (FSBR) technique [13,14] (Fig. 1.2). FSBR is a new joining technique that has been developed to support automobile lightweighting initiatives. This one-sided joining process is compatible with dissimilar materials, and operates by pushing a rotating blind rivet tool through the two workpieces to form a lap joint; the particular FSBR joint in question consists of a PMC top sheet joined to an aluminum alloy bottom sheet. Friction from the rotating rivet softens the composite and metal sheets, thereby creating a “stir zone” with a distorted local fiber arrangement. Severe plastic deformation in the metal sheet can also embed metal fragments within the stir zone. Given that the stir zone experiences the highest stresses such that failure in the lap joint emanates from the rivet hole, it is imperative to understand how the altered microstructure responds to mechanical loads. *In situ* XCT and DVC techniques can uniquely probe the internal response of the stir zone, in contrast to conventional surface-based techniques.

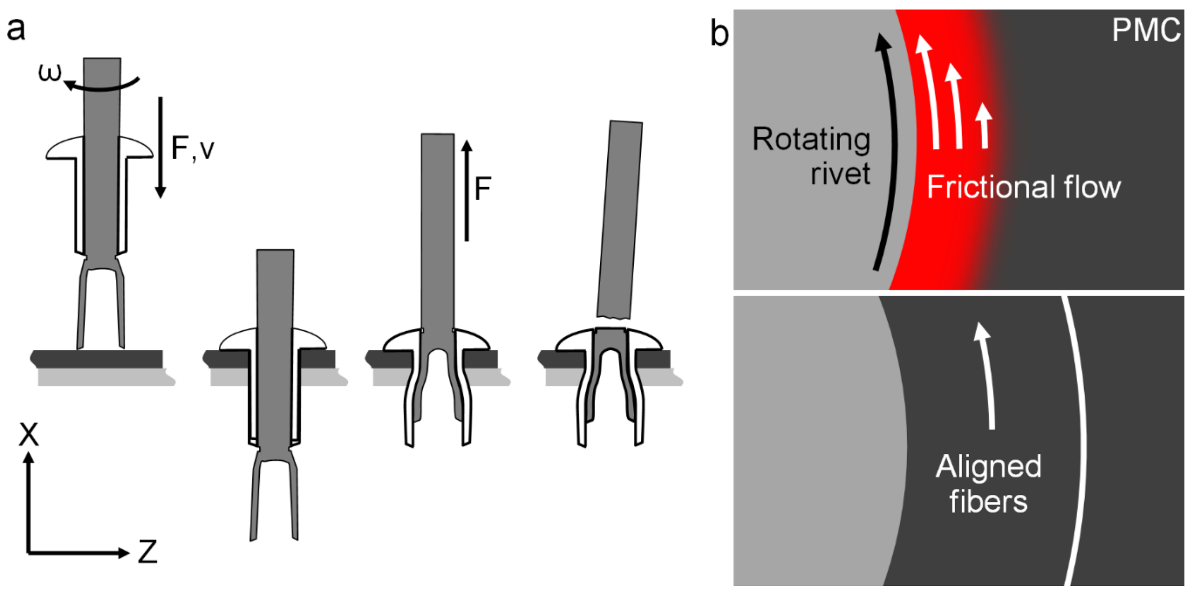

Fig. 1.2. Friction stir blind riveting process. (a) Manufacturing sequence, and (b) formation mechanism of stir zone.

The final model material is a braided CMC tube that is being developed for accident-tolerant nuclear fuel cladding system. The CMC consists of tows of high-purity SiC fibers that are braided around a mandrel; the fibers are then coated with a pyrolytic carbon interphase, and then the preform is densified through chemical vapor infiltration of a SiC matrix. This unique architecture promotes crack bridging and fiber pullout, which help to toughen the composite compared to a brittle monolithic ceramic. The cladding tube features a triaxial braid with balanced axial and hoop properties, with fibers oriented at 0° as well as ±60° from the axis. The final tube geometry has an outer radius of 5.5 mm and a wall thickness of 1.2 mm.

Prior to operation, fuel pellets and pressurized gas are sealed within the cladding. Once inserted into the nuclear reactor core, the cladding experiences temperature gradients through the wall thickness, internal pressurization, and radiation-induced swelling. As a result, one of the primary loading conditions is circumferential. In this dissertation, DVC is employed to study the damage behavior caused by hoop-direction loading. The hoop stress is generated using a novel expanding plug test fixture in which a nearly-incompressible elastomer insert is axially compressed; the plug swells in the radial direction and pressurizes the specimen [15].

3. In situ XCT mechanical testing experiments

The unique ability to resolve the internal microstructure of composites has made XCT an appealing (yet challenging) technique to perform *in situ* mechanical testing. With spatial resolution on the order of 1 μm, the XCT technique can comfortably resolve key microstructural (*e.g.*, pores, fibers, and other reinforcement features) and damage (cracks, fiber kinking, buckling) features. Modern synchrotron X-ray sources can capture dynamic composite phenomena with >1 Hz tomography [16–18] (Fig. 1.3), and thus are able to “freeze” transient damage events in 3D. Slower laboratory XCT systems also exhibit adequate resolution to detect localized damage, allowing the study of quasi-static events. Many examples of this technique to study the damage mechanisms of composites are summarized in a recent review article [19], which demonstrate the viability of *in situ* studies of mechanical behavior [20–22], composite processing [23–26], and environmental exposure [27].

The central challenges for performing *in situ* XCT testing of composites relate to (a) obtaining adequate contrast, (b) ensuring test fixture compatibility with the XCT system, and (c) applying controlled loads. These factors must be considered for the design of a successful *in situ* experiment.

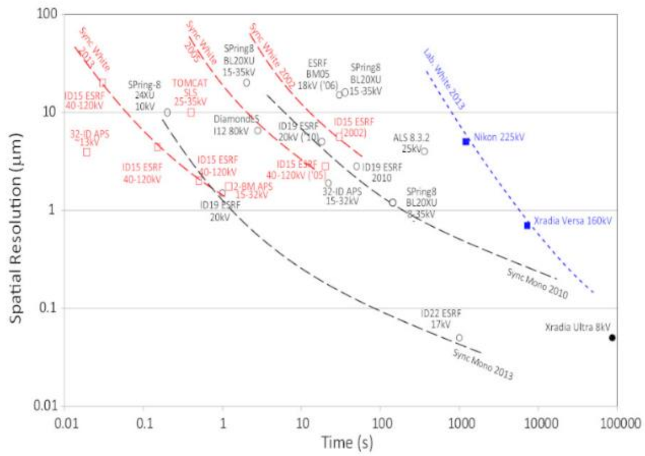

Fig. 1.3. Comparison of X-ray Computed Tomography acquisition time and spatial resolution with laboratory (blue), and "white" and "monochromatic" synchrotron X-ray sources (red and black, respectively). Adapted from [11].

Contrast in X-ray tomography is proportional to the X-ray attenuation in each voxel, which describes the ratio between the incident and transmitted X-ray flux. X-ray attenuation within a sample is governed by Beer's Law

$$I = I_0 \exp(-\mu x) \tag{1.1}$$

which shows the transmitted X-ray intensity I as a function of the initial intensity I_0, the positive attenuation constant μ, and specimen thickness x. The resulting X-ray contrast is therefore directly attributed to variation in μ between constituents; indeed, the reconstruction algorithm aims to recover μ for every voxel in the tomogram. The attenuation constant scales proportionally to the atomic number Z and the material density, and also depends nonlinearly on the X-ray photon energy.

The attenuation constants for constituent materials relevant to the model composite systems have been compiled from National Institute of Standards and Technology reference tables [28], and are reported in Fig. 1.4. Clearly, the limited difference in density and composition between reinforcement and matrix materials results in poor contrast for both carbon-fiber reinforced polymer, and SiC-fiber reinforced SiC matrix composites (syntactic foams, which primarily consist of air and PDMS matrix, do not have this constraint). To overcome this, long scan times with a large number of projections are required to achieve adequate signal to noise ratios. Especially for laboratory XCT systems, small distances between the X-ray source and detector are required for good image quality.

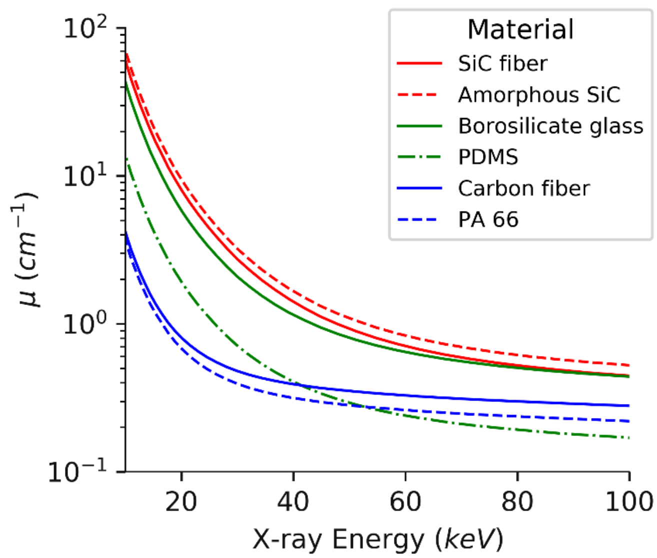

Fig. 1.4. X-ray attenuation constants for relevant constituents in the studied composite materials. Note that the X-ray attenuation constant for air is $\mu^{air} \approx 10^{-3}$ over this range of photon energies. Data from Ref. [28]

As a consequence of the low contrast between reinforcement and matrix phases in composites, any XCT loading device must be designed to carefully fit within the small distance between the X-ray source and detector, and also not obstruct the X-ray transmission. For laboratory XCT systems, this distance is on the order of 50 mm or less, but in some cases can be less than 25 mm [29,30]. Additionally, the stage must permit the maximum transmission of the X-rays through the sample, and have uniform attenuation from all angles. This minimizes scan time and also eliminates "streaking" artifacts due to irregular attenuation outside the field of view.

Finally, as with any mechanical testing device, the loading stage should apply well-characterized loads and deformation to the specimen. While conventional loading devices include large, stiff and X-ray opaque components to ensure good alignment and frame stiffness, these are not compatible with the XCT equipment.

With these constraints in mind, several custom loading stages were designed to perform *in situ* XCT mechanical testing of composite samples (Fig. 1.5). Each loading device included an X-ray transparent polycarbonate or Nylon tube to transfer the load between the upper and lower grips, a miniature tension-compression load cell, and a manually-controlled screw to displace the top of the sample. The grips and other internal components were designed with a tight tolerance to the polymer tube, which allowed them to slide freely while maintaining strong axial alignment. This design was comparable to others described in the literature [31,32]. Several variations of the stage were developed to accommodate different loading modalities, specimen geometries and maximum force requirements.

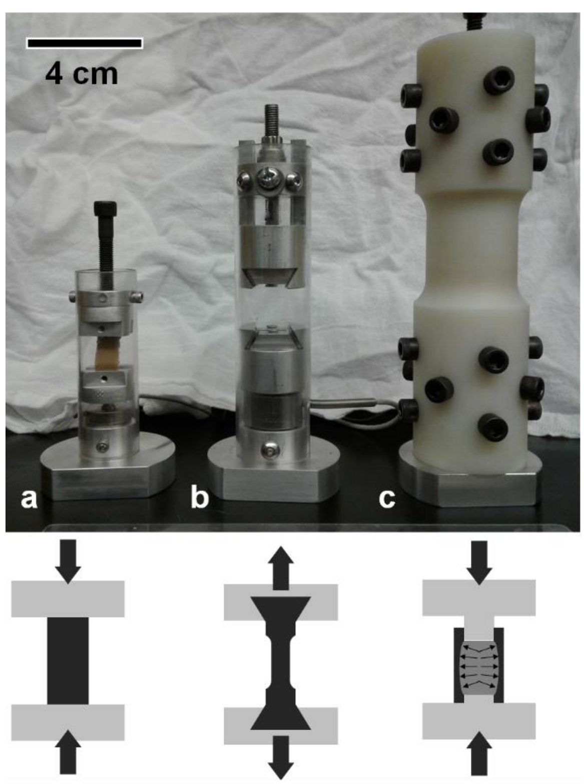

Fig. 1.5. Custom XCT loading stages designed for this dissertation. Stages are designed to apply (a) uniaxial compression, (b) uniaxial tension, and (c) expanding plug (hoop stress) to various types of specimens.

4. 3D image-based displacement measurement

The high-resolution 3D images acquired by *in situ* XCT encode all deformation and damage within the material, so it is intuitive to process the images to measure the full-field displacement of the material. Several strategies have been proposed to achieve this, including *particle tracking* and *digital volume correlation*.

Particle tracking (PT) algorithms operate by identifying high-contrast features with unique geometry and size in the undeformed state, registering the same particles in the deformed image, and computing the displacement between the two states. Strain fields can be evaluated from the change in spacing between particles. These techniques have been widely adopted in biological applications [33–36], and more recently in the experimental mechanics of solid materials [37–40].

By nature of the small deformations in many engineering materials, exceptional measurement sensitivity is demanded of PT algorithms, such that very small displacements on the order of $u < 0.1\ voxels$ and strains on the order of $\varepsilon < 0.01$ can be accurately resolved. However, the accuracy of these techniques is limited, and strongly depends on the quality of microstructural markers. Recent error analysis has shown that an optimized particle tracking technique can achieve standard deviation displacement error of $\sigma_u = 0.10\ voxels$ for typically-sized particles with a radius of 3 $voxels$, and $\sigma_u = 0.03\ voxels$ for unusually large particles with a radius of 9 $voxels$ [41]. Strain measurement scales inversely with the spacing between adjacent particles, and sufficient accuracy is therefore restricted to sparse patterns. Finally, the accuracy of all particle tracking measurements is observed to be strongly sensitive to the specific tracking algorithm [33].

In contrast, DVC operates by computing the motion of an *ensemble* of voxels defined by a cubic subvolume. Each subvolume is sized to contain many high-contrast features (referred to as "speckles" in DVC nomenclature), and therefore overcomes many of the limitations of particle tracking algorithms. Specifically, by effectively tracking a large cluster of particles, superior displacement and strain accuracies are achieved in contrast to registration of individual particles. Displacement and strain measurement precision routinely exceed $\sigma_u < 0.1\ voxels$ and $\sigma_\varepsilon < 0.01$ even for materials with small and irregular particles [42]; similar achievements could not be achieved via PT algorithms. As a result, it has become much more widely adopted within the mechanics community [42–44].

5. *Principles of digital volume correlation*

DVC [45] extends the popular two-dimensional Digital Image Correlation (DIC) [46,47] approach into three dimensions, and uses correlation algorithms to quantitatively track the full-field displacement between the "reference" and "deformed" states. Displacement is measured in the local sense by dividing the reference tomogram into subvolumes (typically cubes with sides of 10-40 voxels in length), and computing the cross-correlation of each subvolume with the deformed image. As the aim of the algorithm is to register the displacement of each voxel from the reference subvolume to the deformed state, the quality of this match can be assessed using a least-squares correlation between the two subvolumes,

$$\chi_{LS} = \sum_{x \in S} \Big(G\big(\boldsymbol{x} + \boldsymbol{u}(\boldsymbol{x})\big) - F(\boldsymbol{x}) \Big)^2 \tag{1.2}$$

where F and G correspond to the reference and deformed images, $\boldsymbol{x}$ represents the local coordinates within the reference subvolume S, and $\boldsymbol{u}(\boldsymbol{x})$ is the displacement field. The correlation is minimized when the displacement field is found (Fig. 1.6a); subvoxel accuracy is achieved using higher-order image interpolation and efficient numerical schemes such as Gauss-Newton, etc.

Typically, the deformation is linearized within each subvolume to reduce the number of parameters to be solved and ensure the problem is appropriately overdetermined,

$$\boldsymbol{u}(\boldsymbol{x}) \approx \boldsymbol{u}_{\boldsymbol{0}} + \nabla\boldsymbol{u}(\boldsymbol{x} - \boldsymbol{x}_{\boldsymbol{0}}) \tag{1.3}$$

where $\boldsymbol{u}_{\boldsymbol{0}}$ captures the rigid body translation at the subvolume's center $\boldsymbol{x}_{\boldsymbol{0}}$; and $\nabla\boldsymbol{u}$ captures the deformation gradients throughout the subvolume due to deformation and rotation. This formulation provides convenient access to the material strains in each subvolume, *i.e.*, from $\nabla\boldsymbol{u}$. By repeating this process over all subvolumes, the full-field displacement and strain is found.

Error in the DVC displacement and strain measurements is introduced during both tomogram acquisition and post-processing (correlation). Most prominently, distortion due to the cone-beam geometry and thermal drift of the X-ray source can introduce significant strain error on the order of $\delta\varepsilon > 0.005$ [48]; however, these errors can be ameliorated by accounting for the nonlinear distortion and using appropriate scan recipes [49,50]. Other sources of error due to image noise, interpolation schemes and the correlation algorithm have been extensively characterized for conventional DIC, and are described in detail in [51].

5.1. Inferior speckle patterns and DVC accuracy

In DVC, measurement accuracy depends strongly on the quality of the speckle pattern, which carries all information about the specimen deformation. While studies specific to the role of speckle patterns on the accuracy of DVC are limited (indeed, this is a key objective of the current dissertation), there exists a vast literature dedicated to evaluating the role of speckle patterns on the effectiveness of the analogous 2D DIC technique. In summary, these analyses have shown that speckles should be high-contrast, uniformly sized (typically 3 $voxels$ in diameter), random, durable, and isotropic [52–56]. For conventional surface-based DIC applications, appropriate patterns can readily be applied by a number of techniques, including spray paint, airbrush, transfer printing, or stencil [57]. Colloquially, these requirements ensure that each subset contains a unique and sufficiently high information content, such that the correlation algorithm can precisely locate the subset in the deformed image [58]. In fact, the speckle pattern is the most important tool to improve the DIC/DVC measurement quality measurement.

However, a key distinction between the preparation of surface-based and volumetric test specimens is that it is substantially more challenging (or even undesirable) to create high-quality 3D speckle patterns [43]. This limitation is particularly pronounced in composites, whose microstructures tend to violate these stipulations (Fig. 1.6b-d). In particular, the fiber-reinforced composites tend to have *anisotropic* microstructures with *low contrast*, whereas syntactic foams have *fragile* microstructures.

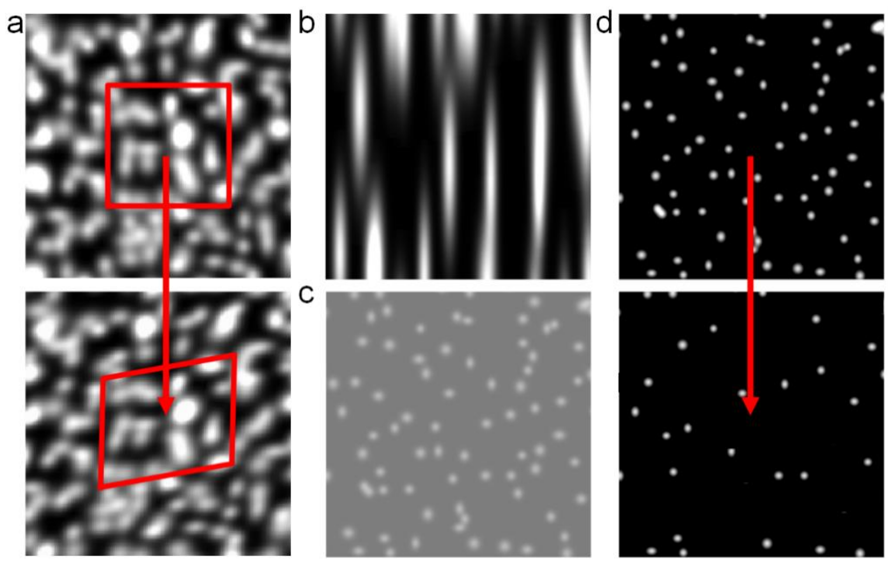

Fig. 1.6. High-quality and deficient synthetic speckle patterns. (a) High-quality DIC pattern enables good subset registration. (b-d) Low-quality DIC patterns due to anisotropy, low contrast and fragility. All images are generated artificially.

There is no good way to overcome this limitation. One commonly used approach is to embed high-contrast particles into the microstructure during the manufacturing process, such as metallic particles in a polymer-matrix composite [59]. The addition of a significant fraction of high-contrast particles may substantially alter the microstructure or mechanical properties of the material, and limit the utility of conclusions about the material behavior. This is particularly important for studying the damage response of composites, which is already sensitive to defects and microstructural variation.

Instead, the strategy employed in this dissertation is to accept the deficient speckle pattern, and characterize its limitations. It is hypothesized that the original composite microstructures can still provide reliable DVC measurement under certain conditions: it is the aim of this dissertation to validate DVC for use in such materials, and use this technique to quantitatively describe their damage mechanisms.

6. Primary research questions

Accordingly, the first research theme in this dissertation is to address the ***feasibility of DVC measurement in materials with deficient speckle patterns.*** This is particularly relevant to composites, which have carefully designed microstructures that unintentionally violate these rules. Fiber reinforcement in the CMC and PMCs creates a strongly anisotropic microstructure, which makes it challenging to accurately compute the displacement along the fiber direction. Moreover, the fibers and matrix often feature similar compositions (*e.g.*, graphite fibers in polymer matrix, or SiC fibers in SiC matrix), resulting in low X-ray contrast. Finally, the hollow glass reinforcement in syntactic foams is designed to collapse under high stresses to absorb mechanical energy, which results in a fragile microstructure that becomes severely degraded at large strains.

Fundamentally, this dissertation aims to identify the key topological characteristics that enable DVC measurement in composites. For instance, one could imagine worse DVC accuracy for composites with purely unidirectional reinforcement, than for woven/braided fiber architectures, than for random-orientation composites. Similarly, DVC accuracy should degrade with increasing damage to the syntactic foam microstructure. Thus, new error models should be developed to theoretically explain the DVC accuracy in materials with deficient speckle patterns. This is explored principally in Chapters 2, 5 and 6, which test the accuracy of DVC in elastomer-matrix syntactic foams, FSBR-processed polymer matrix composites, and braided ceramic matrix composites, respectively. DVC is experimentally validated on these materials, and in Chapter 2 these results are also reconciled with theoretical DIC/DVC error models.

The second research theme is to ***extract the role of heterogeneous microstructure on the damage micromechanisms of composites***, which is achieved by leveraging the capability of XCT/DVC to simultaneously measure *microstructure* and *local deformation* in the composite. Having shown that DVC can reliably identify the local deformation, the remaining tasks are to provide quantitative local descriptions of the microstructure and synthesize these measurements to understand the mechanics of damage in the composites. Standard image segmentation techniques, which use image contrast and topology to label different microstructural features, provide a route to extract structural measurements that can be interpreted in context of the DVC results. In Chapter 3, these techniques are developed to explore the nature of damage in syntactic foams, which is experimentally shown to be amplified within clusters of GMBs in the matrix; this finding is further supported by numerical simulation of GMB collapse in a model syntactic foam system. In Chapter 4, a DVC-enabled microstructure tracking algorithm is established to further quantify the role of GMB clustering on damage, which provides the first experimental evidence that GMB collapse occurs more rapidly in tightly-packed regions of GMBs. In Chapter 5, *in situ* mechanical testing shows that micro-buckling damage in FSBR-processed PMCs is governed by the local fiber orientation and metal impurities embedded in the stir zone. In Chapter 6, a new *in situ* expanding plug test is developed to test the failure of braided CMC tubes under hoop-stress dominated loading, which finds that failure emanates from tow crossover points and qualitatively correlates with irregular tow arrangement.

References

[1] M.R. Wisnom, Size effects in the testing of fibre-composite materials, Compos. Sci. Technol. 59 (1999) 1937–1957. doi:10.1016/S0266-3538(99)00053-6.

[2] F.W. Zok, On weakest link theory and Weibull statistics, J. Am. Ceram. Soc. 100 (2017) 1265–1268. doi:10.1111/jace.14665.

[3] A.J. Kinloch, K. Masania, A.C. Taylor, S. Sprenger, D. Egan, The fracture of glass-fibre-reinforced epoxy composites using nanoparticle-modified matrices, J. Mater. Sci. 43 (2008) 1151–1154. doi:10.1007/s10853-007-2390-3.

[4] K. Friedrich, Microstructural efficiency and fracture toughness of short fiber/thermoplastic matrix composites, Compos. Sci. Technol. 22 (1985) 43–74. doi:10.1016/0266-3538(85)90090-9.

[5] J.J. Brennan, K.M. Prewo, Silicon carbide fibre reinforced glass-ceramic matrix composites exhibiting high strength and toughness, J. Mater. Sci. 17 (1982) 2371–2383. doi:10.1007/BF00543747.

[6] G.M. Jacobsen, J.D. Stone, H.E. Khalifa, C.P. Deck, C.A. Back, Investigation of the C-ring test for measuring hoop tensile strength of nuclear grade ceramic composites, J. Nucl. Mater. 452 (2014) 125–132. doi:10.1016/j.jnucmat.2014.05.002.

[7] M.Z. Berbon, K.L. Rugg, M.S. Dadkhah, D.B. Marshall, Effect of Weave Architecture on Tensile Properties and Local Strain Heterogeneity in Thin-Sheet C-SiC Composites, J. Am. Ceram. Soc. 85 (2002) 2039–2048. doi:10.1111/j.1151-2916.2002.tb00401.x.

[8] Q.D. Yang, K.L. Rugg, B.N. Cox, D.B. Marshall, Evaluation of Macroscopic and Local Strains in a Three-Dimensional Woven C/SiC Composite, J. Am. Ceram. Soc. 88 (2005) 719–725. doi:10.1111/j.1551-2916.2005.00156.x.

[9] M.N. Rossol, V.P. Rajan, F.W. Zok, Effects of weave architecture on mechanical response of 2D ceramic composites, Compos. Part A Appl. Sci. Manuf. 74 (2015) 141–152. doi:10.1016/j.compositesa.2015.04.003.

[10] M. Chen, M. Blacklock, D. Zhang, J. Gong, Effects of stochastic tow waviness on stiffness and strength of plain-weave ceramic matrix composites, Adv. Mech. Eng. 9 (2017) 1–10. doi:10.1177/1687814017727973.

[11] E. Maire, P.J. Withers, Quantitative X-ray tomography, Int. Mater. Rev. 59 (2014) 1–43. doi:10.1179/1743280413Y.0000000023.

[12] M. Yu, P. Zhu, Y. Ma, Effects of particle clustering on the tensile properties and failure mechanisms of hollow spheres filled syntactic foams: A numerical investigation by microstructure based modeling, Mater. Des. 47 (2013) 80–89. doi:10.1016/j.matdes.2012.12.004.

[13] D. Gao, U. Ersoy, R. Stevenson, P.-C. Wang, A New One-Sided Joining Process for Aluminum Alloys: Friction Stir Blind Riveting, J. Manuf. Sci. Eng. 131 (2009) 061002. doi:10.1115/1.4000311.

[14] J. Min, Y. Li, J. Li, B.E. Carlson, J. Lin, Friction stir blind riveting of carbon fiber-reinforced polymer composite and aluminum alloy sheets, Int. J. Adv. Manuf. Technol. 76 (2015) 1403–1410. doi:10.1007/s00170-014-6364-8.

[15] K. Mosley, The stressing for test purposes of materials in tubular form using elastomeric inserts—experimental and theoretical development, Arch. Proc. Inst. Mech. Eng. 1847-1982 (Vols 1-196). 196 (1982) 123–139. doi:10.1243/PIME_PROC_1982_196_014_02.

[16] Y. Wang, Y. Chai, C. Soutis, P.J. Withers, Evolution of kink bands in a notched unidirectional carbon fibre-epoxy composite under four-point bending, Compos. Sci. Technol. 172 (2019) 143–152. doi:10.1016/J.COMPSCITECH.2019.01.014.

[17] B.M. Patterson, N.L. Cordes, K. Henderson, J.J. Williams, T. Stannard, S.S. Singh, A.R. Ovejero, X. Xiao, M. Robinson, N. Chawla, In situ X-ray synchrotron tomographic imaging during the compression of hyper-elastic polymeric materials, J. Mater. Sci. 51 (2016) 171–187. doi:10.1007/s10853-015-9355-8.

[18] E. Maire, C. Le Bourlot, J. Adrien, A. Mortensen, R. Mokso, 20 Hz X-ray tomography during an in situ tensile test, Int. J. Fract. (2016) 1–10. doi:10.1007/s10704-016-0077-y.

[19] S.C. Garcea, Y. Wang, P.J. Withers, X-ray computed tomography of polymer composites, Compos. Sci. Technol. 156 (2018) 305–319. doi:10.1016/j.compscitech.2017.10.023.

[20] M.J. Emerson, Y. Wang, P.J. Withers, K. Conradsen, A.B. Dahl, V.A. Dahl, Quantifying fibre reorientation during axial compression of a composite through time-lapse X-ray imaging and individual fibre tracking, Compos. Sci. Technol. 168 (2018) 47–54. doi:10.1016/J.COMPSCITECH.2018.08.028.

[21] S.C. Garcea, I. Sinclair, S.M. Spearing, P.J. Withers, Mapping fibre failure in situ in carbon fibre reinforced polymers by fast synchrotron X-ray computed tomography, Compos. Sci. Technol. 149 (2017) 81–89. doi:10.1016/J.COMPSCITECH.2017.06.006.

[22] A.E. Scott, M. Mavrogordato, P. Wright, I. Sinclair, S.M. Spearing, In situ fibre fracture measurement in carbon–epoxy laminates using high resolution computed tomography, Compos. Sci. Technol. 71 (2011) 1471–1477. doi:10.1016/J.COMPSCITECH.2011.06.004.

[23] N.M. Larson, F.W. Zok, In-situ 3D visualization of composite microstructure during polymer-to-ceramic conversion, Acta Mater. 144 (2018) 579–589. doi:10.1016/J.ACTAMAT.2017.10.054.

[24] J. Hemmer, C. Burtin, S. Comas-Cardona, C. Binetruy, T. Savart, A. Babeau, Unloading during the infusion process: Direct measurement of the dual-scale fibrous microstructure

evolution with X-ray computed tomography, Compos. Part A Appl. Sci. Manuf. 115 (2018) 147–156. doi:10.1016/J.COMPOSITESA.2018.09.013.

[25] T. Centea, P. Hubert, Measuring the impregnation of an out-of-autoclave prepreg by micro-CT, Compos. Sci. Technol. 71 (2011) 593–599. doi:10.1016/J.COMPSCITECH.2010.12.009.

[26] J. Vilà, F. Sket, F. Wilde, G. Requena, C. González, J. LLorca, An in situ investigation of microscopic infusion and void transport during vacuum-assisted infiltration by means of X-ray computed tomography, Compos. Sci. Technol. 119 (2015) 12–19. doi:10.1016/J.COMPSCITECH.2015.09.016.

[27] J. Lachambre, E. Maire, J. Adrien, D. Choqueuse, In situ observation of syntactic foams under hydrostatic pressure using X-ray tomography, Acta Mater. 61 (2013) 4035–4043. doi:10.1016/j.actamat.2013.03.017.

[28] C.T. Chantler, K. Olsen, R.A. Dragoset, J. Chang, A.R. Kishore, S.A. Kotochigova, D.S. Zucker, Detailed Tabulation of Atomic Form Factors, Photoelectric Absorption and Scattering Cross Section, and Mass Attenuation Coefficients for Z = 1-92 from E = 1-10 eV to E = 0.4-1.0 MeV, 2005. doi:10.18434/T4HS32.

[29] M.W. Czabaj, M.L. Riccio, W.W. Whitacre, Numerical reconstruction of graphite/epoxy composite microstructure based on sub-micron resolution X-ray computed tomography, Compos. Sci. Technol. 105 (2014) 174–182. doi:10.1016/j.compscitech.2014.10.017.

[30] J.Y. Buffiere, E. Maire, J. Adrien, J.P. Masse, E. Boller, In Situ Experiments with X ray Tomography: an Attractive Tool for Experimental Mechanics, Exp. Mech. 50 (2010) 289–305. doi:10.1007/s11340-010-9333-7.

[31] J.-Y. Buffière, E. Maire, P. Cloetens, G. Lormand, R. Fougères, Characterization of internal damage in a MMCp using X-ray synchrotron phase contrast microtomography, Acta Mater. 47 (1999) 1613–1625. doi:10.1016/S1359-6454(99)00024-5.

[32] J.C.E. Mertens, K. Henderson, N.L. Cordes, R. Pacheco, X. Xiao, J.J. Williams, N. Chawla, B.M. Patterson, Analysis of thermal history effects on mechanical anisotropy of 3D-printed polymer matrix composites via in situ X-ray tomography, J. Mater. Sci. 52 (2017) 12185–12206. doi:10.1007/s10853-017-1339-4.

[33] P. Ruusuvuori, T. Äijö, S. Chowdhury, C. Garmendia-Torres, J. Selinummi, M. Birbaumer, A.M. Dudley, L. Pelkmans, O. Yli-Harja, Evaluation of methods for detection of fluorescence labeled subcellular objects in microscope images, BMC Bioinformatics. 11 (2010) 248. doi:10.1186/1471-2105-11-248.

[34] T.G. Mason, K. Ganesan, J.H. van Zanten, D. Wirtz, S.C. Kuo, Particle Tracking Microrheology of Complex Fluids, Phys. Rev. Lett. 79 (1997) 3282–3285. doi:10.1103/PhysRevLett.79.3282.

[35] N. Chenouard, I. Smal, F. de Chaumont, M. Maška, I.F. Sbalzarini, Y. Gong, J.

Cardinale, C. Carthel, S. Coraluppi, M. Winter, A.R. Cohen, W.J. Godinez, K. Rohr, Y. Kalaidzidis, L. Liang, J. Duncan, H. Shen, Y. Xu, K.E.G. Magnusson, J. Jaldén, H.M. Blau, P. Paul-Gilloteaux, P. Roudot, C. Kervrann, F. Waharte, J.-Y. Tinevez, S.L. Shorte, J. Willemse, K. Celler, G.P. van Wezel, H.-W. Dan, Y.-S. Tsai, C.O. de Solórzano, J.-C. Olivo-Marin, E. Meijering, Objective comparison of particle tracking methods, Nat. Methods. 11 (2014) 281–289. doi:10.1038/nmeth.2808.

[36] X. Feng, M.S. Hall, M. Wu, C.-Y. Hui, An adaptive algorithm for tracking 3D bead displacements: application in biological experiments, Meas. Sci. Technol. 25 (2014) 055701. doi:10.1088/0957-0233/25/5/055701.

[37] S.F. Nielsen, F. Beckmann, H.F. Poulsen, J.A. Wert, Measurement of the components of plastic displacement gradients in three dimensions, Mater. Sci. Eng. A. 387–389 (2004) 336–338.

[38] H. Toda, H. Sinclair, J.-Y. Buffière, E. Maire, K.H. Khor, P. Gregson, T. Kobayashi, A 3D measurement procedure for internal local crack driving forces via synchrotron X-ray microtomography, Acta Mater. 52 (2004) 1305–1317. doi:10.1016/j.actamat.2003.11.014.

[39] M. Kobayashi, H. Toda, Y. Kawai, T. Ohgaki, K. Uesugi, D.S. Wilkinson, T. Kobayashi, Y. Aoki, M. Nakazawa, High-density three-dimensional mapping of internal strain by tracking microstructural features, Acta Mater. 56 (2008) 2167–2181. doi:10.1016/j.actamat.2007.12.058.

[40] H. Toda, E. Maire, Y. Aoki, M. Kobayashi, Three-dimensional strain mapping using in situ X-ray synchrotron microtomography, J. Strain Anal. Eng. Des. 46 (2011) 549–561. doi:10.1177/0309324711408975.

[41] N. Li, M.A. Sutton, H.W. Schreier, J.L. Turner, N. Mani, Strain Measurements Through Optimized Particle Tracking in Volumetric Images: Methodology and Error Assessment, Exp. Mech. 56 (2016) 1281–1291. doi:10.1007/s11340-016-0146-1.

[42] A. Buljac, C. Jailin, A. Mendoza, J. Neggers, T. Taillandier-Thomas, A. Bouterf, B. Smaniotto, F. Hild, S. Roux, Digital Volume Correlation: Review of Progress and Challenges, Exp. Mech. 58 (2018) 661–708. doi:10.1007/s11340-018-0390-7.

[43] B.K. Bay, Methods and applications of digital volume correlation, J. Strain Anal. Eng. Des. 43 (2008) 745–760. doi:10.1243/03093247JSA436.

[44] F. Hild, A. Bouterf, S. Roux, Damage measurements via DIC, Int. J. Fract. 191 (2015) 77–105. doi:10.1007/s10704-015-0004-7.

[45] B.K. Bay, T.S. Smith, D.P. Fyhrie, M. Saad, Digital volume correlation: Three-dimensional strain mapping using X-ray tomography, Exp. Mech. 39 (1999) 217–226. doi:10.1007/BF02323555.

[46] M.A. Sutton, W. Wolters, W.H. Peters, W. Ranson, S.R. McNeill, Determination of

displacements using an improved digital correlation method, Image Vis. Comput. 1 (1983) 133–139. doi:10.1016/0262-8856(83)90064-1.

[47] H.A. Bruck, S.R. McNeill, M.A. Sutton, W.H. Peters, Digital image correlation using Newton-Raphson method of partial differential correction, Exp. Mech. 29 (1989) 261–267. doi:10.1007/BF02321405.

[48] N. Limodin, J. Réthoré, J. Adrien, J.-Y. Buffière, F. Hild, S. Roux, Analysis and Artifact Correction for Volume Correlation Measurements Using Tomographic Images from a Laboratory X-ray Source, Exp. Mech. 51 (2011) 959–970. doi:10.1007/s11340-010-9397-4.

[49] B. Wang, B. Pan, G. Lubineau, In-Situ Systematic Error Correction for Digital Volume Correlation Using a Reference Sample, Exp. Mech. C (2017) 1–10. doi:10.1007/s11340-017-0356-1.

[50] B. Wang, B. Pan, R. Tao, G. Lubineau, Systematic errors in digital volume correlation due to the self-heating effect of a laboratory x-ray CT scanner, Meas. Sci. Technol. 28 (2017) 055402. doi:10.1088/1361-6501/aa60ad.

[51] M.A. Sutton, J.-J. Orteu, H.W. Schreier, Image Correlation for Shape, Motion and Deformation Measurements, Springer US, Boston, MA, 2009. doi:10.1007/978-0-387-78747-3.

[52] R.B. Lehoucq, P.L. Reu, D.Z. Turner, The Effect of the Ill-posed Problem on Quantitative Error Assessment in Digital Image Correlation, Exp. Mech. (2017) 1–13. doi:10.1007/s11340-017-0360-5.

[53] P. Mazzoleni, F. Matta, E. Zappa, M.A. Sutton, A. Cigada, Gaussian pre-filtering for uncertainty minimization in digital image correlation using numerically-designed speckle patterns, Opt. Lasers Eng. 66 (2015) 19–33. doi:10.1016/j.optlaseng.2014.08.004.

[54] D. Lecompte, H. Sol, J. Vantomme, A. Habraken, Analysis of speckle patterns for deformation measurements by digital image correlation, in: P. Slangen, C. Cerruti (Eds.), Proc. SPIE 6341, International Society for Optics and Photonics, 2006: p. 63410E. doi:10.1117/12.695276.

[55] G. Lionello, L. Cristofolini, A practical approach to optimizing the preparation of speckle patterns for digital-image correlation, Meas. Sci. Technol. 25 (2014) 107001. doi:10.1088/0957-0233/25/10/107001.

[56] P. Reu, All about speckles: Speckle Size Measurement, Exp. Tech. 38 (2014) 1–2. doi:10.1111/ext.12110.

[57] Y.L. Dong, B. Pan, A Review of Speckle Pattern Fabrication and Assessment for Digital Image Correlation, Exp. Mech. 57 (2017) 1161–1181. doi:10.1007/s11340-017-0283-1.

[58] B. Pan, H. Xie, Z. Wang, K. Qian, Z. Wang, Study on subset size selection in digital

image correlation for speckle patterns, Opt. Express. 16 (2008) 7037. doi:10.1364/OE.16.007037.

[59] R. Brault, A. Germaneau, J.C. Dupré, P. Doumalin, S. Mistou, M. Fazzini, In-situ Analysis of Laminated Composite Materials by X-ray Micro-Computed Tomography and Digital Volume Correlation, Exp. Mech. 53 (2013) 1143–1151. doi:10.1007/s11340-013-9730-9.

Chapter 2:
Effect of fragile speckle patterns on accuracy of digital volume correlation

1. Introduction

Both digital image correlation (DIC) [1] and its three-dimensional analogue digital volume correlation (DVC) [2] compute the deformation field by tracking the aggregate motion of neighborhoods of features through a sequence of *in situ* experimental images (or 3D tomograms acquired by volumetric imaging techniques). This is achieved by correlating the deformed image with the original undeformed image, and computing the translation, rotation and deformation of the image from the reference state into the deformed state. Generally speaking, the sample should exhibit a high-quality, high-contrast, random "speckle pattern" to ensure the uniqueness and accuracy of the deformation measurement [3,4]. One of the fundamental assumptions of DIC and DVC algorithms is that the individual speckles in the pattern be ***durable*** to allow them to be tracked in each image, so they should not substantially change appearance or disappear throughout the experiment. While such a speckle pattern can readily be applied to the surface of a specimen using spray paint, toner, or one of many other techniques for two-dimensional or stereo DIC, it is intrinsically challenging (and often undesirable) to modify the internal microstructure of three-dimensional specimens to meet these criteria for DVC measurement [5]. Instead, the intrinsic contrast and texture of the microstructure can substitute for a high-quality artificial pattern.

As a result, a common deficiency of volumetric speckle patterns is the degradation of the microstructure under load, which can lead to decorrelation and inaccurate measurements. One common example is due to the development of damage in the material, which introduces new contrasting features to the material that were not present in the reference state. This is frequently encountered in brittle materials that undergo microcracking, such as ceramic matrix composites

[6–9], plasterboard [10], and graphite [11]. Alternatively, this can be observed in the rupture of ductile metals, which is commonly preceded by void initiation, coalescence and growth into a crack [12]. Unless the damage mechanisms are explicitly incorporated into the warping functions for the DVC algorithms (such as Heaviside DVC [13] or extended-DVC analogous to X-FEM techniques [14]), these features cause the image to violate the principle of "gray-level conservation" and therefore reduce the quality of the DVC measurement. However, it is generally acknowledged that DVC measurements will remain reasonably accurate provided the volume of damaged material remains small compared to the quantity of markers in the speckle pattern, as is the case in these examples.

Another scenario is the disappearance of individual speckles between the reference and deformed states, which also deleteriously affects DVC accuracy. This is particularly relevant for DVC experiments that tend to rely on the intrinsic texture of the material of interest, which may not be stable at large deformation as in the cases of foams [15–17], bone [2,18] and granular materials [19,20]. Even in surface-based DIC applications where artificial patterns are easily applied, the pattern may degrade when painted markers flake off the area of interest or fade with large deformation. It is currently unclear how this degradation affects DVC accuracy.

Recent *in situ* X-ray Computed Tomography (XCT) experimental measurements by the authors have shown that DVC remains viable even in cases of severe damage to the speckle pattern with only minor losses in accuracy. As reported in Ref. [21], tomograms of syntactic foams were acquired at increasing levels of uniaxial compression. The syntactic foam consisted of an elastomer matrix filled with hollow glass microballoons (GMBs), which produced an archetypal 3D speckle pattern in the undamaged state (Fig. 2.1a). At increasing deformation, many of these GMBs crushed under mechanical load and eventually disappeared from the tomogram (Fig. 2.1b), so a significant fraction of the markers that constituted the speckle pattern eventually disappeared from the images. Remarkably, accurate DVC measurements were obtained until 40% of the GMBs had collapsed.

The ability to accurately correlate heavily damaged tomograms challenges our current assumptions about requirements for speckle patterns. In particular, these findings indicate that rules about gray level conservation can be relaxed in certain cases to permit measurement of specimens with fragile speckle patterns. The objective of this paper is to explore the limits of DVC for materials with fragile microstructures and speckle patterns, and to quantify the effects of microstructure degradation as well as DVC analysis parameters on measurement accuracy. Certainly, use of DVC to study fragile microstructure comes at a cost of decreased accuracy, but how much damage is tolerable? The feasibility of DVC in these scenarios is first explored through experimental measurements using rigid body motion experiments to capture the effect on error under real imaging conditions. Later, analysis of synthetic images with controlled levels of speckle pattern degradation is used to more accurately quantify the effects on DVC accuracy without influence of additional experimental error sources. Finally, these effects are addressed from a theoretical perspective to reconcile these trends with existing models of DVC error.

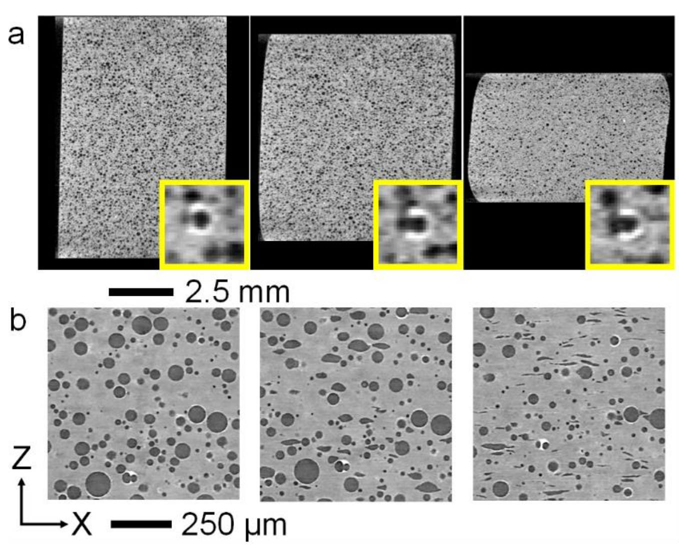

Fig. 2.1. Virtual cross-sections of compressed syntactic foam during *in situ* experiment. (a) Slices from low-resolution for DVC analysis at increasing strain, with insets showing subvolume size. (b) Slices from the corresponding high-resolution XCT images, showing collapse of GMBs. Images adapted from experiment in Ref. [21].

2. DVC preliminaries

The basis for all DVC algorithms is the cross-correlation between the reference and deformed subvolumes. Since cross-correlation measures the similarity between two volumes, the optimal solution is obtained when each pixel in the deformed volume is mapped to the corresponding pixel in the reference coordinate, *i.e.* the displacement field is solved. One way of achieving this is by using optimization schemes to maximize the zero-mean, normalized cross-correlation (ZNCC), which is notably insensitive to systematic changes in contrast and illumination [3]. The ZNCC is computed as,

$$C_{ZNCC}(\boldsymbol{x}) = \frac{1}{N} \sum_{\boldsymbol{x} \in S} \left(\frac{F(\boldsymbol{x}) - \bar{F}}{\sigma_F} \frac{G\big(\boldsymbol{x} + \boldsymbol{u}(\boldsymbol{x})\big) - \bar{G}}{\sigma_G} \right) \tag{2.1}$$

where F and G correspond to the reference and deformed images, $\boldsymbol{x}$ represents the coordinates within the reference subset S, $\boldsymbol{u}(\boldsymbol{x})$ is the displacement field that maps undeformed coordinates into their deformed state, $\bar{F}$ and $\bar{G}$ indicate the average intensities of each subset, and σ_F and σ_G are the standard deviations of intensities within each subset. In contrast to the other chapters, C_{ZNCC} is selected for convenience in expressing the correlation strength: a "perfect" correlation score has the value of $C_{ZNCC} = 1$, whereas fully-decorrelated images have $C_{ZNCC} = -1$. As summarized in Ref. [22], Eq. 2.1 can be mathematically related to the C_{LS} used in other chapters.

2.1. Notation to describe specimen degradation

The primary concern about correlating images of fragile speckle patterns is that C_{ZNCC}

will decrease as the specimen degrades, increasing the possibility that the optimization algorithm will identify inaccurate displacement and strain fields due to decorrelation effects. For purposes of this chapter, unique notation is developed to concisely describe the damaged character of speckle patterns:

- ϕ – Volume fraction of markers in undamaged state (from 0 to 1)
- α – Fraction of markers that are damaged (from 0 to 1)
- C – Residual contrast of all damaged markers (from 0 to 1)

3. Experimental methods

3.1. Materials

Sylgard GMB specimens were prepared by mixing A16 glass microballoons (3M) into two-part Sylgard 184 silicone elastomer (Dow Corning) and curing agent. The mixture was drawn into a cylindrical syringe and cured at room temperature with an accelerator. After curing, the molded foam was carefully cut into cylindrical specimens with 7 mm height and diameters of 4.8 mm. The diameter of A16 GMBs ranges from 30 to 95 µm within 10-90% distribution, with a mean diameter of 60 µm. Three specimens were manufactured with nominal GMB volume fractions of 0.20, 0.30 and 0.46. Since the low-resolution tomograms could not discern GMB walls from the matrix, the actual void volume fractions were 0.147, 0.225 and 0.422; to allow generalization to other types of speckle patterns, all results are reported in terms of the void volume fraction.

3.2. Rigid body motion experiments

Experimental assessment of the error due to fragile specimens was performed using rigid body motion experiments during *in situ* compression of the syntactic foams. Syntactic foam specimens were compressed uniaxially using a custom, screw-driven loading stage as reported in [6,23]. The specimen was deformed between two acrylic platens to minimize reconstruction artifacts near the specimen edges. Each specimen was compressed in roughly 500 μm increments until DVC failed to achieve correlation, resulting in 5 or 6 *in situ* load steps per specimen.

Three tomograms were acquired at each load step. First, one high-resolution tomogram with voxel resolution of $[1.7\ \mu m]^3$ was used to quantify the volume fraction of GMBs in the undamaged state, and the fraction of damaged GMBs in subsequent steps. Second, a low-resolution tomogram was acquired with voxel resolution of $[8.5\ \mu m]^3$, resulting in a typical speckle diameter of 6-8 voxels that was ideal for DVC analysis. Finally, an additional low-resolution tomogram was acquired after axially displacing the sample 250 μm. The higher resolution tomogram was necessary to accurately measure the size and Feret shape (3D aspect ratio) of the GMBs [24], while the difference in measured displacements and strains between the pair of low-resolution tomograms enabled an assessment of DVC error. All tomographic imaging was performed using X-radia MicroXCT 200 with X-ray source parameters 80 keV and 8 W. High-resolution tomograms were reconstructed from a set of 2401 radiographs between -103° and 103° rotation with 6.5 second exposure, and the low-resolution tomograms were reconstructed from a set of 1401 radiographs between -103° and 103° rotation with 7 second exposure.

Dimensional quantification of the GMBs was performed using Python image processing scripts and Avizo Fire 9.0. The raw 16-bit high-resolution tomograms were sequentially smoothed using nonlocal means filters, downsampled to 8-bit images, thresholded and segmented with standard image processing techniques. The 3D Feret shape (FS, equivalent to the particle's aspect ratio) was used to identify the collapse of each segmented GMB, where $FS > 1.3$

indicated an ellipsoidal geometry consistent with GMB collapse. In contrast, low FS indicated spherical geometry of an intact GMB.

Both the mechanical response and the damage behavior are reported in Fig. 2.2 for the three different volume fractions. The stress-strain curves were typical for elastomeric syntactic foams [25], which generally exhibit an initially stiff elastic response, a plateau region associated with GMB collapse at relatively constant stress, and densification of the foam [26]. Both the elastic stiffness and prominence of the plateau region increased with higher GMB reinforcement, whereas the syntactic foams with lower GMB volume fraction behaved more like the elastomer matrix. In the three specimens, appreciable GMB collapse occurred only after reaching the plateau region, and damage increased approximately linearly thereafter. GMB collapse occurred more rapidly at higher volume fractions, as particle clustering is known to amplify the GMB stresses [21,27,28].

The low-resolution tomograms were independently correlated against a single reference tomogram using commercial DVC code (Vic-Volume, Correlated Solutions) with a subset size of 29 voxels, and step size of 10 voxels. This subset size was selected to include roughly $3^3 = 27$ speckles per subset for the $\phi = 0.147$ specimen, which is a general guideline for DIC/DVC analysis. A sensitivity study found that step size had no effect on the displacement errors. Additionally, the step size did not affect the nonlinear dependence between strain error and damage, but simply scaled the error by a factor of $1/step^2$; the latter relationship matches the sensitivity of a central-differences numerical differentiation scheme to noise.

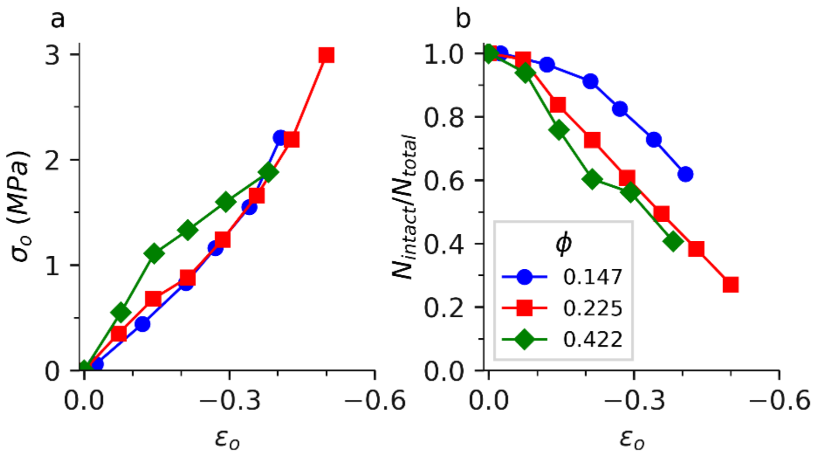

Fig. 2.2. Mechanical behavior of syntactic foam specimens. (a) Engineering stress vs. engineering strain curves. (b) Fraction of intact specimens vs. engineering strain.

Strain was computed with a strain filter size of 5 subsets, which was the minimum filter size available in the software. The strain filter averaged the displacement gradient uniformly across neighboring subsets, with the aim of decreasing measurement noise compared to calculation of strain from a single subset. As the objective of this analysis was to identify the "worst case" DVC strain error due to speckle pattern degradation, the total strain filtering was adjusted to the minimum possible value in the software; future users could increase strain filtering to further reduce the effects of speckle pattern degradation at the cost of spatial resolution. This combination of analysis parameters resulted in a virtual strain gage size of [79 voxels]^3 = [672 μm]^3. All analysis was performed with a 4-tap spline-based interpolation scheme [3]. To measure the error in the DVC-computed strain, the difference in measured strain was recorded at each subset for the corresponding deformed and deformed rigid body motion tomograms.

4. Experimental results

To experimentally evaluate the displacement and strain errors, the DVC measurements were compared before and after rigid body motion. Since both tomograms were acquired at the same state of compression and were correlated independently against the same reference tomogram, they should theoretically exhibit the same strain field. Any differences are attributed to the various sources of measurement error. In particular, error in the undeformed state ($\varepsilon = 0$) reflects the noise floor of the measurement system, while subsequent increases in error as the syntactic foam is compressed can be attributed to the effects of speckle pattern degradation.

4.1. Displacement error

The axial displacement field for a syntactic foam specimen with void volume fraction $\phi = 0.225$ is presented in Fig. 2.3 at three increasing deformations. While the specimen exhibited some buckling at the highest loads, the displacement field was predominantly uniaxial in nature (Fig. 2.3a). After removing rigid body motion from the measurements, it was clear that the DVC measurements exhibited strong repeatability (Fig. 2.3b). Any differences in the experimental displacement fields were imperceptible at this level of contrast, even at the largest deformations.

To highlight any DVC error between the two analyses, Fig. 2.3c shows the difference in measured axial displacement $\Delta w = w - w^{RBM}$ at the same three deformations. For nominal strains of strain $\varepsilon_0 = -0.12$ and $\varepsilon_o = -0.24$, the resulting DVC error was small in magnitude. For all subsets the error remained below 0.2 voxels, and in most cases was below .05 voxels. As confirmed in Fig. 2.3d, the displacement error was only marginally higher at $\varepsilon_o = -0.24$ compared to $\varepsilon_o = -0.12$. Additionally, variation in Δw was uniform and random throughout the specimen, indicating that the error calculation was not affected by distortion artifacts or damage localization.

However, at the final strain increment of $\varepsilon_0 = -0.30$, the error noticeably increased throughout the specimen. Inspection of Fig. 2.3c for this deformation identified several anomalous "hot spots" in the displacement calculation, indicating large discrepancy of $\Delta w >$ 0.2 voxels between the w and w^{RBM} calculations at these points. Despite this, the majority of the displacement measurements remained accurate to within $\Delta w < 0.1$ voxels, indicating that the DVC analysis was generally trustworthy despite severe degradation to the speckle pattern. Thus, DVC may cautiously be used in specimens despite widespread microstructural damage.

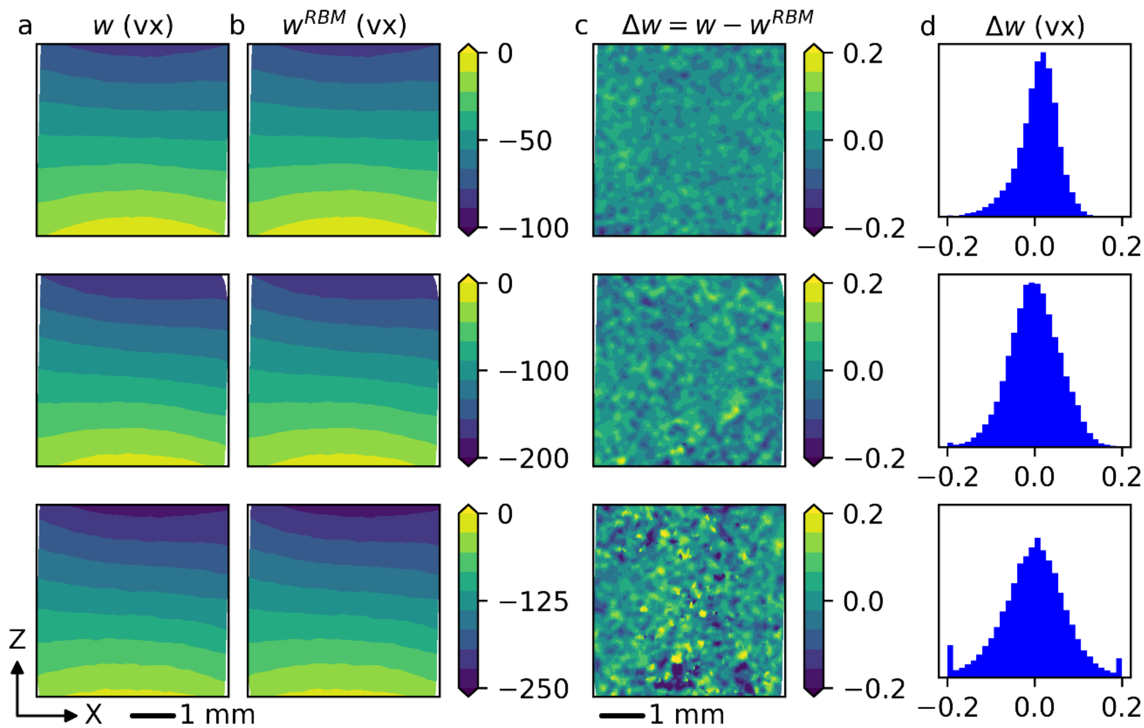

Fig. 2.3. Experimental assessment of axial displacement error for syntactic foam specimen with $\phi = 0.223$. (a-b) Measured axial displacement in voxels (a) before (w) and (b) after rigid body motion (w^{RBM}); (c) difference between measured displacements Δw; and (d) histogram of Δw. Results are shown at (top) nominal strain $\varepsilon_0 = -0.12$, (middle) $\varepsilon_o = -0.24$, and (bottom) $\varepsilon_0 = -0.30$. Note that the rigid body motion is removed when plotting w^{RBM}.

This analysis was repeated on the additional two specimens to compare the error trends as a function of the syntactic foam microstructure and damage characteristics (Fig. 2.4). These results loosely identify two key analysis regimes. First, DVC error remained near the noise floor below a critical level of speckle pattern degradation. These errors were approximately $\Delta w =$

0.03 voxels for $\phi = 0.225$ and 0.422, and $\Delta w = 0.05$ for $\phi = 0.147$. In this regime, DVC measurements could be considered "stable," and good accuracy can be guaranteed.

Second, after exceeding a critical level of speckle pattern degradation at $\alpha \approx 0.3$, the displacement error rapidly increased. In other words, the effects of minor speckle pattern degradation on DVC accuracy were less significant than other experimental factors, including the initial speckle pattern quality or imaging noise. Only at severe degradation did this error source become significant. Thus, these measurements became "unstable," where accuracy depended on the local damage state and cannot be generally guaranteed.

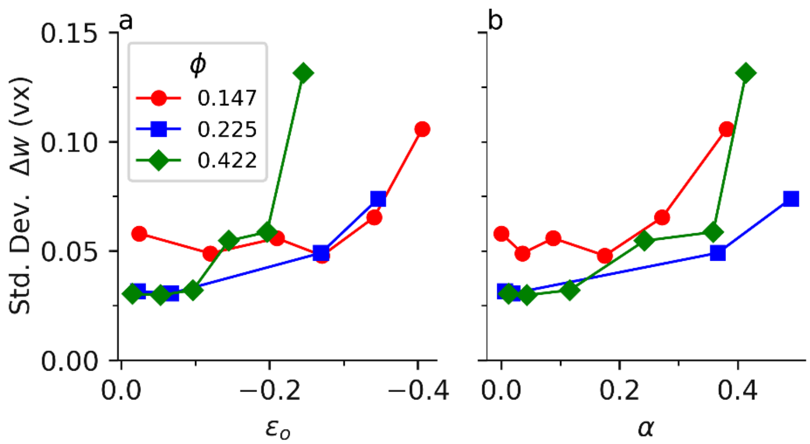

Fig. 2.4. Displacement error as function of (a) engineering strain ε_o and (b) fraction of damaged GMBs α in the different syntactic foams.

4.2. Strain error

Equivalent analyses were performed to interpret the effects of speckle pattern degradation on strain measurement accuracy. First, the axial strain fields are presented in Fig. 2.5a. Under uniform axial compression, the specimen exhibited strong variation in axial strain due to heterogeneous collapse of GMBs. As was previously discussed in [21] and also observed in some other syntactic foams [29], this behavior was mechanistically related to the redistribution of stress around collapsed GMBs and the propagation of damage through the syntactic foam. For the specimen with void volume fraction $\phi = 0.225$, the intensity of the strain field variation increased from $\varepsilon_{zz} \approx 0.01$ at a nominal strain of $\varepsilon_0 = -0.12$, to $\varepsilon_{zz} \approx 0.05$ at a nominal strain of $\varepsilon_0 = -0.30$. Analysis of the strains after rigid body motion (Fig. 2.5b) showed very little difference compared to the original analysis, confirming the measurement accuracy.

To more precisely evaluate the error, the difference between measured strain fields, $\Delta\varepsilon_{zz} = \varepsilon_{zz} - \varepsilon_{zz}^{RBM}$, was computed at each subvolume (Fig. 2.5c). Here, while the $\Delta\varepsilon_{zz}$ field exhibited a similar banded appearance, the magnitude of variation in $\Delta\varepsilon_{zz}$was roughly 5 times smaller than the variation in ε_{zz}. This trend was especially true when the specimen was imaged at low strain with little degradation to the speckle pattern ($\varepsilon_o = -0.12$). In the low-strain images, variation approached the noise floor associated with this particular combination of XCT imaging and DVC analysis parameters. At higher strains ($\varepsilon_o = -0.30$) with more damage, the error increased marginally, although many subvolumes produced obviously spurious strain values with $|\Delta\varepsilon_{zz}| > 0.01$; these points appeared as yellow or purple spots in Fig. 2.5c. This trend was validated by comparing the histograms of $\Delta\varepsilon_{zz}$ in Fig. 2.5d, which showed both an increase in both standard deviation and number of outliers in each measured strain field. Interestingly, the increase in strain error occurred rapidly, as error at an intermediate strain of $\varepsilon_o = -0.24$ remained small.

Similar analyses were repeated for all three specimens, and the standard deviation of $\Delta\varepsilon_{zz}$ as a function of the speckle pattern degradation is reported for each load increment in Fig. 2.6. These trends resembled those for displacement in Fig. 2.4, and also showed that the accuracy of the DVC strain measurements remained near the measurement noise floor until a critical level of speckle pattern degradation was achieved. Typical error in this regime of minor speckle pattern degradation ranged from $\sigma_{\Delta\varepsilon_{zz}} = 98\ \mu\varepsilon$ for $\phi = 0.147$ and $54\ \mu\varepsilon$ for $\phi = 0.422$, with the different speckle pattern densities accounting for the discrepancies between specimens.

In contrast, error in the strain measurement rapidly grew to unacceptable levels once the speckle pattern degradation reached a critical value. This effect was much more prominent for strain than for displacement, which can be attributed to the sensitivity of numerical differentiation schemes (to compute strain) to noise in the displacement signal. Due to volume-fraction dependent damage mechanisms for the syntactic foams, this transition varied somewhat between specimens. This transition occurred most rapidly at $\varepsilon_o = -0.2$ in the high volume fraction specimen, and later at $\varepsilon_o = -0.35$ in the low volume fraction specimen.

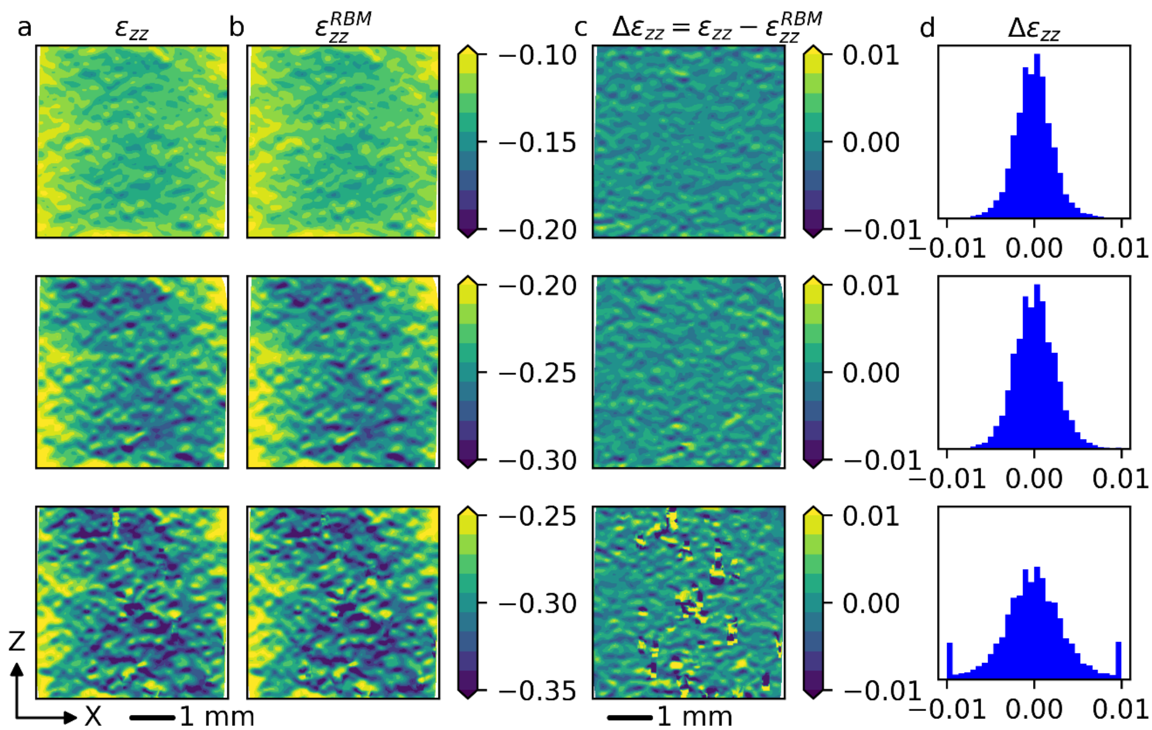

Fig. 2.5. Experimental assessment of strain error for syntactic foam specimen with $\phi = 0.223$. (a-b) Measured axial strain (a) before and (b) after rigid body motion; (c) difference between measured strain $\Delta\varepsilon_{zz}$; and (d) histogram of $\Delta\varepsilon_{zz}$. Results are shown at (top) nominal strain $\varepsilon_0 = -0.12$, (middle) $\varepsilon_o = -0.24$, and (bottom) $\varepsilon_0 = -0.30$.

When measured in terms of damage to the speckle pattern, the results suggested that the critical level of degradation varied with both the GMB content and the damage mechanisms in the syntactic foam. For instance, the low volume fraction specimen exhibited the least resilience to speckle pattern damage with critical $\alpha \approx 0.27$ before error rapidly increased, which could be attributed to the sparse speckle pattern. On the other hand, the two specimens with higher volume fractions exhibited a critical $\alpha \approx 0.36$, indicating the benefit of a denser speckle pattern. Despite this, error increased faster in the $\phi = 0.422$ specimen after the critical transition, possibly due to enhanced strain localization.

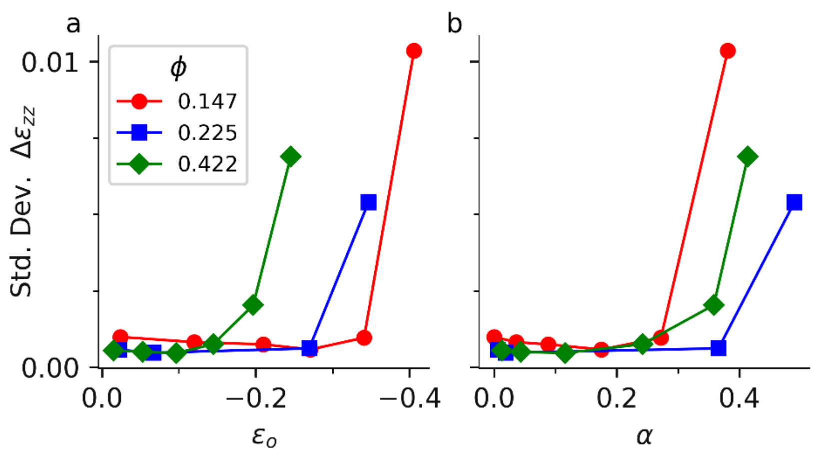

Fig. 2.6. Strain error as function of (a) engineering strain ε_o and (b) fraction of damaged GMBs α in the different syntactic foams.

5. *Numerical Methods*

While the experimental results clearly showed that accurate DVC measurements could be obtained despite widespread damage to the speckle pattern, these trends were convoluted by imaging artifacts such as distortion and other XCT error sources [30]. Additionally, heterogeneous deformation such as crush-band effects or strain localization [29] could further bias these measurements.

To address these challenges, synthetic images were generated and then analyzed by DVC to assess the separate roles of *fraction of damaged markers* and *degraded marker contrast* on the accuracy of DVC strain computations. These two parameters can approximate the degradation of many other materials in addition to syntactic foams. For example, while GMBs tend to quickly collapse and disappear from tomograms, other materials may exhibit a more gradual failure process in which markers slowly lose contrast. Simulations were performed for many volume fractions of markers. In this way, the simulation results can be readily adapted to other material systems.

5.1. Generation of synthetic images

To establish the effects of pattern degradation on DVC error, artificial images with increasing levels of degradation and no strain were generated. Synthetic images with prescribed damage levels were developed through a three-step process of generating an undamaged reference pattern, degrading selected markers in the pattern, and then adding Gaussian noise to simulate experimental image conditions. Correlation of the synthetic volumes to the undamaged reference state using commercial DVC software provided an assessment of errors due to microstructure degradation.

First, a reference volume of size $1024 \times 256 \times 256$ voxels was generated with bright markers on a dark background by perturbing the position of markers on a 3D regular grid, similar to the technique used in [31]. The grid pitch was modified to change the volume fraction ϕ between 0.136 and 0.407 which encompassed representative porosities found in many syntactic foams and other DVC specimens [25,29,32,33]. Speckles were modeled as modified 3D Gaussian signals with standard deviations σ randomly selected between 1 and 3 voxels,

$$I_{speckle}(\boldsymbol{x}) = \min\left(200, 400\, exp\left(\sum_{i=1}^{3} \frac{-(x_i - x_i^c)^2}{\sigma^2}\right)\right) \tag{2.2}$$

where x_i represents the image coordinate, and x_i^c represents the subpixel center of the marker.

The intensity of the central region in each speckle was truncated to imitate the uniform intensity of the hollow GMBs. In contrast to explicitly modeling the spherical particles, the modified Gaussian profile allowed facile imposition of subpixel displacements and deformations without relying on downsampling or interpolation filters. The speckles in the deformed images were analytically translated by 0.5 voxels from their reference position; this subpixel displacement has been shown to maximize the DVC-measured displacement variance due to image interpolation [3,31], and provided a more challenging measurement problem than a set of images with no applied motion.

To efficiently survey the different combinations of α and C that represent various degrees of pattern degradation, damage was introduced to each pattern by randomly flagging markers for degradation as a linear function of the x coordinate. In this way, the probability of damage increased from $\alpha = 0.0$ at $x = 0$ to $\alpha = 1.0$ at $x = 1024$ (Fig. 2.7). The residual contrast of each flagged particle was incrementally decreased from $C = 1.0$ to 0.0, resulting in several images with many faint particles and one image with fully deleted particles. Since damage only varied in the x direction, there existed many data points on each $y - z$ plane to statistically analyze the effects of marker degradation. The intensities of the 3D volumes were scaled for 8-bit images, with the dark background assigned an intensity of 25, and the undamaged particles an intensity of 225; this intensity range allowed noise to be added to the image.

Finally, Gaussian noise was independently added to each image to approximate error in the imaging conditions. X-ray tomograms typically exhibit higher levels of noise than 2D optical images, and this noise will limit the accuracy of the strain computation. We quantify noise using the Noise to Signal Ratio (NSR), defined as

$$NSR = \frac{\sigma_{noise}}{I_{max} - I_{min}} \tag{2.3}$$

where σ_{noise} is the standard deviation of the noise, and $I_{max} - I_{min}$ is the intensity range in the signal. Our experimental results using laboratory-based XCT equipment yielded tomograms with NSR of ~3%, whereas tomograms from synchrotron or more modern XCT systems could produce lower noise levels. A sensitivity study found that error in strain computation due to NSR remained below 0.0001, which was insignificant relative to the effect of a fragile speckle pattern (with $\sigma_\varepsilon \approx 0.001 - 0.01$). Therefore, simulations were performed with a representative NSR of 3%.

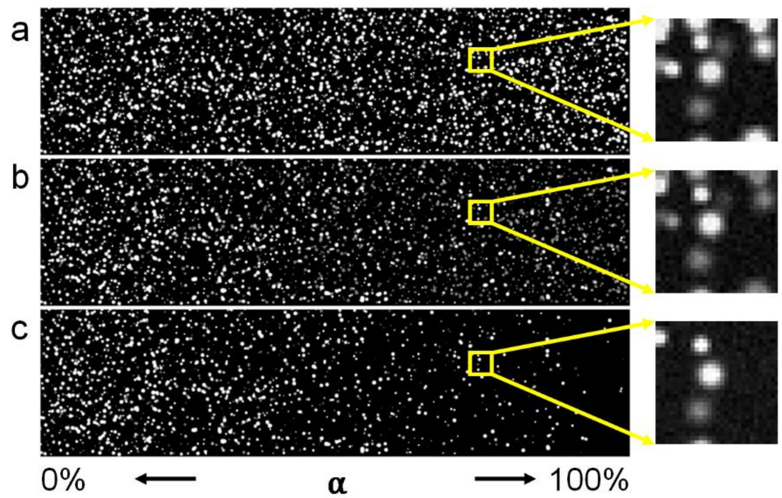

Fig. 2.7. Damage gradient in synthetic zero-strain images (a-c) Corresponding 2D slices with (a) $C = 1.0$, (b) $C = 0.5$, and (c) $C = 0.0$. Insets on right indicate subset size (29^3 voxels) used in DVC analysis, and highlight how selected markers gradually faded with decreasing C. $\phi = 0.137$. Images are 1024×256 voxels in size.

5.2. DVC analysis

DVC analysis was performed using the commercial Vic-Volume DVC software (Correlated Solutions) with parameters that matched the experimental error analysis (subset size of 29^3 voxels and step size of 10 voxels). These parameters resulted in ~50,000 subsets per volume, and 529 subsets for a given fraction of damaged markers. Strain measurement was again performed with a strain filter of size $[5]^3$ subsets, which was the minimum amount of filtering in the DVC software. Additional analyses were performed with a range of subset sizes to assess the sensitivity to this parameter.

6. Numerical results

6.1. Effect of speckle pattern degradation

Analysis of the zero-displacement simulations clearly revealed that the average marker volume fraction ϕ, the fraction of damaged markers α, and the residual contrast of damaged markers C strongly influenced the accuracy of the displacement computations, as summarized in Fig. 2.8. Results are presented for three different volume fractions that corresponded to those used in the experiments, and error is defined as the standard deviation of the measured artificial displacement.

Similar to the experimental results, there appeared to exist two domains for displacement computation. During the initial stable computation regime, the displacement error increased linearly with respect to α. This continued until a critical damage value was reached, after which the computation became unstable and error increased rapidly. Below the critical level of speckle pattern degradation, the error increased gradually with α but remained relatively small; in the worst-case scenario with $\phi = 0.137$ and $C = 0.0$, the error remained less than 0.2 voxels throughout the stable DVC regime. The transition into the unstable regime is identified by the inflection point in the plots, which varied slightly with ϕ and C; values of this transition point (for $C = 0.0$) ranged from $\alpha = 0.62$ for $\phi = 0.137$, $\alpha = 0.68$ for $\phi = 0.217$, and $\alpha = 0.70$ for $\phi = 0.404$. The magnitude of error in the stable measurement regime varied with the residual contrast of the damaged speckles C and the volume fraction of speckles in the image ϕ. In general, error improved with increasing ϕ and C. This was qualitatively consistent with the experiments, which also found that the high ϕ specimens exhibited a lower noise floor than low

ϕ specimens.

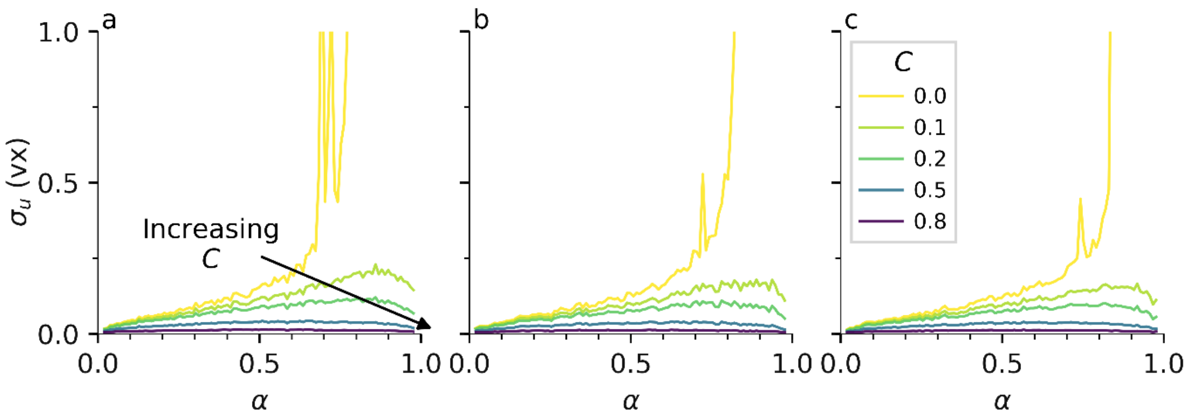

Fig. 2.8. Effect of speckle pattern degradation and volume fraction ϕ on displacement error. (a-c) Results for ϕ of (a) 0.137, (b) 0.217, and (c) 0.404. NSR = 3%.

Equivalent analysis on the strain error identified similar nonlinearities in the measurement precision, as revealed in Fig. 2.9. Specifically, the strain error increased linearly until a critical fraction of particles had disappeared, which was approximately identical to that identified in the displacement analysis. This transition point occurred at strain error of ≈ 0.0025 (250 $\mu\varepsilon$); this critical value (at $C = 0$) ranged from $\alpha = 0.48$ for $\phi = 0.137$, $\alpha = 0.60$ for $\phi = 0.217$, and $\alpha = 0.67$ for $\phi = 0.404$. Below this point, strain error increased linearly with α. Again, the error decreased with larger ϕ and C.

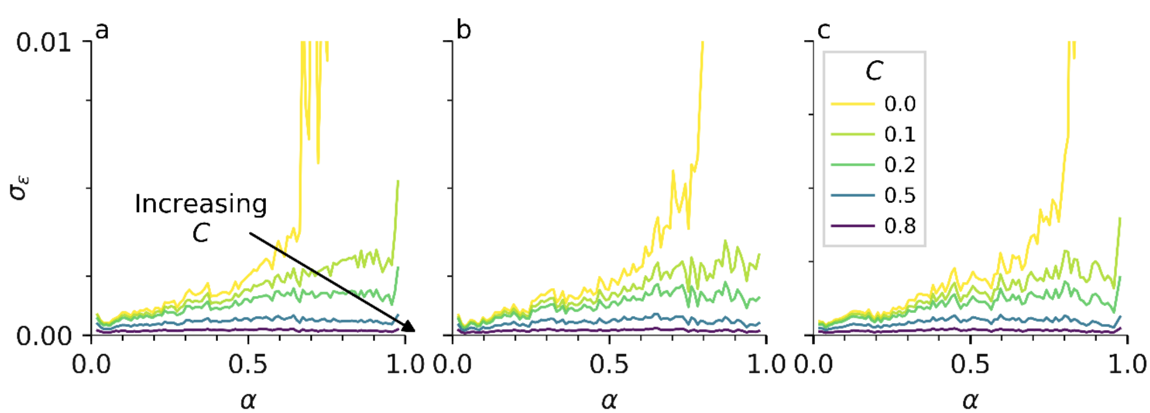

Fig. 2.9. Effect of speckle pattern degradation and volume fraction ϕ on strain error. (a-c) Results for ϕ of (a) 0.137, (b) 0.217, (c) 0.404. NSR = 3%.

6.2. Effect of subset size

Using the same synthetic tomograms (for $C = 0$), the DVC analysis was repeated to understand the effect of subset size on displacement error. These results are shown in Fig. 2.10, which highlight the stabilizing benefit of large subset size M on the DVC-measured displacement. These benefits were especially pronounced at low volume fractions: for $\phi = 0.137$, a displacement error of $\sigma_u = 0.25$ voxels was achieved at $\alpha = 0.47$ for $M = 21$ voxels, but at $\alpha = 0.78$ for $M = 31$ voxels. In contrast, with a denser speckle pattern of $\phi = 0.422$, the change in subset size from $M = 21$ to 31 voxels increased the DVC stability from $\alpha = 0.62$ to 0.88. Thus, an experimentalist can effectively adjust the subset size to compensate for speckle pattern degradation; of course, this benefit would also come at the cost of the measurement's spatial resolution.

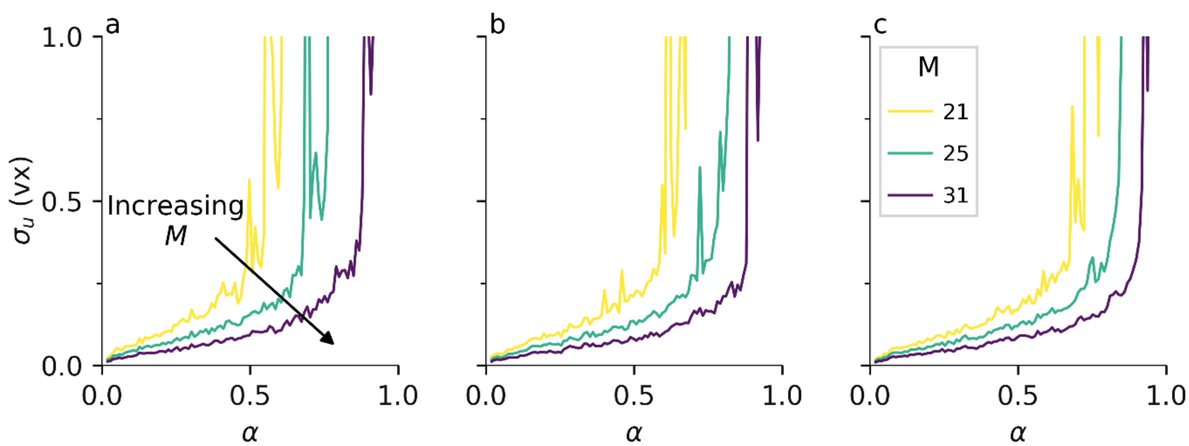

Fig. 2.10. Effects of subset size M on displacement error for ϕ of (a) 0.137, (b) 0.217, and (c) 0.404. $C = 0$, NSR = 3%.

7. Theoretical analysis

7.1. Predicting DVC instability due to fragile microstructures

The observed trends with regards to speckle pattern damage, subset size, and speckle volume fraction can be reconciled with existing theories of DIC/DVC error. Specifically, the following can be asserted:

- An increasing fraction of damaged speckles (α) will increase the mismatch between the reference and deformed subset, thereby increasing DVC error.
- For constant α, a larger subset will retain more intact speckles in the deformed subset. Accordingly, the subset size M may be used to improve DVC accuracy in cases of pattern degradation.
- Similarly, a larger volume fraction ϕ of speckles will increase the number of intact speckles and improve measurement precision.

In the following section, these deductions are formalized in terms of the Sum of Subset Squared Image Gradients (SSSIG) criterion proposed by Pan [34]. In Pan's work, the DVC displacement error was quantitatively related to the image intensity gradients used for subvoxel interpolation in each subset. Ultimately, this analysis showed that the standard deviation of displacement error σ_{u_i} scales proportional to variance of the image noise $D(\eta)$ and inversely with SSSIG

$$\sigma_{u_i} \propto \left(\frac{D(\eta)}{\Sigma_S \left(\frac{\partial G}{\partial x_i} \right)^2} \right)^{0.5} \tag{2.4}$$

where Σ_s refers to a summation over all voxels in the subset, and G is the deformed tomogram with damaged speckles.

With some modifications, the SSSIG criterion is shown to accurately predict the DVC instability associated with severe speckle pattern degradation for a variety of speckle patterns and DVC parameters. In this analysis, the results from subset-based sensitivity study described in the section **Effect of subset size** are used to demonstrate this behavior. Accordingly, their comparison is restricted to images with consistent speckle geometry, DVC step size, and image noise.

The analysis assumes that the images exhibit the following characteristics

- Uniform speckle size, shape and contrast, with non-overlapping speckles
- The average spacing of speckles can be characterized by a wavelength λ
- DVC analysis is performed with cubic subsets of size M
- Consistent, independent noise for each voxel

Given these conditions, SSSIG can be defined precisely by the number of intact speckles in each subset

$$\sum_S \left(\frac{\partial G}{\partial x_i}\right)^2 = \mathcal{G}_i N_{intact} \tag{2.5}$$

where $N_{intact} = (1-\alpha)N_{speckles}$ and $N_{speckles} = \left(\frac{M}{\lambda}\right)^3$. $\mathcal{G}_i$ describes the individual contribution of each speckle to the SSSIG, $\mathcal{G}_i = \sum_s \left(\frac{\partial I_{speckle}(\boldsymbol{x})}{\partial x_i}\right)^2$, with $I_{speckle}$ as defined in Eq. 2.2 above.

Under this model, the DVC displacement error should scale inversely with N_{intact} for all combinations of M and ϕ (which is interchangeable with λ). This is tested in Fig. 2.11, which indeed reveals a consistent transition point between “stable” and “unstable” DVC measurement errors based on N_{intact}. Specifically, σ_u increased linearly until $N_{intact} = 11 - 20$ speckles, and increased rapidly for subsequent deletion of speckles. This threshold was valid for the wide range of $N_{speckles}$ from 26 and 150 in the undamaged state, and no obvious trends in the critical N_{intact} were identified with respect to either M or ϕ. As a result, it is postulated that this represents the minimum number of intact features for accurate DVC analysis.

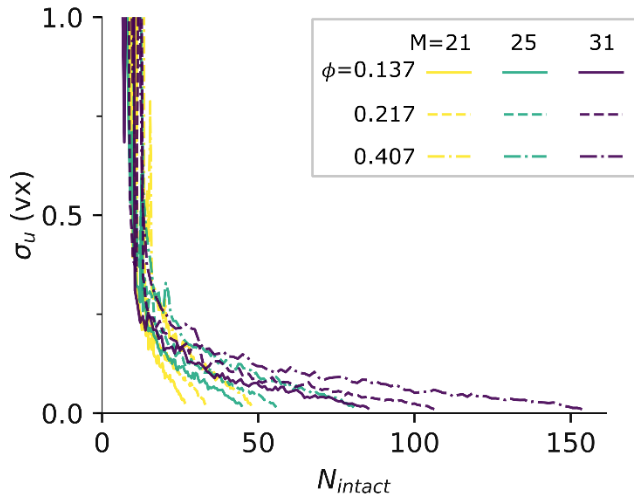

Fig. 2.11. Normalized model of DVC error for different combinations of subset size M and volume fraction ϕ.

7.2. Effect of damage on correlation strength

It is further speculated that the effects of damage on DVC error can be related to the correlation strength C_{ZNCC}. This is validated using two sets of 2D synthetic images of size 384^2 pixels (Fig. 2.12a), which were generated according to the methods described in the previous section **Generation of synthetic images**. In the first set, individual markers were damaged by a "fading" technique. In the second, the width of the markers was "shrunk" in proportion to the speckle damage. While both sets of images were identical in the undamaged and fully damaged states, the intermediate states were somewhat different. The undamaged images included a speckle fraction of $\phi = 0.26$. Half of the markers ($\alpha = 0.5$) were flagged for damage, while the other half of the speckles remained unchanged in the degraded images. The contrast C was reduced incrementally between images, which approximated the collapse of GMBs in the syntactic foam.

Results of the simulation in Fig. 2.12b indicated that the two damage mechanisms both reduced C_{ZNCC} nonlinearly. Reductions in C_{ZNCC} can hinder local optimization schemes from successfully identifying the appropriate correlation peak [22,35], leading to spurious displacement and strain measurements. Indeed, many commercial DIC and DVC software packages are configured to ignore subsets with poor correlation; in this case, severe decorrelation due to speckle pattern degradation would prevent any displacement measurement at all! Remarkably however, C_{ZNCC} remained above 0.9 for $C \geq 0.5$. While arbitrary, this threshold has been previously used to update the reference image in incremental DIC schemes and preserve measurement accuracy for large deformations [36,37]. Given that the measurement accuracy scales with the correlation strength, it seems reasonable that DVC measurements could tolerate minor degradation to the speckle pattern, but become increasingly sensitive to subsequent damage.

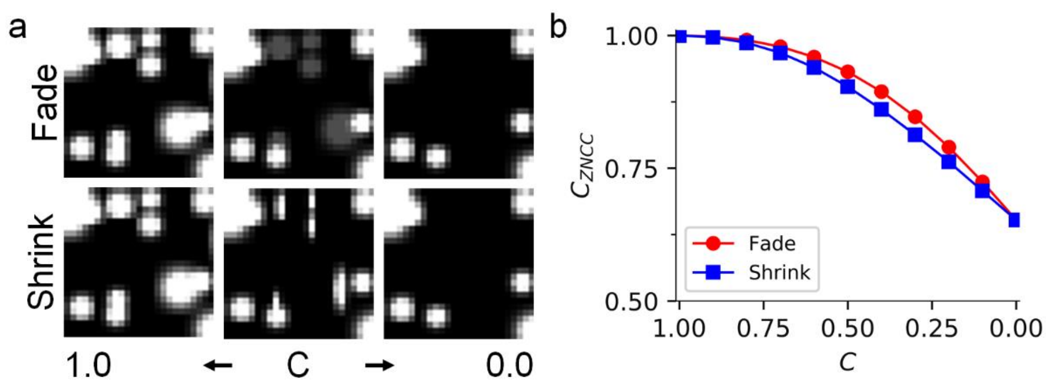

Fig. 2.12. Effect of “Fade” and “Shrink” speckle degradation mechanisms on DVC. (a) Schematic of the two mechanisms, shown with synthetic images of size 25×25 pixels. (b) Resulting ZNCC scores as function of residual contrast C. $\alpha = 0.5$ of speckles were flagged for damage.

8. Discussion

8.1. Comparison between experiment and numerical results

Most importantly, these results showed that accurate DVC measurements can be obtained despite non-trivial levels of degradation to the speckle pattern. This was confirmed using both experimental tomograms and numerically-generated images with controlled levels of speckle pattern degradation. In both cases, DVC error remained small while below a critical level of degradation (*i.e.,* the stable measurement regime), after which strain error rapidly increased to unacceptable levels (unstable measurement regime). Thus, the transition between stable and unstable measurement regimes reflected the degradation of the speckle pattern rather than peculiarities of the syntactic foams used in experiments. Fundamentally, this appeared to be related to the effects of speckle pattern degradation on the correlation strength C_{ZNCC}. The nonlinear dependence of C_{ZNCC} on degradation allowed C_{ZNCC} to remain high after the disappearance of a small fraction of speckles, but C_{ZNCC} rapidly decreased with further degradation.

Despite this, several key differences were observed between the two analyses. First, DVC error analysis of the experimental and numerically-generated images revealed different trends within the stable measurement regime. In particular, the experimental results suggested a constant error of $\sigma_u = 0.025 - 0.05\ voxels$ and $\sigma_\varepsilon = 50 - 100\ \mu\varepsilon$ for all levels of degradation beneath the critical value, while the numerical images suggested a *linearly increasing* error within this range (for constant C). The likely explanation of this trend was that the effective C for the collapsed GMBs was not constant but decreased throughout the experiment. Initially, the Feret shape of damaged particles would be small, such that the particle would be pseudo-spherical and would provide strong residual contrast C in the tomogram. Subsequent loading would further compress the particles, increasing Feret shape and decreasing C. At small deformations, the typical C would remain large enough to negligibly affect the error. For example, from Figs. 2.8 and 2.9 it was shown that displacement or strain error did not substantially increase with $C \approx 0.5$ regardless of the fraction of speckles damaged. This allowed error to remain low when the GMBs were partially collapsed, but to rapidly increase as the damaged particles fully closed.

Second, analysis of the numerically-generated images predicted critical damage levels that were higher than those observed in the experiment. Plausibly, damage localization in the experiment contributed to the increased error. Detailed analysis of the tomograms showed that bands of elevated strain (visible in Fig. 2.5) corresponded to regions with clusters of crushed GMBs, such the speckle pattern damage would locally exceed the global average and therefore increase the measurement error. This behavior was caused by particle-to-particle interactions [38] and local clustering of GMBs [27], and was particularly severe in the high volume fraction specimens ($\phi = 0.422$ and to a lesser extent $\phi = 0.225$).

8.2. Implications

The ability to accurately correlate heavily damaged speckle patterns should enable DVC-based strain measurements in a broad class of materials with fragile microstructures, including syntactic foams and possibly many other materials. This was previously thought to be impossible or ill-advised at best, since it would violate the principle of gray-level conservation. In contrast, our experiments showed that roughly 30-40% of speckles could disappear before strain error noticeably worsened to $\sigma_\varepsilon > 0.01$. Intriguingly, adjusting the subset size may be a viable technique to enable accurate DVC measurements in cases of even more severe degradation. In particular, analysis of the simulated images suggested that DVC analysis remained stable as long as each subset contained a minimum of $N_{intact} = 20$ speckles. In any case, rigid body motion experiments are essential to assess the error due to speckle pattern degradation, and should be included in any experimental protocol where results may be affected by microstructural damage.

The current findings were only obtained for particle-based speckle patterns, where damage resulted in the disappearance of particles in the pattern. Therefore, it remains unclear how other types of speckle patterns and damage mechanisms affect the stability of DVC measurements. Future work is required to assess this behavior in granular, foam or fibrous composites, and also materials that undergo different damage mechanisms such as microcracking or cell collapse. Simulation of these effects using numerically generated images may prove a cost-effective manner to test viability of DVC measurement in these other materials.

Finally, these results demonstrate the importance of restricting DVC measurement to scenarios with sub-critical levels of speckle pattern degradation. For the current syntactic foam, this was achieved by relating damage to the uniaxial deformation, which was found to reliably correspond to DVC error across multiple samples with identical GMB volume fractions. Similar testing should be performed on other materials to avoid inaccurate strain measurements. Alternatively, in the case of super-critical speckle pattern degradation, the spatial distribution of subsets with large strain error could be used to identify regions of severe microstructural damage.

It becomes more challenging to define the critical level of speckle pattern degradation when damage is locally concentrated rather than homogeneously dispersed throughout the material, which would cause DVC error to increase more rapidly near the location of damage. While a straightforward but cautious approach would be to manually trim the region of interest around the damaged regions, this can be tedious and also disposes of many accurate correlation points. Since the speckle pattern degradation reduces the correlation strength, it may be possible to introduce automatic screening of each correlated subset. One intriguing avenue for evaluating the quality of the experimental strain measurement is to implement so-called q-factor DVC, which assesses the sharpness and uniqueness of the cross-correlation through image quality factors [35]. Q-factor DVC was originally developed for cases of large deformation, which causes round speckles to collapse into ellipses and is comparable to the collapse of GMBs in the syntactic foam. Additionally, this work can be integrated into the framework for incremental DIC/DVC techniques [36,37] to indicate when the reference image should be updated.

9. Conclusions

Accurate DVC measurements were obtained during *in situ* testing of specimens with fragile microstructures even with widespread damage to the speckle pattern. This was validated using experiments on three types of syntactic foams with different volume fractions of glass microballoon reinforcement, as well as analysis of numerically-generated images with controlled levels of speckle pattern degradation; in both cases, correlation succeeded despite large proportions of individual markers in the speckle pattern disappearing between the reference and deformed states up to 20-35% compression and 30-40% damaged speckles. These findings justify the use of DVC on many types of materials with unstable microstructures, including syntactic foams, ceramic composites, bone and others. From these analyses, the following conclusions are made:

- The performance of DVC as a function of speckle pattern degradation was classified into two regimes. Below a critical level of speckle degradation, DVC measurement was “stable” and error approached the experimental noise floor. The displacement and strain errors were constant within this regime, and varied inversely with the speckle pattern density. Above this critical value, measurement became “unstable” and error rapidly increased with further degradation to the speckle pattern.
- In the experiments, the transition from stable to unstable measurement regimes

typically occurred after 30-40% of the speckles were damaged. This critical value depended on several factors including pattern quality, marker volume fraction and the degree of damage localization. In particular, larger volume fractions of markers tend to stabilize the DVC measurements to accommodate more severe damage to the speckle pattern.

- The experimental trends were qualitatively replicated using numerically-generated images, which successfully captured the transition between stable and unstable measurement regimes. However, the numerical analysis tended to overestimate transition between these two regimes, likely due to subtle differences in the damage mechanisms between the syntactic foam and the simulated images. Despite this, numerically-generated images may be used to preliminarily simulate the viability of DVC measurements in other types of fragile speckle patterns, such as those found in foams or fiber-reinforced composites.
- The effect of damage on measurement error was reconciled with the Sum of Subset Squared Image Gradients (SSSIG) criterion proposed by Pan [34]. Using numerically generated images, the displacement error was shown to scale inversely with the number of intact N_{intact} speckles in each subset, and DVC instability was triggered at roughly constant N_{intact} for a variety of speckle patterns and DVC parameters. Accordingly, larger subset sizes may be used to compensate for sparse speckle patterns or severe pattern degradation.

References

[1] M.A. Sutton, W. Wolters, W.H. Peters, W. Ranson, S.R. McNeill, Determination of displacements using an improved digital correlation method, Image Vis. Comput. 1 (1983) 133–139. doi:10.1016/0262-8856(83)90064-1.

[2] B.K. Bay, T.S. Smith, D.P. Fyhrie, M. Saad, Digital volume correlation: Three-dimensional strain mapping using X-ray tomography, Exp. Mech. 39 (1999) 217–226. doi:10.1007/BF02323555.

[3] M.A. Sutton, J.-J. Orteu, H.W. Schreier, Image Correlation for Shape, Motion and Deformation Measurements, Springer US, Boston, MA, 2009. doi:10.1007/978-0-387-78747-3.

[4] Y.L. Dong, B. Pan, A Review of Speckle Pattern Fabrication and Assessment for Digital Image Correlation, Exp. Mech. 57 (2017) 1161–1181. doi:10.1007/s11340-017-0283-1.

[5] B.K. Bay, Methods and applications of digital volume correlation, J. Strain Anal. Eng. Des. 43 (2008) 745–760. doi:10.1243/03093247JSA436.

[6] B.P. Croom, P. Xu, E.J. Lahoda, C.P. Deck, X. Li, Quantifying the three-dimensional damage and stress redistribution mechanisms of braided SiC/SiC composites by in situ volumetric digital image correlation, Scr. Mater. 130 (2017) 238–241. doi:10.1016/j.scriptamat.2016.12.021.

[7] L. Saucedo-Mora, T. Lowe, S. Zhao, P.D. Lee, P.M. Mummery, T.J. Marrow, In situ observation of mechanical damage within a SiC-SiC ceramic matrix composite, J. Nucl. Mater. 481 (2016) 13–23. doi:10.1016/j.jnucmat.2016.09.007.

[8] L. Saucedo-Mora, M. Mostafavi, D. Khoshkhou, C. Reinhard, R. Atwood, S. Zhao, B. Connolly, T.J. Marrow, Observation and simulation of indentation damage in a SiC-SiCfibre ceramic matrix composite, Finite Elem. Anal. Des. 110 (2016) 11–19. doi:10.1016/j.finel.2015.11.003.

[9] V. Mazars, O. Caty, G. Couégnat, A. Bouterf, S. Roux, S. Denneulin, J. Pailhès, G.L. Vignoles, Damage investigation and modeling of 3D woven ceramic matrix composites from X-ray tomography in-situ tensile tests, Acta Mater. 140 (2017) 130–139. doi:10.1016/j.actamat.2017.08.034.

[10] A. Bouterf, E. Maire, S. Roux, F. Hild, X. Brajer, E. Gouillart, E. Boller, Analysis of compaction in brittle foam with multiscale indentation tests, Mech. Mater. 118 (2018) 22–30. doi:10.1016/j.mechmat.2017.12.004.

[11] S.M. Barhli, L. Saucedo-Mora, M.S.L. Jordan, A.F. Cinar, C. Reinhard, M. Mostafavi, T.J. Marrow, Synchrotron X-ray characterization of crack strain fields in polygranular graphite, Carbon N. Y. 124 (2017) 357–371. doi:10.1016/J.CARBON.2017.08.075.

[12] F. Hild, A. Bouterf, S. Roux, Damage measurements via DIC, Int. J. Fract. 191 (2015) 77–105. doi:10.1007/s10704-015-0004-7.

[13] V. Valle, P. Bokam, A. Germaneau, S. Hedan, New Development of Digital Volume Correlation for the Study of Fractured Materials, Exp. Mech. (2018) 1–15. doi:10.1007/s11340-018-0415-2.

[14] J. Rannou, N. Limodin, J. Réthoré, A. Gravouil, W. Ludwig, M.-C. Baïetto-Dubourg, J.-Y. Buffière, A. Combescure, F. Hild, S. Roux, Three dimensional experimental and numerical multiscale analysis of a fatigue crack, Comput. Methods Appl. Mech. Eng. 199 (2010) 1307–1325. doi:10.1016/J.CMA.2009.09.013.

[15] S. Roux, F. Hild, P. Viot, D. Bernard, Three-dimensional image correlation from X-ray computed tomography of solid foam, Compos. Part A Appl. Sci. Manuf. 39 (2008) 1253–1265. doi:10.1016/j.compositesa.2007.11.011.

[16] A. Bouterf, S. Roux, F. Hild, J. Adrien, E. Maire, S. Meille, Digital volume correlation applied to X-ray tomography images from spherical indentation tests on lightweight gypsum, Strain. 50 (2014) 444–453. doi:10.1111/str12101.

[17] F. Pierron, S.A. McDonald, D. Hollis, J. Fu, P.J. Withers, A. Alderson, Comparison of the mechanical behaviour of standard and auxetic foams by x-ray computed tomography and digital volume correlation, Strain. 49 (2013) 467–482. doi:10.1111/str.12053.

[18] E. Verhulp, B. van Rietbergen, R. Huiskes, A three-dimensional digital image correlation technique for strain measurements in microstructures, J. Biomech. 37 (2004) 1313–1320. doi:10.1016/j.jbiomech.2003.12.036.

[19] F. Forsberg, C.R. Siviour, 3D deformation and strain analysis in compacted sugar using x-ray microtomography and digital volume correlation, Meas. Sci. Technol. 20 (2009) 095703. doi:10.1088/0957-0233/20/9/095703.

[20] M. Bornert, N. Lenoir, P. Bésuelle, Y. Pannier, S. a. Hall, G. Viggiani, J. Desrues, Discrete and continuum analysis of localised deformation in sand using X-ray μCT and volumetric digital image correlation, Géotechnique. 60 (2010) 315–322. doi:10.1680/geot.2010.60.5.315.

[21] B.P. Croom, H. Jin, B. Mills, J. Carroll, K. Long, J. Brown, X. Li, Damage mechanisms in elastomeric foam composites: Multiscale X-ray computed tomography and finite element analyses, Compos. Sci. Technol. 169 (2019) 195–202. doi:10.1016/j.compscitech.2018.11.025.

[22] B. Pan, K. Qian, H. Xie, A. Asundi, Two-dimensional digital image correlation for in-plane displacement and strain measurement: a review, Meas. Sci. Technol. 20 (2009) 062001. doi:10.1088/0957-0233/20/6/062001.

[23] B.P. Croom, W.-M. Wang, J. Li, X. Li, Unveiling 3D Deformations in Polymer Composites by Coupled Micro X-Ray Computed Tomography and Volumetric Digital

Image Correlation, Exp. Mech. 56 (2016) 999–1016. doi:10.1007/s11340-016-0140-7.

[24] B.M. Patterson, J.P. Escobedo-Diaz, D. Dennis-Koller, E. Cerreta, Dimensional quantification of embedded voids or objects in three dimensions using X-ray tomography., Microsc. Microanal. 18 (2012) 390–8. doi:10.1017/S1431927611012554.

[25] B.M. Patterson, N.L. Cordes, K. Henderson, J.J. Williams, T. Stannard, S.S. Singh, A.R. Ovejero, X. Xiao, M. Robinson, N. Chawla, In situ X-ray synchrotron tomographic imaging during the compression of hyper-elastic polymeric materials, J. Mater. Sci. 51 (2016) 171–187. doi:10.1007/s10853-015-9355-8.

[26] N. Gupta, Kishore, E. Woldesenbet, S. Sankaran, Studies on compressive failure features in syntactic foam material, J. Mater. Sci. 36 (2001) 4485–4491. doi:10.1023/A:1017986820603.

[27] M. Yu, P. Zhu, Y. Ma, Effects of particle clustering on the tensile properties and failure mechanisms of hollow spheres filled syntactic foams: A numerical investigation by microstructure based modeling, Mater. Des. 47 (2013) 80–89. doi:10.1016/j.matdes.2012.12.004.

[28] B.P. Croom, H. Jin, J. Carroll, K. Long, X. Li, Particle clustering effects on damage mechanisms in syntactic foams, Submitted. (2018).

[29] J. Adrien, E. Maire, N. Gimenez, V. Sauvant-Moynot, Experimental study of the compression behaviour of syntactic foams by in situ X-ray tomography, Acta Mater. 55 (2007) 1667–1679. doi:10.1016/j.actamat.2006.10.027.

[30] N. Limodin, J. Réthoré, J. Adrien, J.-Y. Buffière, F. Hild, S. Roux, Analysis and Artifact Correction for Volume Correlation Measurements Using Tomographic Images from a Laboratory X-ray Source, Exp. Mech. 51 (2011) 959–970. doi:10.1007/s11340-010-9397-4.

[31] P. Mazzoleni, F. Matta, E. Zappa, M.A. Sutton, A. Cigada, Gaussian pre-filtering for uncertainty minimization in digital image correlation using numerically-designed speckle patterns, Opt. Lasers Eng. 66 (2015) 19–33. doi:10.1016/j.optlaseng.2014.08.004.

[32] J. Lachambre, E. Maire, J. Adrien, D. Choqueuse, In situ observation of syntactic foams under hydrostatic pressure using X-ray tomography, Acta Mater. 61 (2013) 4035–4043. doi:10.1016/j.actamat.2013.03.017.

[33] N. Gupta, A functionally graded syntactic foam material for high energy absorption under compression, Mater. Lett. 61 (2007) 979–982. doi:10.1016/j.matlet.2006.06.033.

[34] B. Pan, H. Xie, Z. Wang, K. Qian, Z. Wang, Study on subset size selection in digital image correlation for speckle patterns, Opt. Express. 16 (2008) 7037. doi:10.1364/OE.16.007037.

[35] A.K. Landauer, · M Patel, · D L Henann, · C Franck, A q-Factor-Based Digital Image

Correlation Algorithm (qDIC) for Resolving Finite Deformations with Degenerate Speckle Patterns, Exp. Mech. 58 (2018) 815–830. doi:10.1007/s11340-018-0377-4.

[36] B. Pan, W. Dafang, X. Yong, Incremental calculation for large deformation measurement using reliability-guided digital image correlation, Opt. Lasers Eng. 50 (2012) 586–592. doi:10.1016/j.optlaseng.2011.05.005.

[37] Z. Hu, H. Luo, S.G. Bardenhagen, C.R. Siviour, R.W. Armstrong, H. Lu, Internal Deformation Measurement of Polymer Bonded Sugar in Compression by Digital Volume Correlation of In-situ Tomography, Exp. Mech. 55 (2015) 289–300. doi:10.1007/s11340-014-9856-4.

[38] G. Tagliavia, M. Porfiri, N. Gupta, Analysis of particle-to-particle elastic interactions in syntactic foams, Mech. Mater. 43 (2011) 952–968. doi:10.1016/j.mechmat.2011.08.008.

Chapter 3:
Damage mechanisms in elastomeric foam composites: Multiscale X-ray computed tomography and finite element analyses

1. Introduction

Syntactic foams are lightweight polymeric composites reinforced with hollow glass microballoon (GMB) particles. Under uniaxial compression, the foam deforms in three stages [1], including a stiff elastic response before GMB collapse, propagating GMB collapse over relatively constant load, and densification after nearly all GMBs have collapsed. These GMB deformation mechanisms produce an “S-shaped” stress-strain curve characterized by high specific elastic stiffness, hysteresis and energy absorption, making syntactic foams promising lightweight structural materials for many applications. However, a key outstanding challenge in the design and modeling of syntactic foams is predicting the onset and duration of GMB collapse, as these two parameters govern the energy absorption of the foam. Here, onset of damage refers to the “initiation” of the first damage observed within a local subset of GMBs, and “propagation” refers to subsequent damage to the adjacent particles.

At the heart of the issue is confusion over the precise mechanisms that lead to damage initiation and propagation due to complex dependency on GMB geometry and mechanical properties. Changes in the syntactic foam microstructure due to GMB diameter, wall thickness, volume fraction and interfacial characteristics can have pronounced effects on the mechanical response and onset of damage [2–5]. Moreover, the performance of syntactic foams is intrinsically stochastic, since damage initiation depends on the random packing of individual GMBs [6]. Still, it remains unclear how the interaction between adjacent particles contributes to damage initiation, and how previously damaged GMBs can influence the propagation of damage to adjacent particles.

This has motivated the use of *in situ* X-ray Computed Tomography (XCT) mechanical testing to visualize the 3D foam microstructure and damage behavior [7–9], as well as micro-mechanics finite element models that include detailed representations of GMBs and the matrix [9,10]. *In situ* XCT allows for quantitative measurement of individual GMBs and their spatial arrangement, thus providing an ideal platform for identifying the mechanisms of damage within the foam. Prior experiments have shown, for instance, that the stiffness of the polymer matrix regulates the distribution of GMB failure [7]. Stiff polymer matrices such as epoxies induce damage along local failure bands, whereas rubbery matrices promote more evenly distributed GMB collapse. The syntactic foam studied in the current work features an elastomeric silicone (PDMS) matrix that is poorly studied but is believed to cause dispersed GMB collapse [11].

However, both the *in situ* XCT experiments and micromechanics models suffer the same limitation due to a restricted measurement volume. Experimentally, the XCT images must provide sufficient resolution to capture the failure of individual GMBs, limiting the overall field of view to ~1 mm^3. Similarly, the level of detail required in the finite element mesh allows simulation of only ~100 GMBs before the model becomes prohibitively large. Therefore, while the high-resolution tomograms may effectively capture the damage initiation behavior, it remains unclear if the small-scale experimental and numerical results accurately capture the damage propagation mechanisms in large specimens.

1.1. Digital volume correlation: Application to syntactic foam

One strategy to overcome this restriction is to employ multiscale *in situ* XCT mechanical testing. As in previous experiments, analysis of high-resolution tomograms can directly reveal the damage initiation and propagation mechanisms within a selected region of interest within the specimen. Next, quantitative deformation and strain analysis of low-resolution tomograms using

Digital Volume Correlation (DVC) can test if the deformation patterns observed at high resolution also hold at larger length scales. A particular advantage of the DVC-based measurement is the superior displacement resolution of 0.01-0.1 voxels [12], which allows sensitive measurements to be obtained at large fields of view. Conceptually, DVC strain fields can detect damage in the composite due to changes in the local composite stiffness before and after GMB collapse. Therefore, the local strain field reflects the damage mechanisms observed at high resolution; for example, the formation of crush bands under compression [7] would produce bands of high axial strain. This chapter employs the DVC framework established in Chapter 1.

1.2. Organization of chapter

In this chapter, *in situ* XCT uniaxial compression testing is used to study the damage mechanisms of elastomeric syntactic foam specimens. In contrast to prior experiments that relied on qualitative measurements at restricted fields of view, we present quantitative analysis of damage at multiple length scales. Direct image segmentation and processing of high-resolution tomograms reveal the mechanics of GMB collapse, and indirect measurements of damage using DVC-measured strain fields identify the formation of pseudo-crush bands at longer length scales. From these measurements, a new mechanism is presented to explain the observed damage initiation and propagation behavior, which is supported by a parametric finite element analysis of a model syntactic foam system.

2. Materials and methods

2.1. Sample preparation

Sylgard GMB specimens were prepared by mixing two-part Sylgard 184 silicone elastomer (Dow Corning) with A16 glass microballoons (3M) and curing agent. The mixture was injected into a cylindrical syringe and cured at room temperature with an accelerator. The diameter of A16 GMBs ranges from 30 to 95 µm within 10-90% distribution, with a mean diameter of 60 µm. The particular Sylgard GMB specimen used in this experiment had a nominal volume fraction of 35%. After curing, the cylinder specimen was removed from the mold and then carefully sliced into shorter cylinders with 7 mm height and diameters of 4.8 mm.

2.2. In situ experiments

In situ compression experiments (Fig. 3.1) of the syntactic foam specimens were performed inside an X-Radia 520 Versa machine. Tomograms were acquired at the original undeformed state as well as at global engineering strain increments of 7% up to 50% compression at two resolutions (high resolution of 1.7 µm per voxel, and low resolution of 10 µm per voxel) to simultaneously image the collapse of GMBs with high detail, and also capture the macroscopic global deformation. Special care was taken to align the high-resolution tomograms at different loading steps so that the behavior of individual GMBs from the same set could be tracked. In order to accommodate the specimen's viscoelastic response, the load was allowed to stabilize for thirty minutes before acquiring the next tomogram. We note that the shape of the *in situ* loading curve differed slightly from the continuous loading curve, which was tentatively attributed to time-dependent damage and matrix viscoelasticity; these effects were not due to compliance in the loading stage.

Quantitative image analysis of the high-resolution tomograms provided measurements of GMB collapse as a function of load (Fig. 3.1a). Standard image processing techniques were implemented in 3D using Avizo 9.0 software to denoise, segment, label and measure individual GMBs. The GMBs were classified into *intact* and *fractured* based on Feret shape, which provided a 3D measure of the GMB aspect ratio. Thresholding of the Feret shape (where FS >

1.5) identified collapsed GMBs. Analysis of these trends showed continued GMB collapse over a range of compression from 14% to beyond 50%. Wrinkling on the specimen surface at higher strains also confirmed widespread collapse of GMBs and the presence of crush bands (visible in Fig. 3.1b-e).

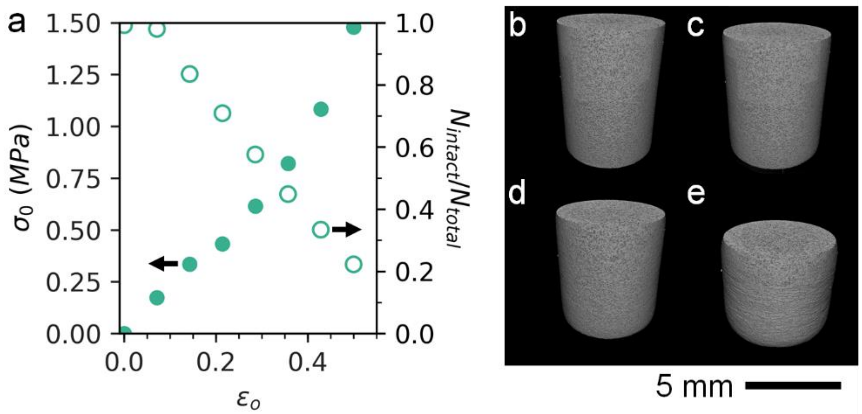

Fig. 3.1. Summary of experimental results. (a) Measured engineering stress and fraction of intact GMBs (from high-resolution tomogram) as a function of engineering strain. (b-e) Renderings of specimen at engineering strains of (b) $\varepsilon_0 = 0.00$, (c) $\varepsilon_0 = -0.07$, (d) $\varepsilon_0 = -0.21$, (e) $\varepsilon_0 = -0.35$.

Correlation of the tomograms by Vic-Volume DVC software (Correlated Solutions) extracted quantitative, full-field kinematic measurements using analysis procedures similar to [13,14]. Before analysis, all 16-bit tomograms were denoised with a Gaussian filter and then quantized to 8-bit images. Subset sizes of 25^3 voxels (250^3 μm) and step sizes of 3 voxels were selected. Strain was computed with a filter size of 9^3 subsets, resulting in a virtual strain gage size of $[520\ \mu m]^3$. This resolution was much coarser than the size of individual GMBs, but still quantified the aggregate compression due to collapse of selected GMBs within each subset.

2.3. DVC error analysis

The collapse of GMBs and their disappearance from the tomograms violates an assumption of grayscale continuity that is necessary for accurate DVC measurement [12], such that damage to GMBs degrades the quality of the DVC strain measurement. This mandated judicial interpretation of the DVC-measured strain fields. Therefore, measurement error was assessed using rigid body motion experiments in both the undeformed and damaged states. In the reference condition (prior to GMB collapse), the maximum measured artificial strain was $\Delta\varepsilon^{max} = 0.003$ and the standard deviation in the measured strain field was $\sigma_{\varepsilon} = 0.0005$. The effect of GMB degradation on DVC accuracy was evaluated by correlating the reference tomogram to two independent tomograms acquired at 28% strain, and then comparing the difference between the two strain fields for each individual subset. In this state, 40% of the GMBs were damaged. We observed a maximum strain difference of $\Delta\varepsilon^{max} = .0028$ and standard deviation of $\sigma_{\varepsilon} = 0.0006$. Accordingly, all experimental conclusions were drawn from strain variation $\Delta\varepsilon \gg\ 0.01$, and DVC results are not reported for subsequent loading steps.

2.4. Finite element analysis

Inspection of the experimental tomograms and DVC results revealed that GMBs tended to cluster along oriented "chains" of closely-packed particles, and also that the proximity and orientation of neighboring GMBs affected the damage initiation and propagation behavior in the syntactic foam. Finite element (FE) analysis of a 2D model syntactic foam containing a chain of five adjacent GMBs was used to further explore this relationship. The analysis focused on the relevant scenarios for damage initiation and propagation by assessing the stress field while all GMBs were intact and the redistribution of stress after the central particle had collapsed. Collapse of the GMB was modeled by deleting its glass walls; this approach was consistent with the experiment, which showed that the GMB walls shattered after collapse and therefore eliminated their load-bearing capacity.

Five GMBs were arranged within a Sylgard 184 matrix that was subjected to uniaxial compressive deformation, as schematically illustrated in Fig. 3.2. The GMBs had a radius 30 μm and wall thickness of 2 μm, which were representative of the particles used in the experiment. The particle positions were defined with a center-to-center spacing (R) and orientation (θ), and were centrally located within a large, 1.5 mm square matrix to eliminate boundary effects. The model assumed a perfect interface between the GMBs and matrix using shared nodes; inspection of the experimental tomograms did not identify any delamination of any intact GMBs at low strain, although trace amounts of GMBs delaminated at higher strains. The top surface of the model was compressed axially by 210 μm in the negative Z direction (14% strain); this displacement was selected arbitrarily to be comparable to the first experimental load step with observed damage.

Two sets of analyses were performed: first, with all GMBs intact (State 1, Fig. 3.2a), and also after one was replaced with a void without a glass wall to simulate the collapsed GMB (State 2, Fig. 3.2b). For each state, the maximum principal stress on the GMBs was computed over a range of geometries with $70\ \mu m \leq R \leq 160\ \mu m$ and $0° \leq \theta \leq 90°$. The analyses excluded smaller separation distances to avoid meshing issues.

All calculations assumed linear-elastic, plane-strain material behavior ($E_{GMB} = 64\ GPa, \nu_{GMB} = 0.2, E_{matrix} = 2\ MPa, \nu_{matrix} = 0.48$); note that the small deformations justified a linear elastic model for the silicone matrix [15]. The mesh was refined near the GMBs to a size of 1 μm (two elements per wall thickness), while a coarser mesh was used further away (Fig. 3.2c). The model employed quadratic tetrahedral elements with ~13,000 elements and ~40,000 nodes, which accurately captured the stress gradient associated with flexure of the GMB walls under axial compression (Fig. 3.2d). A mesh sensitivity study showed convergence to within 0.5%. All calculations were performed in ANSYS R18.1.

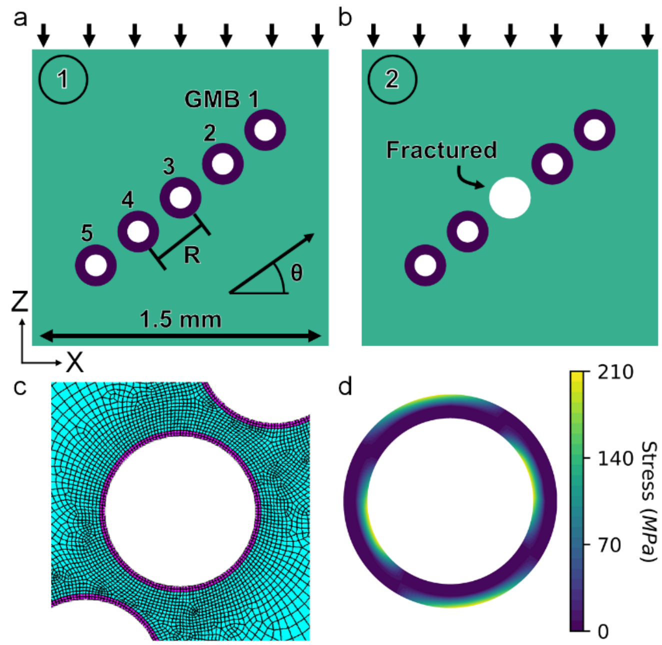

Fig. 3.2. FE model of GMB compression. (a-b) Five GMBs are embedded in a silicone matrix in (a) State 1 with five intact GMBs, and (b) State 2 with one GMB damaged. (c) Detail of FE mesh near GMBs. (d) Maximum principal stress on GMB 2 for $R = 70\ \mu m$, $\theta = 60°$. (a-b) not to scale, and wall thickness is exaggerated in (d).

3. Experimental results

To reveal the internal deformation mechanisms of the syntactic foam, central cross-sections from the *in situ* tomograms are presented in Fig. 3.3. Macroscopically, the specimen exhibited a minor barreling effect at increasing compression, but otherwise deformed uniformly with no bending or torsion (Fig. 3.3a). The visible porosity decreased substantially throughout the experiment as many GMBs collapsed. Detailed inspection of the low-resolution images (Fig. 3.3b) confirmed the damage to some GMBs, as the cross-sectional shape of pores transitioned from circular to elliptic; at the highest strains, many of the fractured GMBs had almost fully collapsed to thickness of a few voxels. However, the limited resolution of 10 μm per voxel prevented understanding of the GMB failure modes.

In contrast, the high-resolution tomograms did capture the detailed morphology of the damaged GMBs (Fig. 3.3c), allowing segmentation of the glass walls from the rubber matrix and identification of the specific damage mechanisms. The most common failure mode was fracture of the GMB walls, which created several glass fragments that were visible in the images (inset in Fig. 3.3c). The broken GMBs collapsed over several loading steps as the global compression increased, although the curvature of the GMB wall fragments prevented full closure of the cavity. A trace fraction of GMBs were observed to delaminate from the matrix at high strain.

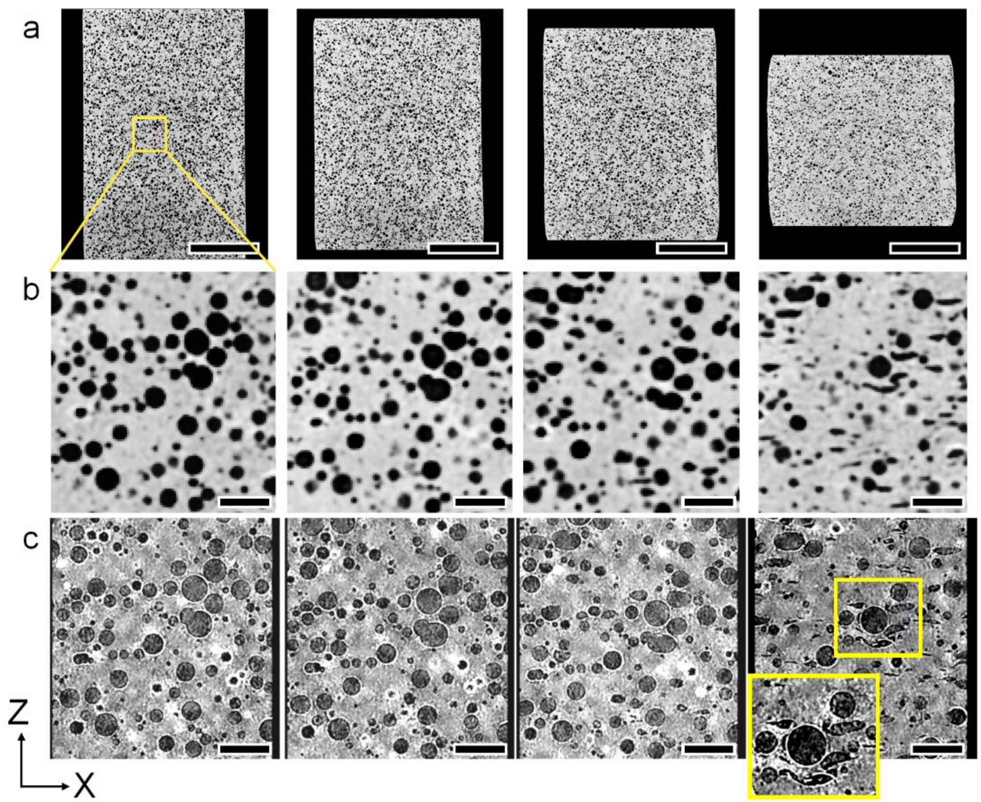

Fig. 3.3. Evidence of GMB collapse in *in situ* tomograms, acquired at $\varepsilon = -.07, -.14, -.21, -.35$ (left to right). (a) Central slices of low-resolution tomograms. (b) Magnified view of slices in (a). (c) Corresponding slices from high-resolution tomograms. Scale bars: (a) 2 mm, (b-c) 0.25 mm.

3.1. Mechanisms of GMB collapse and damage propagation

The tomograms clearly showed that GMB damage was not dispersed uniformly throughout the matrix, which is confirmed by 3D renderings of the GMBs in Fig. 3.4a. While the first damaged GMBs at $\varepsilon = -0.14$ (not shown) appeared to be isolated and somewhat randomly located, subsequent damage tended to spread from previously damaged GMBs. As a result, local pockets of collapsed GMBs were observed at $\varepsilon = -0.21$, but subsequent damage at larger strains through $\varepsilon = -0.35$ resulted in an almost fully-connected network of damaged GMBs. Inspection the damage at higher magnification in Fig. 3.4b confirmed this trend, and also highlighted an apparent correlation between GMB orientation and damage propagation. In particular, damage tended to spread transverse to the axial load (indicated by arrow). Thus, the pseudo-crush bands grew to span the entire high-resolution field of view.

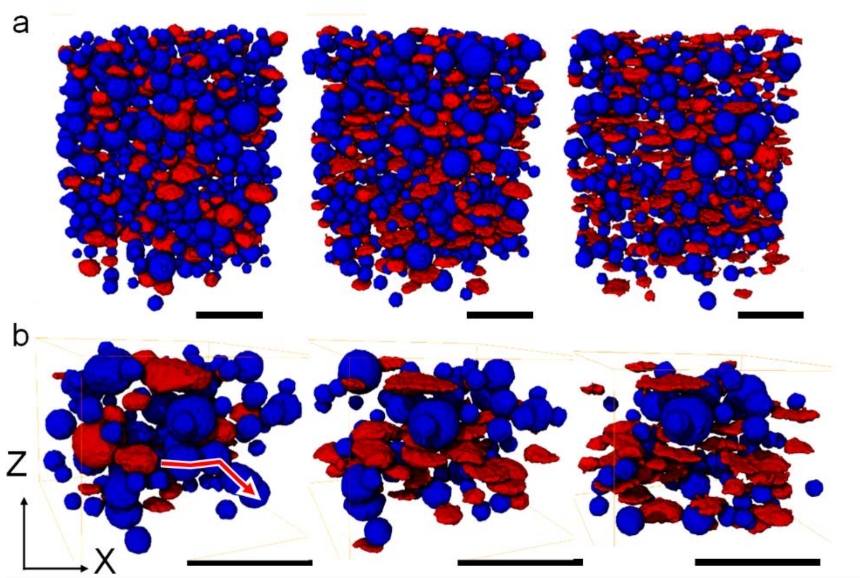

Fig. 3.4. High-resolution 3D renderings of collapsed GMBs. (a) Showing all intact GMBs in blue and damaged GMBs in red, and (b) detail of smaller field of view. Arrow in (b) shows path of damage propagation. Images acquired at $\varepsilon = -.21, -.28,$ and $-.35$ (left to right). Scale bar: 0.25 mm

This analysis raised two compelling questions regarding the damage mechanisms in the syntactic foam. First, what was the mechanism that causes the clustered damage? Second, was this pattern of heterogeneously distributed damage evident at longer length scales?

To further explore the mechanisms of damage initiation and propagation in the syntactic foam, a detailed inspection of the high-resolution tomograms was performed (Fig. 3.5). A cross-section of the reference tomogram clearly showed that the GMBs were not randomly distributed within the matrix but tended to align in chains of closely-packed GMBs (Fig. 3.5a). Interactions between the GMBs and load partitioning resulted in different damage patterns depending on the cluster orientation.

Two remarkable trends were observed regarding the effects of cluster orientation on local initiation and propagation of damage in the syntactic foam. This behavior was identified by tracking the motion of individual GMBs throughout the experiment in Fig. 3.5b-c, which highlights two representative chains with comparably sized GMBs. Comparable results were obtained for additional chains.

First, it is shown that the initiation of GMB collapse did not depend strongly on the chain orientation. In both the horizontal and vertical chains presented in Fig. 3.5b-c, the first collapsed GMBs were observed at a nominal strain of $\varepsilon = -0.14$. Mechanistically, this could indicate that the first instances of GMB failure were significantly regulated by nearest-neighbor interactions. For instance, it was speculated that a GMB with a particularly unfavorable combination of radii, wall thickness and contact with neighboring GMBs would fail first. In fact, all of the GMBs within Fig. 3.5b-c that had collapsed before $\varepsilon = -0.14$ demonstrated close proximity of less than 3 μm to neighboring GMBs.

However, damage propagated more rapidly in the chains that were aligned transverse to the axial load rather than aligned with the load. While GMBs in both chains began to collapse before a nominal axial strain of $\varepsilon = -0.14$, the damage propagated more rapidly in the transverse chain. In this case, all GMBs in the transverse chain collapsed by nominal strains of $\varepsilon = -0.28$, whereas only two of the four GMBs in the axial chain collapsed at the same load. Additional GMBs within Fig. 3.5c that were aligned axially above or below collapsed GMBs provided further examples of this orientation dependence.

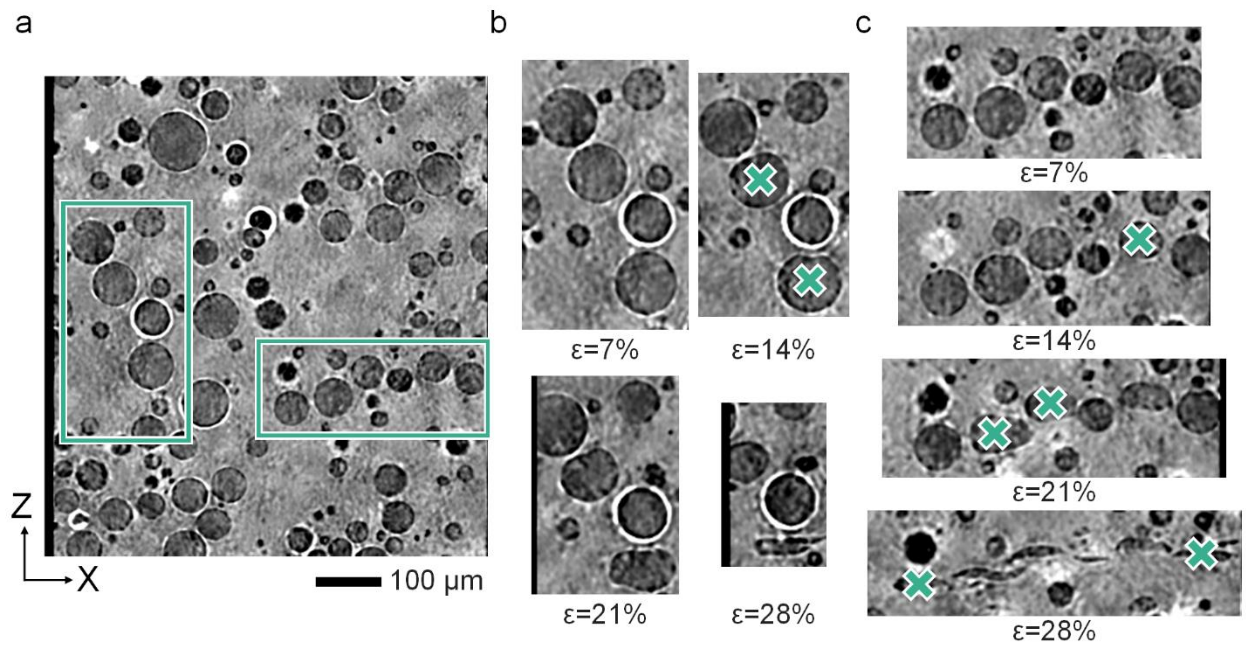

Fig. 3.5. Role of spatial arrangement on GMB collapse. (a) Central cross-section from high-resolution tomogram at zero load. (b-c) Sequence of collapse for (b) "axially arranged" and "laterally-arranged" clusters of GMBs. Nominal strains in (b-c) are indicated in figure, and the first sign of collapse in each GMB is marked by "×".

3.2. Measurements of long-range collapse using DVC

To evaluate damage propagation over larger length scales, the DVC strain measurements from the low-resolution, full-specimen tomograms are presented in Fig. 3.6. The axial strain field ε_{zz} showed largely uniform compression of the specimen away from the loaded surfaces on the specimen (Fig. 3.6a). The axial ε_{zz} revealed some strain variation in the composite, although the variation was hard to identify in comparison to the average strain. To more easily visualize the bands of crushed GMBs, the average global strain was subtracted from the local strain (Fig. 3.6b), resulting in a background-removed axial strain $\hat{\varepsilon}_{zz}(x, y, z) = \varepsilon_{zz}(x, y, z) - \bar{\varepsilon}_{zz}$. In this way, negative values of $\hat{\varepsilon}_{zz}$ indicated locally extreme compression due to GMB collapse. This is justified since damaged GMBs greatly reduced the local stiffness of the material, so regions of locally high compressive axial ε_{zz} were used to indirectly indicate GMB collapse.

In the background-removed strain fields, prominent strain bands exhibited strong preferential orientation that was consistent with previous results in Fig. 3.4b. At a nominal strain of $\varepsilon = -0.14$, these bands were initially small and isolated with widths less than 0.25 mm and typical $\hat{\varepsilon}_{zz} \approx -.01$, but continued to grow across the specimen and connect at increasing deformation. By $\varepsilon = -0.28$, the bands had grown in prominence to typical $\hat{\varepsilon}_{zz} \approx -.05$, and some were as long as 6 mm. At $\varepsilon = -0.28$, the average axial spacing between failure bands was ~500 μm (about 8 times the average GMB diameter of 60 μm). Compression bands were more prominent away from the free surface of the specimen, suggesting that constraint has some effects on GMB collapse.

To confirm that the bands of compressive $\hat{\varepsilon}_{zz}$ corresponded to damaged GMBs, the measured strain field was superimposed on the underlying tomograms (Fig. 3.6c). These regions approximately corresponded to the high-magnification images presented in Fig. 3.3c to allow comparison to the high-resolution tomograms. Strong correspondence between the regions of high compressive $\hat{\varepsilon}_{zz}$ and bands of collapsed GMBs suggested that the DVC results successfully identified the initiation of damage in the syntactic foam. Regions of faint compressive $\hat{\varepsilon}_{zz} \approx -0.01$ appeared at the onset of GMB damage (visible as slight changes in sphericity), and grew in prominence as the GMBs fully collapsed. These bands appeared to be separated by small clusters of intact GMBs that were protected by other collapsed GMBs.

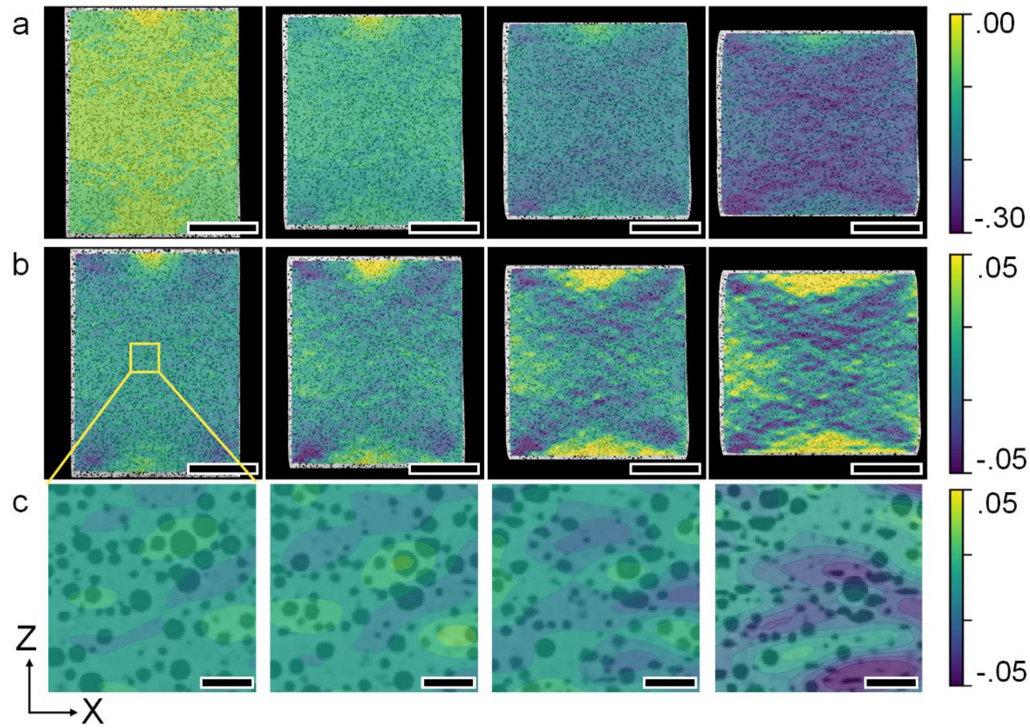

Fig. 3.6. DVC results for tomograms acquired at $\varepsilon = -0.07, -0.14, -0.21, -0.28$ (left to right). (a) axial strain ε_{zz}, (b) background-removed $\bar{\varepsilon}_{zz}$, (c) magnified view of central region in (b). Scale bars: (a-b) 2 mm, (c) 0.25 mm.

4. *Finite element results*

In agreement with the experimental results, the stress state was found to strongly depend on the spacing and orientation of neighboring GMBs. Under the premise that the collapse of brittle GMBs could accurately be predicted by the maximum principal stress, the peak stress within the GMB 2 (which is adjacent to the central GMB, refer to Fig. 3.2a) is shown as a function of GMB arrangement in Fig. 3.7. Results are presented for both State 1 with all GMBs intact (Fig. 3.7a), for State 2 after one GMB was damaged (Fig. 3.7b), and also the change in maximum principal stress between these two states due to stress redistribution (Fig. 3.7c).

With all GMBs intact (State 1), the maximum stress was experienced when the GMBs were closely spaced and axially aligned ($R = 70\ \mu m, \theta = 90°$), resulting in a peak stress of 418 MPa. The stress was elevated to a lesser extent when the GMBs were aligned transverse to the axial load ($R = 70$ μ$m, \theta = 0°$), with a maximum stress of 349 MPa. Interestingly, the peak stress was diminished at small R for intermediate orientations near $\theta = 45°$, with a minimum peak stress of 150 MPa. For all orientations, the significance of GMB orientation decreased at large R, resulting in smaller variation in stress as a function of θ: effectively, isolated GMBs experienced much lower stress.

Critically, the effects of neighboring GMB arrangement changed substantially after one of the GMBs had collapsed (State 2). The highest stresses in GMB 2 were observed with small angles $\theta \approx 15°$ and small R ($\sigma_{max} = 241\ MPa$), while the smallest peak stresses were observed for $\theta \approx 70°$ and small R ($\sigma_{max} = 182\ MPa$). Stresses for closely packed GMBs at $\theta = 0°$ became higher than those at $\theta = 90°$, though the peak GMB stresses at these two arrangements were lower than before collapse. These changes are succinctly highlighted in the stress redistribution map in Fig. 3.7c, which clearly showed that the collapse of a neighboring GMB intensified the peak stress for $35° \leq \theta \leq 55°$, minorly alleviated stress for $\theta < 35°$, and majorly reduced the stress for $\theta > 55°$.

Together, these analyses have important implications for the initiation and propagation of GMB collapse in syntactic foams. First, chains of closely-packed, intact GMBs with orientations near 0° or 90° can greatly amplify the peak tensile stress observed in the GMB walls, thereby promoting damage initiation for these GMB arrangements. After one particle in the chain collapses, however, stress redistribution strongly alters the favorability of subsequent GMB collapse. Stress becomes highest in chains of GMBs oriented near 0°. Accordingly, while damage initiation is most probable in either the 0° or 90° configurations, damage propagation from a collapsed GMB is most likely in the 0° chain. Moreover, small deviations in the positions of GMBs in a nominally horizontal chain (e.g., such that the orientation is closer to 10° than 0°)

could further accelerate damage propagation.

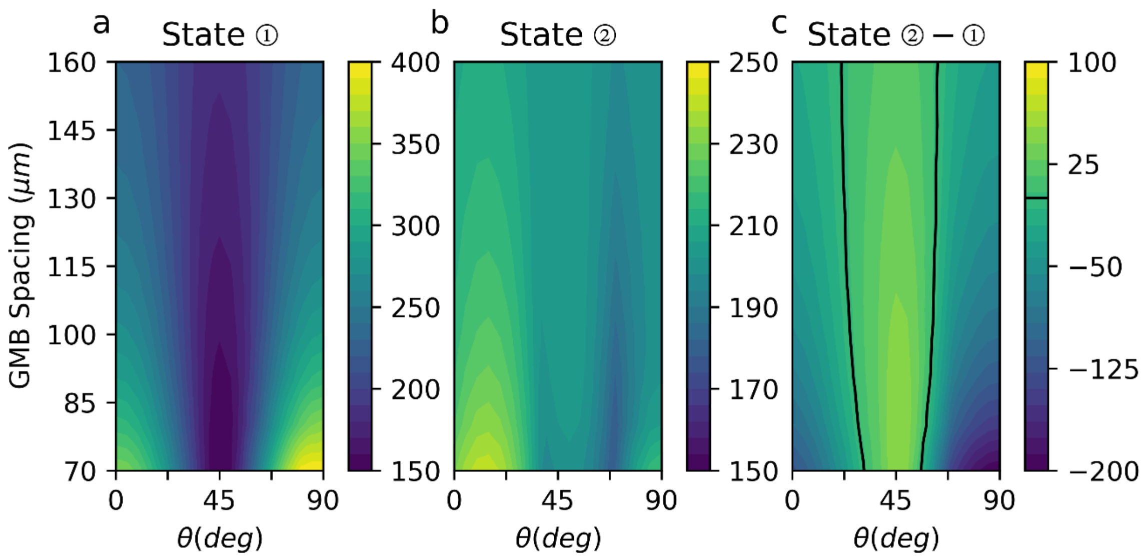

Fig. 3.7. Finite element calculations of maximum principal stress in GMB 2 as a function of GMB arrangement for (a) state 1, (b) state 2, and (c) the difference between state 1 and 2. Results are computed for nominal axial strain of $\varepsilon_o = -0.14$.

5. Discussion

5.1. Mechanisms of damage initiation and propagation in syntactic foams

The primary experimental finding was that the arrangement of neighboring GMBs mechanistically affected the initiation and propagation of damage in syntactic foams, ultimately leading to the formation of elongated bands of collapsed GMBs in the syntactic foam composite.

Damage initiation depended strongly on both the orientation and distance of nearest-neighbor GMB (in addition to the GMB radius and wall thickness). This was shown experimentally, where the earliest GMB collapse occurred when the spacing between GMBs was small and the particles were oriented near $\theta = 0°$ (transverse to axial load) or 90° (aligned with axial load); complementary FE calculations indicated that stress was comparably elevated in both of these configurations. For intermediate angles, FE calculations showed that the neighboring particles actually reduced the stress experienced by each GMB, thereby inhibiting collapse. Since the random packing of GMBs within the syntactic foam produced a variety of inter-particle spacings and orientations, damage initiated somewhat randomly at different loads throughout the composite. Damage was particularly common in chains of axially- or transversely-aligned GMBs with small spacing between neighboring particles, and less common among isolated GMBs.

However, a very different orientation dependence was observed once some of the GMBs collapsed. This was explained in terms of "stress shielding" for axially aligned particles and "stress intensifying" behavior for transversely aligned particles (Fig. 3.8). After the initial collapse of a GMB, the load must be redistributed away from the damaged particle. When the neighboring particles were aligned axially, the collapsed particle shielded the intact GMB from large stresses (Fig. 3.8a) due to shear lag effects. In an alternate scenario, when neighboring GMBs were aligned transverse the load (Fig. 3.8b), the collapse of one GMB redistributed stress toward the adjacent GMB, thereby promoting damage propagation.

This stress redistribution mechanism resulted in considerable asymmetry in the damage propagation, such that damage spread more rapidly along transversely-oriented chains of GMBs with $\theta \approx 0°$ compared to the axial GMB chains with $\theta \approx 90°$. These proposed mechanisms were also supported by FE calculations (Fig. 3.7b), which showed that GMB collapse dramatically reduced the stress on the neighboring GMB when $\theta \approx 90°$, and only moderately when $\theta \approx 0°$. Thus, stress redistribution facilitated the spread of GMB collapse transverse to the axial load.

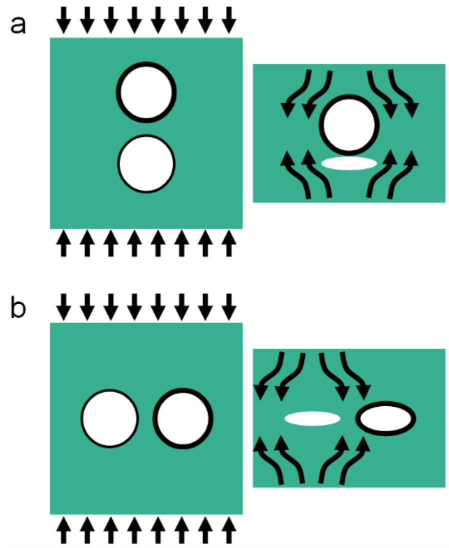

Fig. 3.8. Mechanisms of propagating GMB collapse. (a) Shielding effect from axially-arranged GMBs. (b) Stress-intensifying effect due to laterally-arranged GMBs.

5.2. Long-range damage propagation in syntactic foams

While the high-resolution tomograms adequately explained the local damage trends, their restricted field of view made it challenging to track the damage behavior at longer length scales. In contrast, quantitative deformation measurements of the low-resolution tomograms using DVC identified damage throughout the entire specimen volume. Interpretation of the DVC-measured strain fields revealed the formation of local pseudo-crush bands beginning at low loads, which subsequently propagated transversely across the specimen and merged with neighboring bands. This was mechanistically associated with the clustering of GMBs within the foam and the previously discussed damage mechanisms. Ultimately, this resulted in characteristic pseudo-crush bands with thicknesses of ~500 μm in the axial direction, and lengths that grew to several millimeters in the transverse direction. Individual bands appeared to be separated by resilient GMBs that were shielded from elevated stresses.

The identification of banded damage contradicts recent findings of nominally homogeneous and dispersed failure [11]. This discrepancy emphasized the importance of quantitative damage measurements in accurately interpreting the damage mechanisms of syntactic foams, particularly at length scales larger than permitted by high-resolution tomography. DVC uniquely allowed quantitative 3D analysis of syntactic foam deformation over several millimeters, whereas previous quantitative studies have been restricted to smaller fields of view. It remains unclear how the GMB volume fraction affects the damage propagation mechanism in these materials, since the FE calculations suggest that sparse or tightly-packed GMBs could alter the inter-particle interactions.

6. Conclusions

Quantitative analysis of *in situ* XCT compression experiments on elastomeric syntactic foams has unveiled the fundamental role of inter-particle arrangement on the damage initiation and propagation mechanisms. Both quantitative analysis of high-resolution tomograms and complementary finite element analyses showed that the propensity of GMBs to collapse (1) increased with decreasing spacing between particles, and (2) depended nonlinearly on the orientation of the nearest-neighbor particles. The nonlinear relationship between neighbor orientation and maximum stress promoted collapse in GMBs with neighboring particles oriented at 0° or 90° to the applied load, and inhibited collapse at intermediate angles. Interestingly, the stress redistribution after one GMB collapsed led to a preferred direction of damage propagation transverse to the applied load. Quantitative deformation analysis using digital volume correlation confirmed this trend by identifying prominent pseudo-crush bands with thicknesses of $500\ \mu m$ and widths of several millimeters; this damage mode relied on a uniform compressive stress state in the sample interior, and may be sensitive to the specimen geometry or size. This damage behavior was caused by stress redistribution and shielding around collapsed GMBs, which depended strongly on the orientation of neighboring particle and promoted damage propagation in the transverse direction.

References

[1] N. Gupta, Kishore, E. Woldesenbet, S. Sankaran, Studies on compressive failure features in syntactic foam material, J. Mater. Sci. 36 (2001) 4485–4491. doi:10.1023/A:1017986820603.

[2] M. Yu, P. Zhu, Y. Ma, Identification of the interface properties of hollow spheres filled syntactic foams: An inverse strategy combining microstructural modeling with Kriging metamodel, Compos. Sci. Technol. 74 (2013) 179–185. doi:10.1016/j.compscitech.2012.11.002.

[3] N. Gupta, A functionally graded syntactic foam material for high energy absorption under compression, Mater. Lett. 61 (2007) 979–982. doi:10.1016/j.matlet.2006.06.033.

[4] M. Porfiri, N. Gupta, Effect of volume fraction and wall thickness on the elastic properties of hollow particle filled composites, Compos. Part B Eng. 40 (2009) 166–173. doi:10.1016/j.compositesb.2008.09.002.

[5] G. Tagliavia, M. Porfiri, N. Gupta, Analysis of particle-to-particle elastic interactions in syntactic foams, Mech. Mater. 43 (2011) 952–968. doi:10.1016/j.mechmat.2011.08.008.

[6] M. Yu, P. Zhu, Y. Ma, Effects of particle clustering on the tensile properties and failure mechanisms of hollow spheres filled syntactic foams: A numerical investigation by microstructure based modeling, Mater. Des. 47 (2013) 80–89. doi:10.1016/j.matdes.2012.12.004.

[7] J. Adrien, E. Maire, N. Gimenez, V. Sauvant-Moynot, Experimental study of the compression behaviour of syntactic foams by in situ X-ray tomography, Acta Mater. 55 (2007) 1667–1679. doi:10.1016/j.actamat.2006.10.027.

[8] J. Lachambre, E. Maire, J. Adrien, D. Choqueuse, In situ observation of syntactic foams under hydrostatic pressure using X-ray tomography, Acta Mater. 61 (2013) 4035–4043. doi:10.1016/j.actamat.2013.03.017.

[9] R. Huang, P. Li, T. Liu, X-ray microtomography and finite element modelling of compressive failure mechanism in cenosphere epoxy syntactic foams, Compos. Struct. 140 (2016) 157–165. doi:10.1016/j.compstruct.2015.12.040.

[10] L. Bardella, F. Malanca, P. Ponzo, A. Panteghini, M. Porfiri, A micromechanical model for quasi-brittle compressive failure of glass-microballoons/thermoset-matrix syntactic foams, J. Eur. Ceram. Soc. 34 (2014) 2605–2616. doi:10.1016/j.jeurceramsoc.2013.11.045.

[11] B.M. Patterson, N.L. Cordes, K. Henderson, J.J. Williams, T. Stannard, S.S. Singh, A.R. Ovejero, X. Xiao, M. Robinson, N. Chawla, In situ X-ray synchrotron tomographic imaging during the compression of hyper-elastic polymeric materials, J. Mater. Sci. 51 (2016) 171–187. doi:10.1007/s10853-015-9355-8.

[12] M.A. Sutton, J.-J. Orteu, H.W. Schreier, Image Correlation for Shape, Motion and Deformation Measurements, Springer US, Boston, MA, 2009. doi:10.1007/978-0-387-78747-3.

[13] B.P. Croom, W.-M. Wang, J. Li, X. Li, Unveiling 3D Deformations in Polymer Composites by Coupled Micro X-Ray Computed Tomography and Volumetric Digital Image Correlation, Exp. Mech. 56 (2016) 999–1016. doi:10.1007/s11340-016-0140-7.

[14] B.P. Croom, P. Xu, E.J. Lahoda, C.P. Deck, X. Li, Quantifying the three-dimensional damage and stress redistribution mechanisms of braided SiC/SiC composites by in situ volumetric digital image correlation, Scr. Mater. 130 (2017) 238–241. doi:10.1016/j.scriptamat.2016.12.021.

[15] I.D. Johnston, D.K. McCluskey, C.K.L. Tan, M.C. Tracey, Mechanical characterization of bulk Sylgard 184 for microfluidics and microengineering, J. Micromechanics Microengineering. 24 (2014) 035017. doi:10.1088/0960-1317/24/3/035017.

Chapter 4:
Particle clustering effects on damage in elastomeric syntactic foams

1. Introduction

Syntactic foam composites use hollow glass microballoons (GMBs) to reinforce a polymer matrix. Since the fragile GMBs collapse under mechanical load, the syntactic foam exhibits a unique response to uniaxial compression that is characterized by an initially stiff elastic response, a plateau during which many GMBs collapse at approximately uniform load, and subsequent densification after most GMBs have collapsed. By nature of the GMB's low density and their associated damage mechanisms, syntactic foams exhibit exceptional specific stiffness and energy absorption [1–5], which has motivated their use in many aerospace, marine and sporting goods applications. Of particular interest is a new class of syntactic foams with elastomer matrices [6–8], which exhibits very different mechanical behavior compared to more widely studied foams with glassy thermoset or thermoplastic matrices. Specifically, the very soft elastomer matrix deforms elastically until very large strains, and does not localize or fracture in a brittle manner. It remains unclear how these properties affect the damage mechanisms.

Moreover, the role of GMB volume fraction ϕ on the damage behavior of syntactic foams is poorly understood at a micro-mechanics level, particularly for elastomer-matrix foams. While macroscopic, surface-based measurements of epoxy-matrix syntactic foams have identified a transition in failure mode from axial splitting at $\phi \leq 0.2$ to shear-dominated cracking at $\phi \geq 0.3$ [9], the damage behavior that precedes failure remains unclear. To the author's knowledge, the early stages of GMB collapse as a function of ϕ have not been studied experimentally.

Some progress has been made experimentally using *in situ* X-ray Computed Tomography (XCT) experiments to capture the 3D arrangement of GMBs and their collapse [6,10–12]. For instance, softer polymer matrices such as polypropylene ($\phi = 0.49$) and elastomer matrices such as polyurethane ($\phi = 0.43$) promoted dispersed GMB collapse, whereas stiff and brittle epoxy matrices ($\phi = 0.55$) led to localized damage along well-defined shear planes [10]. However, these conclusions were confounded by the different ϕ in each foam. With lower ϕ, the large average spacing between GMBs could hypothetically enable redistribution of stress away from damaged GMBs and prevent damage localization.

In fact, the trends observed by Adrien [10] contrast with results from recent *in situ* XCT compression experiments on a syntactic foam featuring an elastomeric silicone (PDMS) matrix with $\phi = 0.37$, which showed clustered damage along "pseudo crush bands" [7]. Damage tended to occur in closely-packed chains of GMBs, which was verified numerically to magnify the peak stress experienced by each particle and was not previously reported in *in situ* XCT experiments. In this sense, the localized damage resembled the behavior observed in other foams with higher ϕ and stiffer matrices. Due to the different mechanical response of PDMS compared to both epoxy and polyurethane, these results imply that volume fraction or matrix stiffness cannot fully explain the damage mechanisms. Rather, GMB failure localization appears to be a competition between the *local packing of adjacent GMBs*, which amplifies the GMB stresses, and the *ability of the matrix to redistribute stress* away from highly-loaded or damaged GMBs.

This relationship has been preliminarily explored using finite element (FE) modeling techniques with different ϕ [8,9,12,13]. Notably, Yu *et al.* [14] investigated the effects of particle clustering in epoxy-matrix foams, revealing that increased clustering of GMBs resulted in damage at smaller strains. The important distinction between the *global volume fraction* and the *local interparticle spacing* helps explain the *in situ* XCT results reported in [7]. However, these models explored foams with brittle matrices at small deformations, and also enforced a *minimum spacing* between particles to preserve the quality of the FE mesh. In actual elastomeric syntactic foams, the matrix is very compliant and spacing between adjacent GMBs may be very small.

The objective of this work is to quantitatively unveil the role of interparticle spacing on the observed damage behavior in syntactic foams with elastomeric matrices. In particular, how does the spatial distribution of damage vary with volume fraction, and what is the mechanism for these trends? This is achieved with a new quantitative *in situ* XCT experiment framework that enables tracking of individual GMBs throughout compression. From this analysis, the damage of each GMB can be related to the local arrangement of neighboring particles.

2. Experimental methods

2.1. Materials

Syntactic foam specimens were prepared for *in situ* XCT compression experiments using techniques previously described in Chapter 3 [7]. In brief, the syntactic foams were formed by mixing A16 GMBs (3M) into a two-part Sylgard 184 elastomer matrix (Dow Corning) with a curing agent. The slurry was drawn into cylindrical syringe molds, cured at room temperature, and subsequently cut into specimens with 7 mm height and 4.8 mm diameter. The diameter of A16 GMBs ranged from 30 to 95 μm within 10-90% distribution, with a mean diameter of 60 μm. Four foam specimens were prepared with nominal volume fractions of $\phi = 0.10, 0.20, 0.37$ and 0.46 (Fig. 4.1). Due to the differences in volume fractions and local clustering, each specimen produced very different interactions between GMBs. It is noted that results from the same $\phi = 0.37$ specimen were partially reported in in Chapter 3 [7].

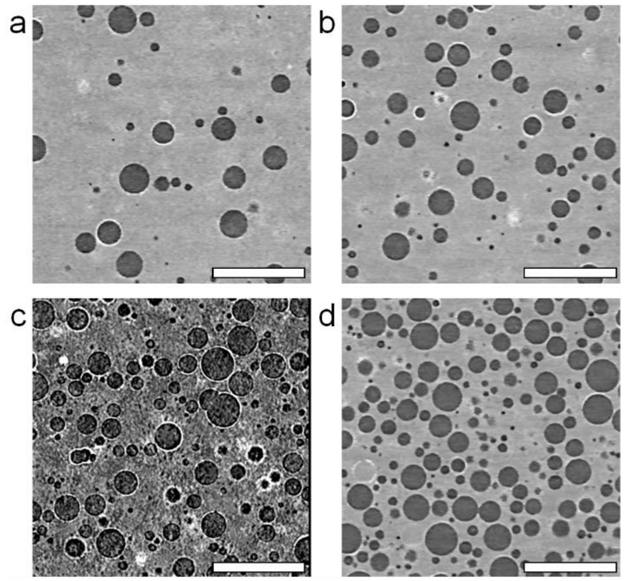

Fig. 4.1. GMB arrangement in syntactic foams with different volume fractions. Shown are XCT cross-sections with $\phi = 0.10$, (b) $\phi = 0.20$, (c) $\phi = 0.37$, and (d) $\phi = 0.46$. GMBs are marked by the dark voids, while the matrix is light gray. Scale bar: 250 μm.

2.2. In situ XCT compression

Using a custom XCT loading stage previously described in Chapter 1 [15], the specimens were compressed *in situ* within an Xradia microXCT-200 machine. Tomography was performed at two resolutions prior to testing and at each load step. First, high-resolution images with voxel size of 1.7 μm and size $[1000\ \text{voxels}]^3$ captured the internal microstructure of the syntactic foam and revealed damage to individual GMBs, though the specimen with $\phi = 0.37$ was imaged with an image size of $[500\ \text{voxels}]^3$ at the same voxel resolution. Additionally, low-resolution images with voxel size of 8.5 μm and size $[1000\ \text{voxels}]^3$ were used to compute deformation across the entire specimen using Digital Volume Correlation (DVC). Specimens were deformed in 500 μm increments between images. All imaging was performed using X-ray source energy of 80 keV and power of 8 W. The nominal engineering stress-strain curve for each specimen is shown in Fig. 4.2a, which shows the development of a prominent stress "plateau" at increasing volume fraction.

The multi-scale imaging approach enables a unique data analysis framework that can track the damage of individual GMBs. First, analysis of the low-resolution tomograms using DVC provides full-field displacement measurements with sub-voxel accuracy (described in Section 2.3). Next, reference features in the high-resolution tomograms are registered in the corresponding low-resolution images. In this way, the DVC displacement field can be aligned and scaled to measure the deformation in the high-resolution tomograms. Third, standard image processing approaches are used to detect damage in individual GMBs in the high-resolution tomograms at each deformed state (Section 2.4). Finally, the GMBs are tracked through each *in situ* high-resolution tomogram using the scaled DVC displacement field (Section 2.5), which can be used to relate the GMB damage to the initial arrangement of particles.

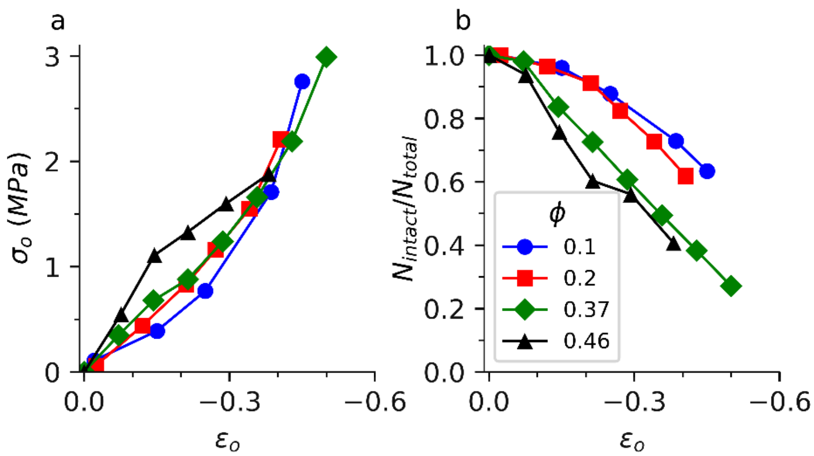

Fig. 4.2. Mechanical response of syntactic foam specimens. (a) Engineering stress-strain curves, and (b) fraction of intact GMBs vs. engineering strain.

2.3. Digital volume correlation

Quantitative kinematic analysis of the low-resolution tomograms using Digital Volume Correlation (DVC) provides a reliable measurement of damage mechanisms in the syntactic foam across the entire specimen. As discussed in Chapter 3 [7], locally elevated compression can indicate localized damage in the syntactic foam. Conceptually, this is related to the collapse of GMBs within the analysis subvolume, which reduces the local stiffness. In this sense, DVC analysis complements the direct quantitative analysis of the high-resolution tomograms by confirming the GMB damage behavior over larger length scales.

Correlation of the low-resolution tomograms was performed using commercial DVC software (Vic-Volume, Correlation Solution Inc.) according to the framework established in Chapter 1. Analysis was performed with subset size [29 voxels]^3, step size 3 voxels, and strain filter size of [5 subsets]^3. This resulted in an effective virtual strain gage size of [350 μm]^3. While damage to GMBs can introduce decorrelation effects and reduce the accuracy of the DVC analysis, this behavior has been extensively characterized in Chapter 2 [16] and the standard deviation of strain error is shown to remain below $\sigma\varepsilon = 0.001$ beneath a strain level of $\varepsilon^{crit} \approx -0.30$ depending on the GMB volume fraction. DVC analysis in this paper is restricted to below ε^{crit}.

2.4. Damage analysis

Post-processing of the high-resolution tomograms using custom scripts developed in Python and Avizo Fire 9.0 were used to de-noise, threshold, segment and measure the individual GMBs throughout the experiment. The 3D Feret Shape (FS) of each GMB was used to interpret the damage status of the particles, which is analogous to a 3D aspect ratio. Particles with $FS > 1.3$ were classified as collapsed. We note that the accuracy of the FS measurement depends on the accuracy of the segmentation process and GMB size, but one could reasonably expect accuracy of ~10% for the smallest diameter particles [17]. The fraction of collapsed GMBs for each specimen is presented as a function of deformation in Fig. 4.2b.

2.5. GMB tracking scheme

To provide more detailed analysis on the mechanics of GMB collapse, the segmented GMBs were tracked between subsequent loading steps; this allowed comparison of GMB survival with its initial location in the foam. After scaling the DVC results to the high-resolution tomograms with a magnification factor, a matching scheme was implemented that used the DVC displacements to predict the location of each particle in the next high-resolution tomogram. Due to heterogeneous deformation within each DVC subset, measurement noise, and the difference in magnification between the low-resolution DVC measurements and the high-resolution tomograms, the predicted GMB location was often off by a few pixels; this error increased with deformation. To reliably match GMBs between load steps, we adopted a "greedy" algorithm: the particle with the smallest discrepancy between the predicted and deformed locations was removed from the search queue, and this process was repeated until the discrepancy between all remaining particle locations exceeded a critical distance of 5 voxels. Thus, poorly-matched GMBs were excluded from subsequent analysis.

3. Experimental results

To elucidate the effects of local GMB packing on the damage mechanisms, analysis of GMB collapse was performed on the *in situ* tomograms at multiple length scales. Inspection of the high-resolution tomograms revealed the specific damage mechanisms, while DVC analysis of the low-resolution tomograms confirmed these behaviors across the entire specimen.

3.1. Damage mechanisms

Detailed analysis of the high-resolution tomograms revealed unique damage mechanisms for the foams with different ϕ (Fig. 4.3). In particular, the damage behavior appeared to strongly correlate with the local clustering of GMBs.

For the low volume fraction sample ($\phi = 0.10$), GMB damage was dispersed and initiated only at high strains (Fig. 4.3a). Most of the GMBs were isolated, and the images revealed few “chains” of closely packed GMBs. Consistent with previous results [7], the images revealed that that damage occurred more rapidly in these chains than in isolated GMBs. Even at large strains, most of the particles remained intact.

Similar trends were observed at $\phi = 0.20$ (Fig. 4.3b). In this sample, damage tended to initiate earliest in GMBs with closely-spaced neighbors rather than isolated particles. The tomograms first identified GMB collapse at lower strains compared to $\phi = 0.07$, possibly due to higher stresses associated with the stiffer composite. As in the $\phi = 0.07$ specimen, GMB collapse remained incomplete, and all damaged GMBs still had intact neighbors at $\varepsilon = -0.28$.

At higher volume fractions, GMB collapse initiated at lower strains, damage occurred more rapidly, and a larger fraction of GMBs collapsed compared to the low ϕ specimens. Additionally, the damage behavior exhibited some degree of localization, as the damage appeared to spread to proximate GMBs. For $\phi = 0.37$ (Fig. 4.3c), isolated damage appeared by $\varepsilon = -0.14$, and soon propagated to adjacent GMBs. Damage diffused more rapidly through horizontal chains of GMBs due to stress intensifying effects from the GMB orientation [7], resulting in several transverse “pseudo crush bands” across the field of view.

Finally, for $\phi = 0.46$ (Fig. 4.3d), damage was first identified at $\varepsilon = -0.07$. Damage quickly propagated to adjacent GMBs, producing a large cluster of collapsed GMBs by $\varepsilon = -0.14$. By $\varepsilon = -0.28$, nearly all GMBs within the field of view were damaged. At this volume fraction, nearly all GMBs had multiple neighboring particles in close proximity, which allowed damage to spread efficiently.

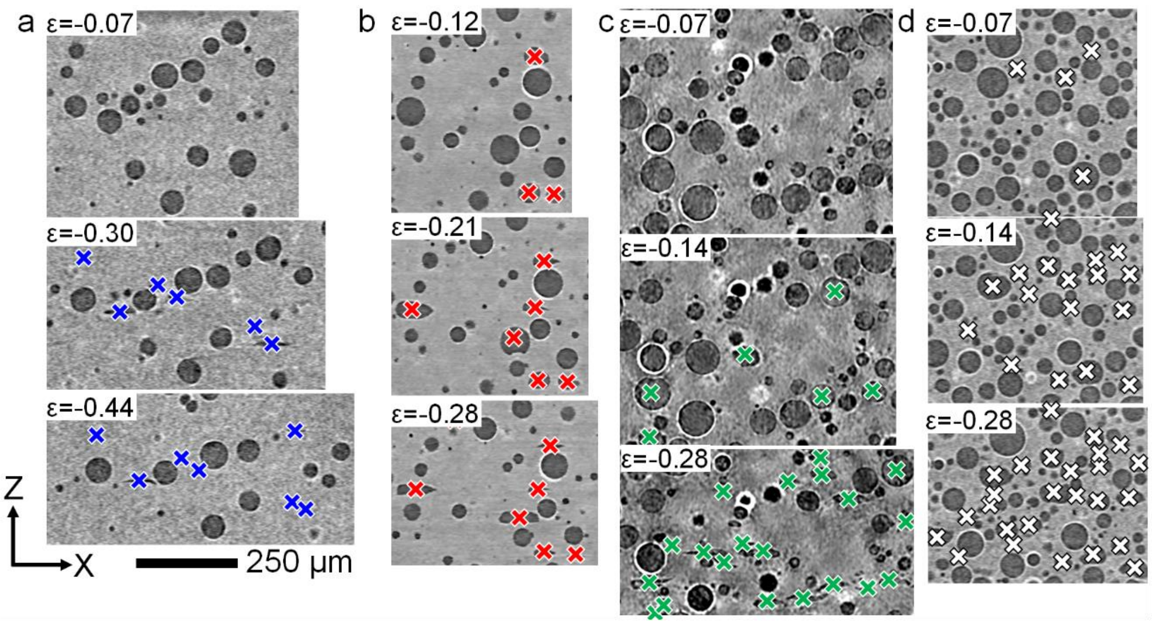

Fig. 4.3. Comparison of strain-dependent damage in syntactic foams with different volume fractions. Volume fractions are (a) $\phi = 0.10$, (b) $\phi = 0.20$, (c) $\phi = 0.37$ and (d) $\phi = 0.46$. Damaged GMBs are marked with "×".

3.2. DVC results

To better visualize the spatial patterns of GMB collapse for the different volume fractions, the DVC-measured axial strain fields at strains $\varepsilon_{zz} \approx -0.30$ are presented in Fig. 4.4. As visible in Fig. 4.4a, the axial strain ε_{zz} exhibited increasing variation with larger GMB volume fraction, despite the average strain being comparable. To more clearly the emphasize the strain variation, the background-removed axial strain is presented in Fig. 4.4b [7],

$$\hat{\varepsilon}_{zz}(x, y, z) = \varepsilon_{zz}(x, y, z) - \bar{\varepsilon}_{zz} \tag{4.1}$$

where $\bar{\varepsilon}_{zz}$ is the average axial strain.

From these results, it is clear that the strain variation increased in magnitude from $\Delta\hat{\varepsilon}_{zz} \approx 0.01$ for the lowest volume fraction $\phi = 0.10$ to $\Delta\hat{\varepsilon}_{zz} \approx 0.05$ for the highest volume fraction $\phi = 0.46$. Moreover, the spatial distribution of strain variation also changed with volume fraction. At larger ϕ, the size of regions with compressive $\hat{\varepsilon}_{zz}$ grew, indicating large clusters of collapsed GMBs. Detailed inspection of these regions in Fig. 4.4c further supported this claim, with negative $\hat{\varepsilon}_{zz}$ neatly superimposed on non-spherical (collapsed) GMBs. These results closely matched the analysis of high-resolution tomograms, where isolated and dispersed GMB collapse would result in smaller strain variation, and more localized collapse would result in stronger variation with lower spatial frequency.

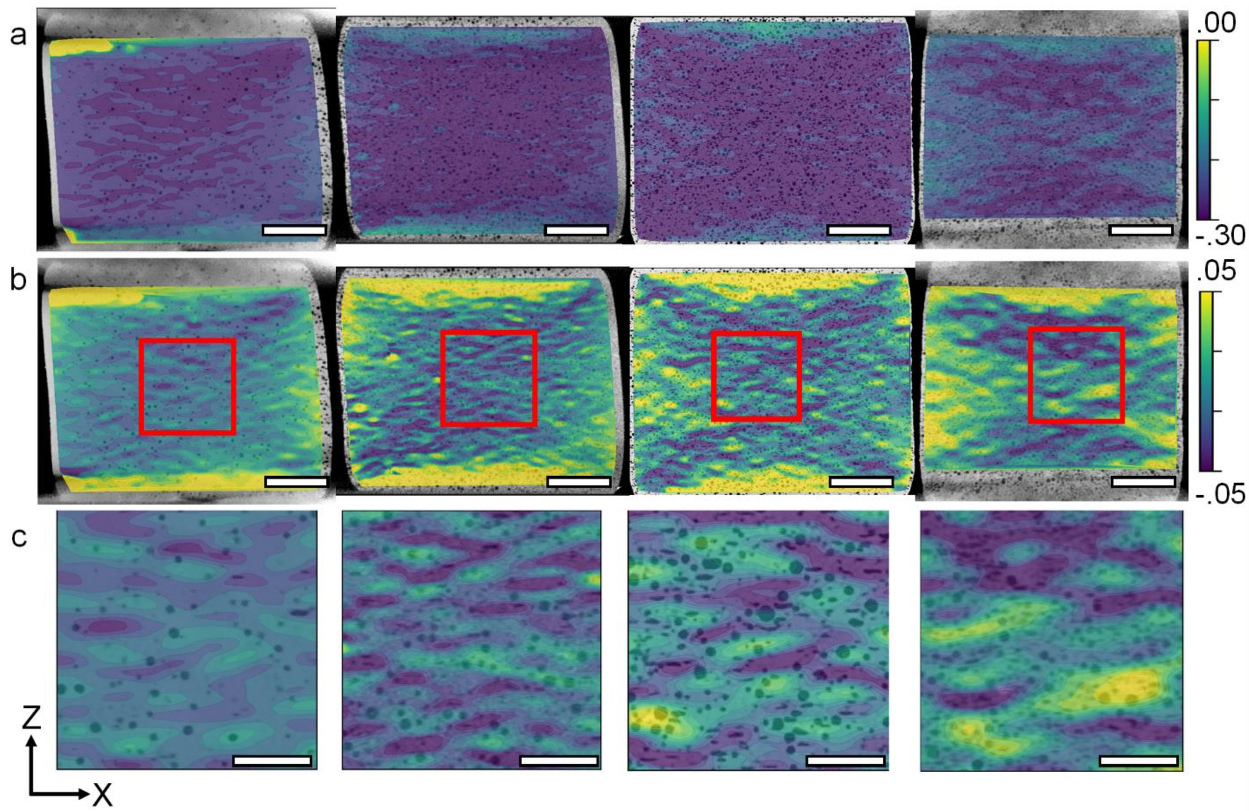

Fig. 4.4. DVC axial strain fields for syntactic foams with different volume fractions. (a) Axial strain ε_{zz} at a nominal strain of $\varepsilon_{zz} = -0.30$, (b) background-removed axial strain $\hat{\varepsilon}_{zz}$, and (c) detail of (b). Red squares in (b) indicate location of (c). Volume fractions, from left to right: $\phi = 0.10, 0.20, 0.37, 0.46$. Scale bars: (a-b) 2 mm, (c) 500 µm.

4. Statistical analysis of GMB collapse

The random arrangement of GMBs within each specimen provided a convenient way to test the effects local GMB clustering on the survival of particles as the syntactic foam was compressed. In this section, the local clustering of GMBs is quantified by the local coordination number $N_{neighbor}$, defined as the number of adjacent particles located within one average diameter ($d_{avg} = 60\ \mu m$) from each GMB center. As shown in Fig. 4.5, this statistic varied substantially within specimens due to local clustering effects, and also between specimens due to the different ϕ. At low ϕ, many particles were isolated with none or few proximate neighbors. In contrast, all GMBs in the $\phi = 0.46$ specimen had nearby neighbors, and the most densely-packed region of the specimen contained up to 14 adjacent GMBs per particle.

Based on previous analyses of particle interactions [7], the more-densely packed GMBs should collapse earlier. This was confirmed with the results highlighted in Fig. 4.6, which summarizes the probability of GMB survival ($p_{survival}$) at increasing deformation for the different syntactic foams. Using the particle tracking scheme described in Section 2.5, each GMB in the deformed state was mapped back to its initial configuration to determine $N_{neigbhor}$. Note that the specimen with $\phi = 0.37$ was excluded from the analysis due to the small field of view in the high-resolution tomograms, which limited our ability to obtain reliable statistics about GMB collapse and packing.

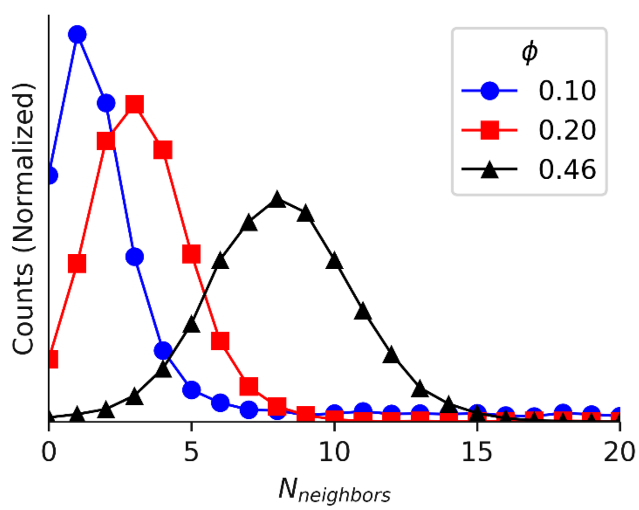

Fig. 4.5. Distribution of local GMB clustering for different syntactic foam specimens.

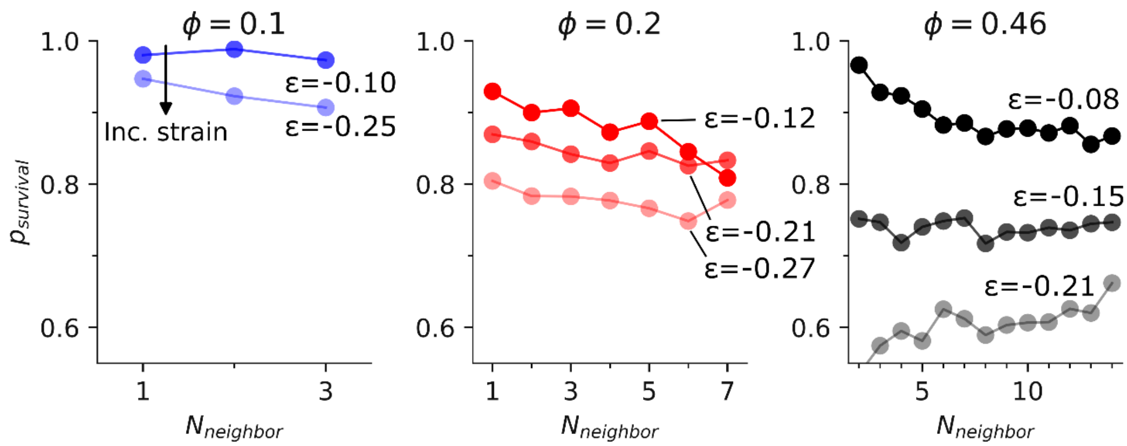

Fig. 4.6. Effects of local GMB clustering on the probability of GMB survival ($p_{survival}$) for different syntactic foams.

Clearly, closely-packed GMBs with large $N_{neighbor}$ collapsed earlier than more sparsely-packed GMBs. This trend was evident within each foam, and also in comparison between foams, implying that the local density of GMBs strongly moderated the damage behavior. The negative relationship was particularly strong for sparsely-packed GMBs ($N_{neighbor} < 10$), but the GMB survival rate was approximately uniform for larger $N_{neighbor}$. Thus, while particle clustering can accelerate the collapse of GMBs by intensifying the stress experienced in each particle [7], these effects diminish at higher packing densities.

While this trend between $N_{neighbor}$ and $p_{survival}$ is very strong, it cannot fully explain the variation in damage mechanisms between specimens with different ϕ. In particular, for GMBs with identical $N_{neighbor}$ at identical strain, $p_{survival}$ is lower in specimens with higher ϕ. As an example, $p_{survival}(\phi = 0.1, \varepsilon = -0.25) > p_{survival}(\phi = 0.2, \varepsilon = -0.21) > p_{survival}(\phi = 0.46, \varepsilon = -0.15)$ for all $N_{neighbor}$. In other words, the far-field GMB density also contributes the prediction of damage. Together, both ϕ and $N_{neighbor}$ independently control the initiation and propagation of damage in syntactic foams.

This trend explained the different damage patterns observed in the high-resolution tomograms (Fig. 4.3) and low-resolution DVC analysis (Fig. 4.4). Specifically, damage initiated and propagated earlier in closely-packed clusters of GMBs in all specimens; these particles had higher $N_{neighbor}$ compared to isolated GMBs. Thus, this would result in significant macroscopic strain and damage localization corresponding to the original spatial distribution of GMBs in the foam. With increasing ϕ, the size of the particle clusters increased, resulting in more severe strain variation.

Finally, there was some evidence that the relationship between $N_{neighbor}$ and $p_{survival}$ reversed after widespread GMB collapse (such that $p_{survival} < 0.70$), based on trends in the foam with $\phi = 0.46$. Only data from this specimen was available at this level of damage, since the other specimens were too compliant to achieve widespread GMB collapse. Theoretically, this could be attributed to the "stress shielding" effects in closely-packed GMB clusters, in which collapsed GMBs redistributed stress away from adjacent intact GMBs [7]. Given that the most densely packed GMBs were also most likely to have collapsed neighboring particles, the earliest GMBs to fail could inhibit failure of the other GMBs.

5. Discussion

These results provide the first *in situ* experimental study of damage localization in syntactic foams as a function of ϕ. The primary findings of the experiment are that (1) the distribution of damage in the syntactic foams evolves with the GMB volume fraction, and (2) these trends are mechanistically related to clustering of particles in the syntactic foam.

5.1. Role of matrix composition on damage mechanisms

The observed damage mechanisms in the elastomer-matrix syntactic foam differed substantially compared to the failure mechanisms reported for syntactic foams with epoxy, vinyl-ester resin, polyurethane (PU), and polypropylene (PP) matrices [9,10,18]. Specifically, the current analysis identified no shear bands that have been observed the stiff/brittle epoxy and vinyl-ester foams. Additionally, the propagation of damage along closely-packed chains of GMBs contrasted with the dispersed GMB collapse in the polyurethane foam, even at comparably high ϕ. Instead, dispersed GMB collapse occurred only at low volume fractions for $\phi < 0.30$, which agreed with recent *in situ* XCT analysis of a PDMS-matrix syntactic foam with $\phi \approx 0.22$ [6].

The absence of a shear-band damage mechanism is partially explained by the stiffness of the matrix material, where $E_{PDMS} = 3\ MPa$ [19] is much softer than $E_{epoxy} \approx E_{vinyl} = 3.0\ GPa$ [20]; in comparison to these rigid matrices that also exhibit strain localization, PDMS's superior compliance and elasticity should conceptually facilitate stress redistribution around damaged particles. On the other hand, this cannot explain the discrepancy between the PDMS foam and the PU or PP foams, which have $E_{PU} = 250\ MPa$ and $E_{PP} = 21\ MPa$. While the origin of this difference remains unclear, it is tentatively attributed to the different crush strengths of GMBs: the current A16 GMBs have thinner walls than reported those used by Adrien *et al.* [10]. Therefore, both the matrix and GMB composition affect the damage mechanisms, in addition to the reported effects of GMB clustering.

5.2. Distribution of damage in syntactic foams

Inspection of the *in situ* XCT damage measurements reveals a clear transition from *isolated* to *localized GMB collapse* at increasing ϕ. This is most clearly illustrated by the DVC strain fields, which are sensitive to the damage state within each analysis subvolume. At higher ϕ, both the amplitude and spatial frequency of strain variation indicated large regions of collapsed GMBs. In contrast, strain variation was minimal for smaller ϕ. These trends were confirmed by direct measurement of GMB collapse in the high-resolution tomograms, and agreed with the previously reported results for GMB/PDMS-matrix syntactic foams ($\phi = 0.23$ in [6], and $\phi = 0.37$ in [7]).

Intriguingly, these relationships were also consistent both *within* and *between* samples of different ϕ. That is, the high-resolution tomograms indicated that GMB collapse initiated earliest in closely-packed chains of particles, much like GMB collapse occurred more rapidly in the specimens with larger ϕ. This was particularly evident in the low volume fraction specimens (*i.e.*, $\phi = 0.10, 0.20$), which contained both isolated and clustered GMBs. The distinction became less prominent at higher ϕ, since the dense packing of GMBs effectively created a single network of closely-packed particles; damage correspondingly initiated throughout the entire specimen at low strain in the $\phi = 0.46$ specimen.

5.3. Role of $N_{neighbor}$ on damage mechanisms

Based on these trends, it was postulated that the damage behavior in syntactic foams could quantitatively be explained in terms of the local packing of GMBs. A statistic reflecting the GMB coordination number ($N_{neighbor}$) was developed, which was sensitive to both the local particle clustering and indirectly the global volume fraction. Analysis of GMB survival found a strong correlation between $N_{neighbor}$ and GMB collapse, where a higher proportion of closely-packed GMBs collapsed at earlier strains. This trend was consistent across specimens with different ϕ. Therefore, these experiments support a conclusion that damage in elastomeric syntactic foams is strongly predicted the local GMB packing, in addition to the effects of far-field GMB density (*i.e.*, ϕ).

In this sense, the results agreed several computational analyses of the effects of GMB clustering. Previous FE analyses by Yu *et al.* [14] assessed the role of particle clustering on tensile response of epoxy-matrix syntactic foams with a 3D representative unit cell, finding that models with increasing particle clustering and GMB volume fraction failed at lower tensile stresses and smaller strains. Similar trends were revealed by micromechanics models of multi-particle interactions by Croom *et al.* (for elastomer matrix syntactic foams) and Tagliavia *et al.* (for a generalized elastic matrix with axially-aligned particles) [7,21], which showed that decreased spacing between adjacent GMBs can magnify the peak stresses in the GMB walls. Including the current experiment, all of these results provide a consistent trend over a wide range of particle arrangements, matrix compliance, and volume fractions. Thus, control of particle clustering by manipulating $N_{neighbor}$ provides a useful tool to tailor the mechanical properties of syntactic foams.

6. Conclusions

In situ XCT compression testing of elastomer-matrix syntactic foams was performed to assess the roles of local GMB clustering and volume fraction on the damage mechanisms. Measurement of the damage trends by quantitative image analysis, DVC and statistical modeling of the GMB survival probability revealed a transition from isolated to spatially clustered GMB collapse with increasing ϕ and particle clustering. At higher volume fractions, GMB collapse spread between closely-packed particles, forming pseudo crush bands and/or pockets of entirely collapsed GMBs; contrastingly at lower volume fractions, damage was dispersed due to low connectivity between GMBs. Within individual foams of nominally identical ϕ, damage tended to initiate more rapidly in closely-packed chains of GMBs rather than isolated particles. These trends were mirrored by DVC results, which identified increased strain variation at larger ϕ that were co-located with clusters of damaged particles. These behaviors were reconciled in terms of the GMB coordination number $N_{neighbor}$, which scales with both local clustering effects and global volume fraction. Probability of collapse was found to increase with $N_{neighbor}$ for all specimens, implying that the effects of local clustering and volume fraction can be adequately explained in terms of this statistic. This finding should guide the design of syntactic foams with superior crush strength and energy absorption.

References

[1] Gupta N, Kishore, Woldesenbet E, Sankaran S. Studies on compressive failure features in syntactic foam material. J Mater Sci 2001;36:4485–91. doi:10.1023/A:1017986820603.

[2] Kim HS, Plubrai P. Manufacturing and failure mechanisms of syntactic foam under compression. Compos Part A Appl Sci Manuf 2004;35:1009–15. doi:10.1016/j.compositesa.2004.03.013.

[3] Gupta N. A functionally graded syntactic foam material for high energy absorption under compression. Mater Lett 2007;61:979–82. doi:10.1016/j.matlet.2006.06.033.

[4] Gupta N, Woldesenbet E, Mensah P. Compression properties of syntactic foams: effect of cenosphere radius ratio and specimen aspect ratio. Compos Part A Appl Sci Manuf 2004;35:103–11. doi:10.1016/J.COMPOSITESA.2003.08.001.

[5] Gupta N, Woldesenbet E. Microballoon Wall Thickness Effects on Properties of Syntactic Foams. J Cell Plast 2004;40:461–80. doi:10.1177/0021955X04048421.

[6] Patterson BM, Cordes NL, Henderson K, Williams JJ, Stannard T, Singh SS, et al. In situ X-ray synchrotron tomographic imaging during the compression of hyper-elastic polymeric materials. J Mater Sci 2016;51:171–87. doi:10.1007/s10853-015-9355-8.

[7] Croom BP, Jin H, Mills B, Carroll J, Long K, Brown J, et al. Damage mechanisms in elastomeric foam composites: Multiscale X-ray computed tomography and finite element analyses. Compos Sci Technol 2019;169:195–202. doi:10.1016/j.compscitech.2018.11.025.

[8] Brown JA, Carroll JD, Huddleston B, Casias Z, Long KN. A multiscale study of damage in elastomeric syntactic foams. J Mater Sci 2018;53:10479–98. doi:10.1007/s10853-018-2263-y.

[9] Huang R, Li P. Elastic behaviour and failure mechanism in epoxy syntactic foams: The effect of glass microballoon volume fractions. Compos Part B Eng 2015;78:401–8. doi:10.1016/J.COMPOSITESB.2015.04.002.

[10] Adrien J, Maire E, Gimenez N, Sauvant-Moynot V. Experimental study of the compression behaviour of syntactic foams by in situ X-ray tomography. Acta Mater 2007;55:1667–79. doi:10.1016/j.actamat.2006.10.027.

[11] Lachambre J, Maire E, Adrien J, Choqueuse D. In situ observation of syntactic foams under hydrostatic pressure using X-ray tomography. Acta Mater 2013;61:4035–43. doi:10.1016/j.actamat.2013.03.017.

[12] Huang R, Li P, Liu T. X-ray microtomography and finite element modelling of compressive failure mechanism in cenosphere epoxy syntactic foams. Compos Struct 2016;140:157–65. doi:10.1016/j.compstruct.2015.12.040.

[13] Panteghini A, Bardella L. On the compressive strength of glass microballoons-based syntactic foams. Mech Mater 2015;82:63–77. doi:10.1016/j.mechmat.2014.12.005.

[14] Yu M, Zhu P, Ma Y. Effects of particle clustering on the tensile properties and failure mechanisms of hollow spheres filled syntactic foams: A numerical investigation by microstructure based modeling. Mater Des 2013;47:80–9. doi:10.1016/j.matdes.2012.12.004.

[15] Croom BP, Wang W-M, Li J, Li X. Unveiling 3D Deformations in Polymer Composites by Coupled Micro X-Ray Computed Tomography and Volumetric Digital Image Correlation. Exp Mech 2016;56:999–1016. doi:10.1007/s11340-016-0140-7.

[16] Croom BP, Jin H, Mills B, Li X. Effect of fragile speckle patterns on accuracy of digital volume correlation. Exp Mech 2019;In press.

[17] Patterson BM, Escobedo-Diaz JP, Dennis-Koller D, Cerreta E. Dimensional quantification of embedded voids or objects in three dimensions using X-ray tomography. Microsc Microanal 2012;18:390–8. doi:10.1017/S1431927611012554.

[18] Gupta N, Ye R, Porfiri M. Comparison of tensile and compressive characteristics of vinyl ester/glass microballoon syntactic foams. Compos Part B Eng 2010;41:236–45. doi:10.1016/j.compositesb.2009.07.004.

[19] Johnston ID, McCluskey DK, Tan CKL, Tracey MC. Mechanical characterization of bulk Sylgard 184 for microfluidics and microengineering. J Micromechanics Microengineering 2014;24:035017. doi:10.1088/0960-1317/24/3/035017.

[20] Ziaee S, Palmese GR. Effects of temperature on cure kinetics and mechanical properties of vinyl-ester resins. J Polym Sci Part B Polym Phys 1999;37:725–44. doi:10.1002/(SICI)1099-0488(19990401)37:7<725::AID-POLB23>3.0.CO;2-E.

[21] Tagliavia G, Porfiri M, Gupta N. Analysis of particle-to-particle elastic interactions in syntactic foams. Mech Mater 2011;43:952–68. doi:10.1016/j.mechmat.2011.08.008.

Chapter 5:
Unveiling 3D deformations in polymer composites by coupled micro X-Ray computed tomography and digital volume correlation

1. Introduction

Lightweight carbon fiber reinforced polymer (CFRP) composites are increasingly used in automotive and aerospace industries to reduce structural weight and improve fuel efficiency, and often must be connected to other materials. Dissimilar material joining techniques, including friction stir welding [1], friction stir blind riveting [2,3], adhesive joining [4], and laser welding [5,6], all locally alter microstructure and mechanical properties, introducing complex three-dimensional (3D) anisotropic deformation behavior that is not yet well understood at a microstructural level. Conventional *in situ* measurements based on microscopy and surface deformation measurements inherently cannot capture the internal deformation, and inadequately describe the influence of the 3D microstructure on the deformation mechanisms. Only with 3D experimental methods can we fully unveil the local deformation behavior in dissimilar material joints.

In this work, coupled *in situ* X-ray computed tomography (XCT) and digital volume correlation (DVC) [7] is employed to quantify the anisotropic deformation behavior in a friction stir blind rivet joint of CFRP. While XCT and DVC techniques have frequently been used to measure the displacement in porous materials [8–13], it has generally been asserted that non-porous CFRP is incompatible with this technique, due to low contrast between the fibers and matrix phases [14]. Here, we demonstrate that the fibers and matrix exhibit adequate contrast and that irregular fiber orientations in the chopped fiber composite enable reliable displacement measurement.

Compared to traditional sample surface or cross section examination of composites, XCT and DVC techniques are preferred for several reasons. First, volumetric data from XCT scans reveals sub-surface microstructural characteristics that are not evident during cross section analysis or postmortem fracture examination. In addition, examination of these 3D images enables quantitative analysis of three-dimensional features such as pore geometry and fiber orientation [15], in contrast to other techniques that only sample 2D projections of these data. Most importantly, *DVC techniques extract quantitative deformation data* from images acquired during *in situ* XCT mechanical testing [8,9,16,17]. These displacement measurements have subvoxel accuracy and enable computation of the three-dimensional strain tensor at all locations throughout the imaged volume. When coupled with XCT measurements of microstructure, this data may be used develop quantitative, mechanics-based models of deformation phenomena such as internal cracking and buckling.

Here, the newly developed XCT and DVC techniques are applied to friction stir blind rivet (FSBR) lap joints between CFRP and metal workpieces to reveal anisotropic deformation mechanisms within CFRP, and data is used to propose a novel constrained buckling model to explain behavior observed in the specimen. Because FSBR uses friction from a rapidly rotating fastener to soften and drive through workpieces (Fig. 5.1), combined thermal and mechanical loads create a stir zone adjacent to the rivet with distinct composition, fiber orientation and mechanical properties (Fig. 5.1e); given these complex boundary conditions in the specimens, combined XCT and DVC experiments are essential to understanding the mechanics of FSBR-process materials. Under compression the rivet hole geometry causes combined axial and bending deformation, which amplifies compressive stresses near the rivet hole and may lead to buckling within the stir zone. In this work, the DVC technique quantitatively describes the microstructural influence on deformation within the stir zone. In accordance with the observed stress state and the complex stir zone microstructure, a buckling model developed based on locally varying microstructure within the stir zone is established in Section 2.

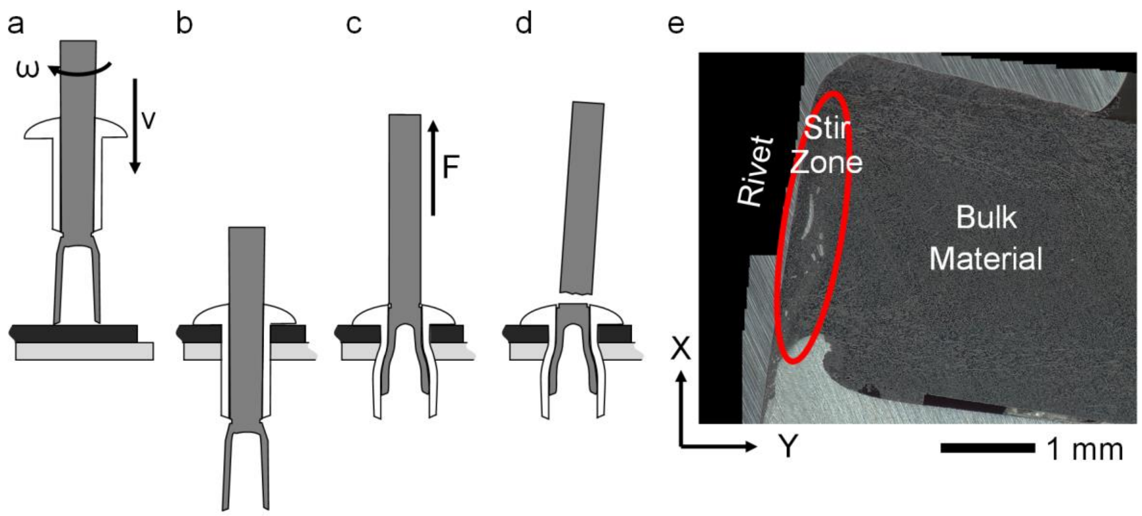

Fig. 5.1. Overview of FSBR process, adapted from Ref. [18]. (a) A blind rivet rotating at speed ω is driven through the workpieces at feed rate ν until (b) the shank head is flush with the top workpiece. Frictional forces heat and soften the workpieces, enabling the rivet to penetrate easily through the workpieces. (c) The mandrel is pulled with force F and (d) broken at a notch to create a FSBR joint. (e) Optical micrograph showing representative microstructure of CFRP after FSBR processing, with stir zone highlighted.

2. Development of constrained buckling model

For a bilayer specimen with distinct local mechanical properties and low interfacial cohesion, it is reasonable to model the separate regions as partially isolated volumes. Following this assumption, we introduce a buckling model to describe the compressive deformation of a compliant layer adjacent to a bulk material; in terms of a FSBR CFRP composite specimen, these sections refer to the stir zone and bulk composite, which may behave independently due to the FSBR altered microstructure and poor fiber/polymer interfacial cohesion in the stir zone. The thin stir zone's inertial properties make it sensitive to bending and buckling, which also means that its deformation is governed by contact with the substrate.

In Fig. 5.2, a model based on buckling of eccentrically loaded columns is presented to accommodate boundary conditions imposed by the interacting coating (corresponding to the thin stir zone) and substrate (bulk composite material). First, we assume an axial load F offset from the column by distance e which induces bending moment such that the bulk material preferentially bends away from the rivet hole. Observing the stir zone's curvature, we note that the natural buckling direction is obstructed by the adjacent bulk material and assume lateral deflection in the opposite direction (Fig. 5.2a), which subsequently resists the applied bending moment; this assumption differentiates this model from more conventional (*i.e.*, unconstrained) eccentrically-loaded column buckling models. Additionally we impose constraints on the left and right edges of the coating to reflect locally stiff regions of material that resist bending, such as areas of the stir zone stiffened by metal inclusions. Within this region defined by four sides of contact with the substrate, the coating may buckle away from the substrate.

With these assumptions, lateral deflection of a plate $\mathrm{v}(x, z)$ can be related to the combined loading using Kirchhoff plate theory. First, we apply normalized axial and bending loads per unit length, $P = F/L$ and $M_x = Fe/L$, to the top edge of a plate, which are induced by the bulk material deformation. Next, displacement on unloaded edges is constrained as per Fig. 5.2b. Assuming a separable form[1] for out of plane deflection,

$$v(x, z) = f(x)g(z) = sin\left(\frac{\pi x}{L}\right)(Asin(kz) + Bcos(kz) - e) \tag{5.1}$$

where $k^2 = \frac{P}{EI}$ and unknown constants A and B can be found with appropriate boundary conditions, we can derive a solution to Kirchhoff's plate bending model:

$$\begin{bmatrix} M_x \\ M_z \\ M_{xz} \end{bmatrix} = -D \begin{bmatrix} 1 & \nu & 0 \\ \nu & 1 & 0 \\ 0 & 0 & (1-\nu) \end{bmatrix} \begin{bmatrix} \partial^2 v/\partial z^2 \\ \partial^2 v/\partial x^2 \\ \partial^2 v/\partial x \partial z \end{bmatrix} \tag{5.2}$$

where $D = 2t^3E/3(1-\nu^2)$, t is half-thickness of plate, E is elastic modulus and ν is Poisson's

---

[1] The form of $g(z)$ is obtained from the analogous one-dimensional problem for eccentrically loaded column buckling.

ratio. Free body diagram (Fig. 5.2c) analysis reveals that M_x can be related to the applied loads

$$M_x(x,z) = -P\big(e + v(x,z)\big) \tag{5.3}$$

which provides a convenient way to determine unknown coefficients *A* and *B* given experimental displacement data.

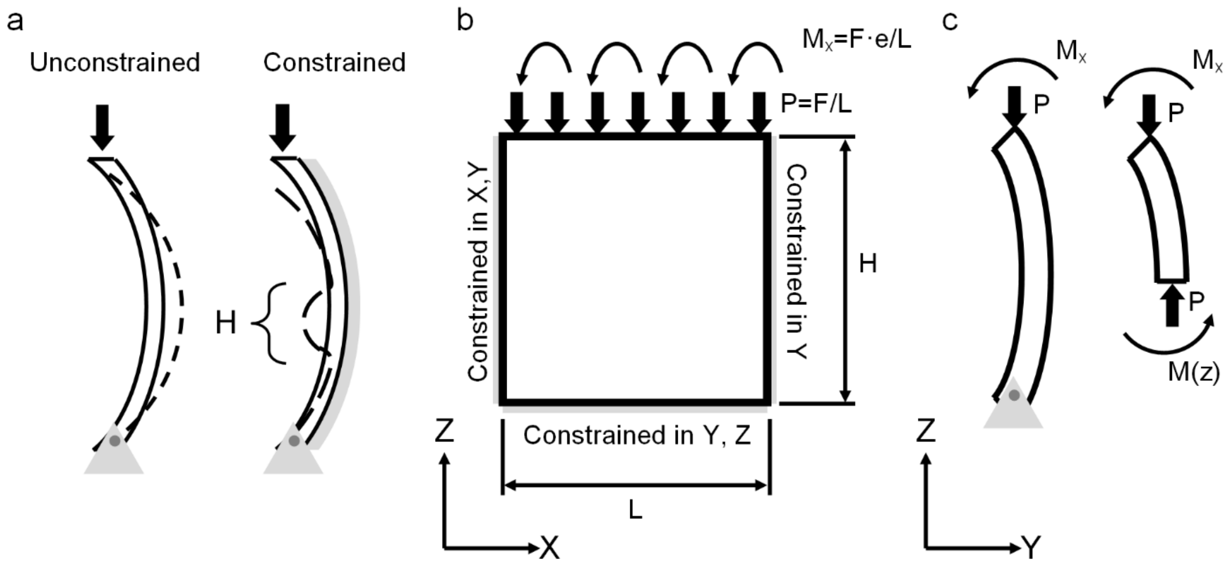

Fig. 5.2. Development of constrained buckling model. (a) Comparison of constrained and unconstrained buckling behavior, (b) schematic of buckling boundary conditions, and (c) free body diagram assuming positive (unconstrained) deflection.

3. Materials and methods

Quantification of local deformation mechanisms requires simultaneous characterization of mechanical behavior and microstructure. To this end, a series of experiments and data processing techniques were developed to provide detailed mechanical and microstructural information.

3.1. Sample preparation

CFRP-Al FSBR lap joints were prepared as described in Fig. 5.1 by joining chopped-fiber CFRP composite with nominally random fiber orientation (fiber length was 300 – 500 μm) to aluminum alloy (AA5754-O) with a zinc-coated, mild-steel blind rivet. The layup is illustrated in Fig. 5.3a and the work material details are summarized in Table 5.1. The rivet diameter was 6.5 mm. The listed CFRP elastic modulus was obtained experimentally from compression tests of bulk materials samples, which was somewhat between values of the PA 66 matrix and commonly cited flexural stiffness values for CFRP.

Low-vacuum scanning electron microscopy (SEM; FEI Quanta 650) microstructural measurements were used to validate the XCT characterization techniques. Energy dispersive X-ray spectroscopy (EDS; Oxford Instruments) analysis revealed that the large (>100 µm) metal inclusions in the stir zone (visible in circled region of Fig. 5.1e) resulted from the aluminum workpiece (Fig. 5.14 in Appendix). Much smaller zinc particles from the rivet coating (~1 µm;) were also observed.

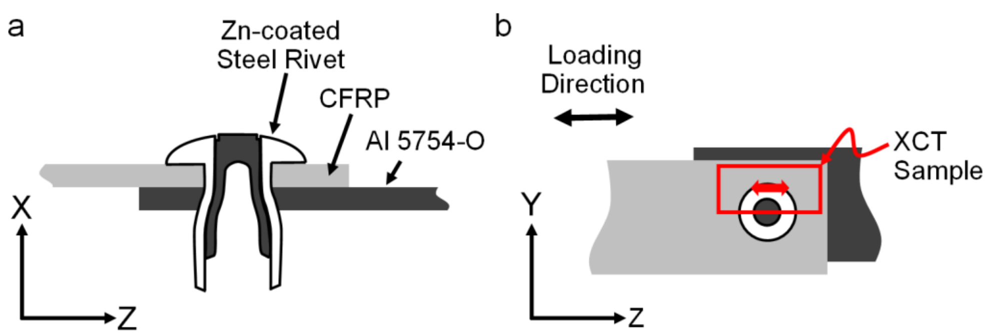

Fig. 5.3. XCT samples extracted from CFRP material in lap shear FSBR specimens. (a) Layup of the FSBR sample is shown with lap-shear specimen cross section, (b) XCT samples were extracted near the rivet hole.

Table 5.1. Properties of joined materials

Materials	***Size (mm^3)***	***Elastic Modulus (GPa)***	***Yield Strength (MPa)***	***Ultimate Tensile Strength (MPa)***	***Elongation (%)***
AA5754-O (Al)	76.2 × 38.1 × 3	69	102	234	21%
CFRP (PA 66 with 30% carbon fiber)	76.2 × 38.1 × 3	8.8	N/A	N/A	1-3%

3.2. In situ XCT compression of CFRP

A custom loading stage was manufactured for *in situ* compression loading (Fig. 5.4a). A manually-actuated, fine-threaded screw axially compressed the specimen, which was secured by grip plates and cone-tipped set screws. The tip of the actuation screw was rounded to minimize torque applied to the specimen; no specimen rotation was observed during the tests. Custom-geometry test coupons (Fig. 5.4b) were machined from the sectioned lap-shear specimen using low machining speeds; the rivet hole formed one face of the sample, which maintained the integrity of the stir zone. We note that the specimen geometry imparted a combined compression-bending load; these trends were recreated with finite element (FE) simulations described in Section 6. The sample's thickness was tapered slightly near the gage section to produce a sample with nominal cross section of $2.9 \times 2.25\ mm$.

To support the compressive load on the specimen, the loading mechanism was encased in a hollow polycarbonate cylinder with wall thickness of 1.6 mm. The cylindrical geometry enabled full 360° X-Ray access to the sample and also minimized orientation-dependent distortions that could affect the accuracy of the computed tomography reconstruction. Some beam attenuation due to the polycarbonate cylinder was observed, but experimental imaging parameters (Table 5.2) were selected to minimize the cylinder's effect on image quality.

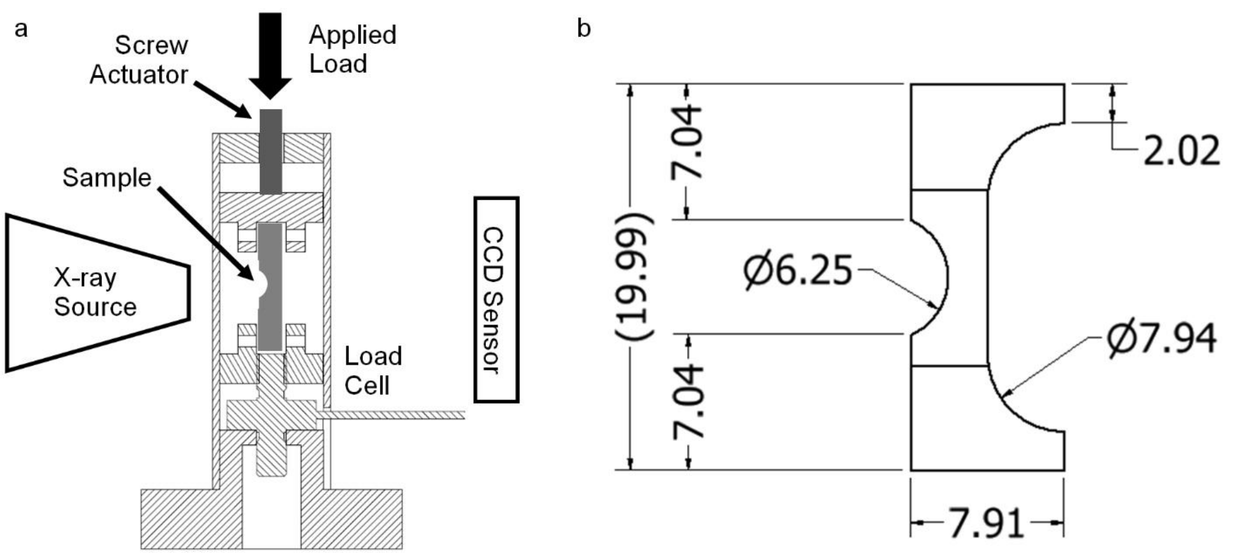

Fig. 5.4. Design of XCT loading system. (a) Compression loading frame with 450 N capacity. (b)

Geometry of rivet hole compression specimen (unit: mm).

Table 5.2. XCT imaging parameters

	Parameter	***Value***
X-Ray Source	Voltage	$60\ keV$
	Power	$8\ W$
	Current	$133\ \mu A$
Image Acquisition	Scan range	$-93°\ to + 93°; 325\ images$
	Exposure	$60\ seconds$
Loading Stage	Initial Load	$0 - 400\ N\ (0 - \ 90\ lbf)$

In situ imaging of the rivet sample was acquired with a commercial XCT scanner (XRadia MicroXCT-200) at nominal compressive loads from 0 to 68 MPa $(0 - 400\ N)$; these loads were sufficient to produce axial strains on the order of $\epsilon_{zz} = -0.04$. It is noted that the CFRP samples demonstrated strong room-temperature strain relaxation behavior, with loads consistently decaying to 71% of the peak value; additional testing revealed this to be a constant strain process, such that deformation observed during a 6-hour XCT scan reflected the initial load. Critically, this process did not induce motion blur within the volumetric images, and did not affect DVC calculations.

Fig. 5.5 shows a representative reconstructed image of the specimen (FEI Avizo software), which has sufficient resolution to capture individual fibers and microstructural features. The images demonstrated systematic and anomalous bright bands, which were determined to be a reconstruction artifact. These bands biased the intensity-based microstructure analysis techniques (Section 3.3), and for this purpose were corrected with a flat-field correction technique. It was found that these artifacts did not affect DVC calculations; deformation was calculated with DVC using the raw (uncorrected) volumetric images.

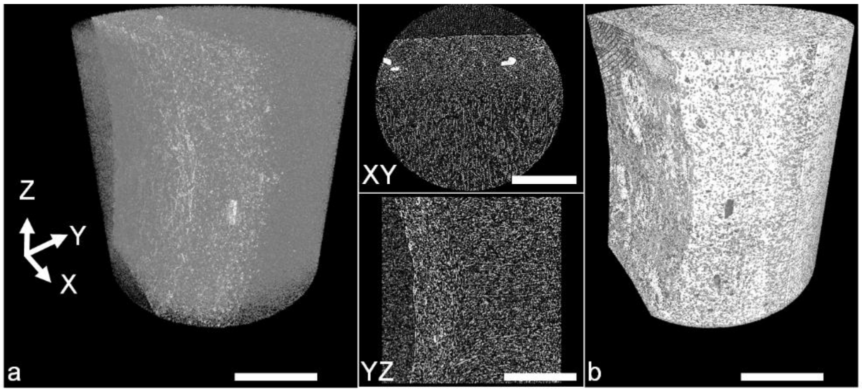

Fig. 5.5. Representative XCT renderings of rivet hole specimen (a) before and (b) after image segmentation, with center insets showing representative cross sections on the XY and YZ planes. The rivet penetration direction is along the X-axis, and the rivet hole surface is on the negative-Y face of the volume. Scale bar: 500 μm

3.3. Image processing

Scanned images were segmented into constituent elements using by thresholding the image intensity to quantitatively identify phases associated with fiber, matrix, porosity and metal inclusions. These methods were automated in Python v3.4 using the NumPy library [19].

Inspection of the reconstructed volumes revealed that microstructural features could readily be distinguished based on differences in X-ray attenuation. After denoising reconstructed volumes with a Gaussian filter, intensity histograms were thresholded to demarcate pore, matrix, fiber, aluminum and zinc constituents in the images; certain regions of the images were excluded from segmentation by assigning boundaries for the rivet hole surface and reconstructed volume. Typical results from segmentation are shown in Fig. 5.5b. The thresholds were adjusted for each image to produce accurately sized fiber, pore, aluminum and zinc elements with respect to SEM measurements, and that these segmented images provided consistent and accurate fiber and pore volume fraction measurements that agreed with SEM observations (Figs. 5.15 and 5.16 in Appendix).

From the segmented images, the volume fraction of constituent materials was calculated by determining the fraction of voxels containing the material of interest with respect to the total number of voxels in a prescribed volume. By carefully defining the analyzed region, volume fractions were calculated at local and global scales, which enabled quantitative comparisons of composition and microstructure between regions (*e.g.*, bulk material vs. stir zone) as well as local variation in microstructure with high resolution. In this work, volume fractions were calculated by two separate methods. First, data was projected along the YZ plane, which aligned with the CFRP plate orientation in the FSBR joint (Fig. 5.3b); volume fractions for fibers, pores and metal inclusions were calculated by analyzing individual rows of data in the X axis direction. Second, local volume fractions were calculated through the entire reconstructed volume by analyzing small cubic subsets of size [35 voxels]^3 on a grid with center-to-center subset spacing of 17 voxels (equivalent to [47 μm]^3 and 20 μm, respectively).

Finally, a template matching technique was applied to the segmented volumetric images to probe local fiber orientation. First, a binary fiber image f was generated by assigning all fiber voxels a value of 1 and all remaining voxels a value of 0. Second, a smaller cubic template g of size n^3 was created to contain an imitation fiber of a particular orientation. Voxels within this imitation fiber element were assigned values according to Eq. 5.4 and were normalized by a factor of N, which was the count of all nonzero voxels within the imitation fiber element,

$$g(\boldsymbol{\delta x}) = \begin{cases} 1/N & if\ (\boldsymbol{\delta x})\ corresponds\ to\ fiber\ location \\ 0 & otherwise \end{cases} \tag{5.4}$$

The two volumes were correlated at all locations $\boldsymbol{x}$ within the binary fiber image,

$$C_{fiber}(\boldsymbol{x}) = \sum_{\delta x\ in\ g} f(\boldsymbol{x} + \boldsymbol{\delta x}) \times g(\boldsymbol{\delta x}) \tag{5.5}$$

where $\boldsymbol{\delta x}$ represented the local coordinates relative to $\boldsymbol{x}$. The resulting correlation values C_{fiber} ranged from 0 to 1 and modeled the degree of overlap between the binary fiber image and imitation fiber element at a given location. In this sense, strong correlation values suggested that a fiber at that location possessed the orientation of the fiber in the imitation image. By repeating this process with fiber elements of many different fiber orientations, the orientation of every fiber within the reconstructed volume was extracted. It was found that using a fiber diameter of 2.5 voxels (3.4 μm), fiber length of 17 voxels (22.8 μm), and a correlation threshold of 0.65 determined fiber orientation to an accuracy better than $\pm 5°$. This approach resembles other fiber tracking schemes implemented for continuous fiber composites [20,21].

3.4. Digital volume correlation analysis

The reconstructed volumes captured at 0, 22 and 44 MPa compressive loads were correlated using commercial DVC software (Vic-Volume, Correlated Solutions Inc.) to calculate the full-field displacement and strain tensors using subset size of [35 voxels]^3 and subset spacing of 15 voxels (equivalent to [47 μm]^3 and 20 μm, respectively). Fibers, pores and other microstructural features with pseudo-random orientation, size and location provided an intrinsic high-contrast speckle pattern for displacement calculations. Accuracy of the calculations was assessed using rigid body motion analysis, which found the accuracy of displacement calculations to better than $\pm 0.7\ \mu m$, and strain calculations to be better than $\pm 1\%$ (based on 95% confidence intervals). This confidence interval was much smaller than anticipated variation in deformation due to local microstructure and loading conditions.

To study local deformation in the stir zone, the deformations of initially vertical paths (defined by groups of subsets with identical X and Y coordinates) were compared using calculated displacements for the 44 MPa image at several positions within the stir and bulk material zones. Axial and lateral deflections along these paths were compared with local microstructure and the buckling model described in Section 2.

4. Microstructural analysis

Prior studies revealed that CFRP in FSBR joints failed near the rivet hole, implying that the stir zone microstructure strongly influences the overall joint performance [3]. As the strength and stiffness of fiber-reinforced composites are intimately related to fiber volume, porosity and fiber orientation, we explored these parameters near the rivet hole in the stir-affected zone and compared these values to the bulk material. The resulting microstructure description is related to mechanical deformation to provide a holistic understanding of microscale deformation in FSBR CFRP joints.

4.1. Volume fraction analysis

Projections of fiber, pore and metal inclusion volume fraction on YZ plane (Fig. 5.6a-c) clearly demonstrated microstructural differences between the stir zone and bulk materials, with a distinct interface between these regions located 250 µm from the rivet hole surface; for this work, this transition was used to demarcate the stir zone and bulk material regions. By sampling the composition of three-dimensional subsets within the stir zone and bulk regions, statistically significant increases in fiber, pore and metal inclusion volume fraction ($p < .001$, using two-sample Kolmogorov-Smirnov tests) were observed in the stir zone compared to the bulk material (Fig. 5.6d-f). Specifically, mean fiber volume fraction within the stir zone was $\bar{x}_{f,stir} = 38\%$, compared to bulk value $\bar{x}_{f,bulk} = 29\%$; pore volume fraction was $\bar{x}_{p,stir} = 3.7\%$ compared to $\bar{x}_{p,bulk} = 1.5\%$; and metal volume fraction was $\bar{x}_{m,stir} = 4.1\%$ compared to $\bar{x}_{m,bulk} = 0.4\%$. While the fibers and pores within the stir zone were evenly distributed, the elevated metal volume fraction was primarily due to the presence of sparsely distributed large metal inclusions. SEM analysis indicated that the small metal inclusions (1-5µm) were zinc, and the large metal inclusions (10-100 µm) were aluminum in composition (Fig. 5.14 in Appendix). The distribution of large aluminum inclusions in the stir zone was notable, as the juxtaposition of very stiff metal versus comparatively soft CFRP (elastic modulus $E_{al} \approx 70\ GPa$ versus $E_{cfrp} \approx 8.8\ GPa$) may have created unusual local deformation behavior. Analysis in Section 5.3 revealed that the extremely stiff aluminum inclusions prevented local buckling in certain areas of the stir zone.

The composition within the stir zone illuminated the harsh loading environment during processing, which is not currently well studied. The only possible source for the large aluminum inclusions was from the workpiece material to which the CFRP plate was being joined. The aluminum inclusions possessed a streamlined geometry that was aligned tangentially to the rivet hole. In conjunction, these findings indicated high operating temperatures that exceeded the melting point of the aluminum alloy (~600°C). At this temperature, the zinc coating on the rivet as well as the PA66 matrix would both be molten; indeed, this would explain the stir zone's axisymmetry as the molten CFRP was spun by the rivet.

Since the region of increased fiber and pore volume fractions had a sharply defined boundary at the edge of the stir zone, their composition may be explained in terms of this harsh processing environment. At the elevated operating temperature, the rotating rivet head tangentially flowed the molten material within the stir zone. A portion of this material was expelled as flash beneath the rivet head, which is visible in Fig. 5.1. The flash appeared to have low fiber volume fraction, meaning that the stir zone was left with an enriched fiber content. During processing it was believed that the rivet head entrained air pockets with in the stir zone, which became frozen into the matrix upon cooling.

In total these measurements suggested a completely different microstructure in the stir zone compared to the bulk material, which made *a-priori* prediction of mechanical response within the stir zone quite difficult. The stir zone simultaneously possessed increased porosity as well as the addition of large metal inclusions. This competition between nominally softening and stiffening features would hinder the development of accurate micromechanical simulations without high-resolution experimental data, such as those provided by and XCT and DVC.

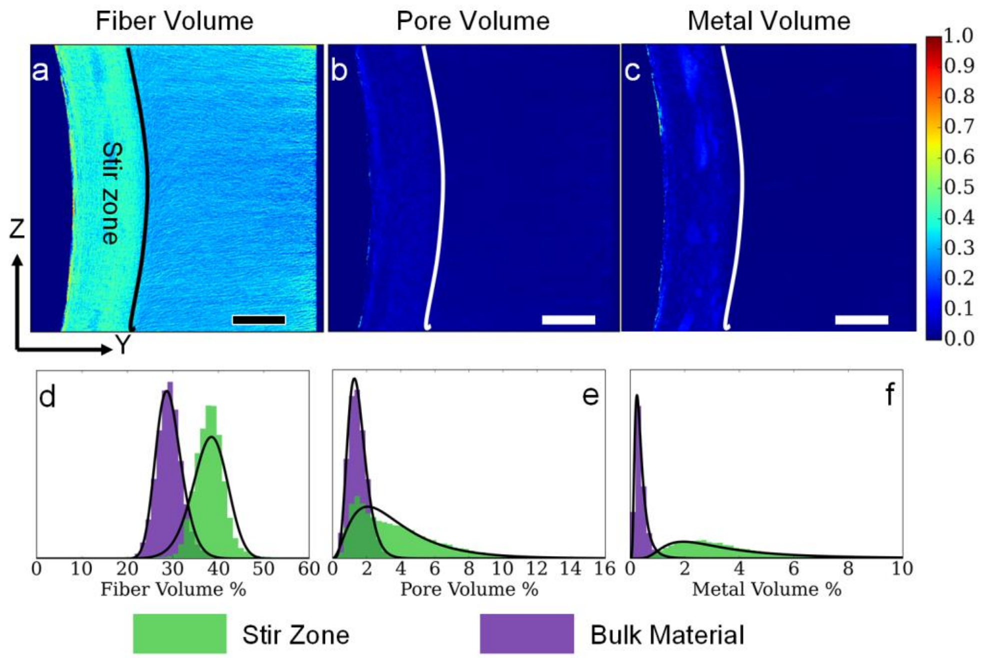

Fig. 5.6. Volume fractions calculated for rivet-hole specimen. Top row: Projections of (a) fiber, (b) pore and (c) metal inclusion volume fraction calculations onto YZ plane. Bottom row: Histogram of volume fractions calculated at subsets throughout 3D image for (d) fibers, (e) pores and (f) metal inclusions. Scale bars: 250 µm

4.2. Fiber orientation

The fiber orientation is compared for the stir zone and bulk materials in Fig. 5.7, which shows that fibers in the stir zone were partially reoriented to align with the rivet hole surface. The primary fiber orientation within the volume of interest in the bulk material was $\phi = 90°$, which was parallel to the XY plane and perpendicular to the rivet hole surface. Fibers in the stir zone had a larger ϕ measurement, suggesting that fibers were partially realigned with the motion of the rivet shank during FSBR processing (the rivet was spun around the X axis, creating a tangential velocity nominally parallel to $\phi = 0° = 180°$).

The altered fiber orientation supports evidence of material flow presented in Section 4.1. In a molten state, material flow preferentially aligned fibers tangential to the rivet hole surface

($\phi = 0° = 180°$). However, the difference in fiber orientations was subtler than would perhaps be expected given this simple model. This discrepancy suggested a complex flow state within the stir zone due to turbulence as well as complex transient heat transfer. In summary, despite the composite having pseudo-random fiber orientation at larger length scales, fiber orientation was relatively uniform within each region and oriented at a 90° orientation.

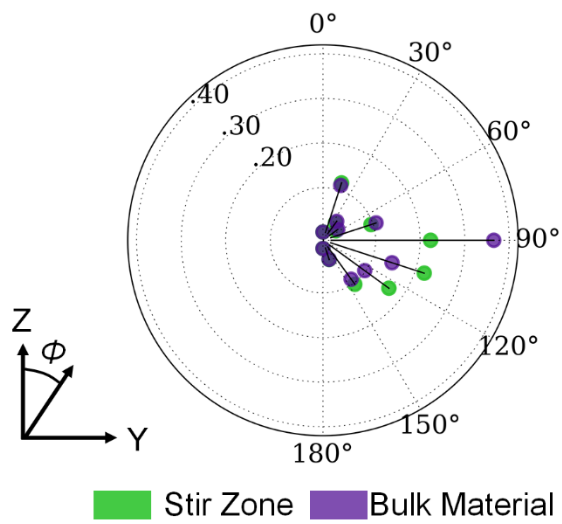

Fig. 5.7. Comparison of fiber orientation in the stir zone and bulk materials.

5. In situ mechanical testing results

5.1. Axial strain

Axial strain was calculated using DVC at 22 and 44 MPa loads (Fig. 5.8). In this figure, the rivet hole surface is depicted by the concave surface on the negative-Y face of the volume, and is marked by the black arc. Insets shown to the right demonstrate deformation on the interior of the volume. Higher compression was observed in the stir zone, consistent with finite element predictions of combined bending and axial loads (Section 6). This combined axial-bending trend was observed within the volume at both 22 and 44 MPa, with higher levels of compression near the rivet hole surface, supporting the stability and accuracy of the DVC calculations. This trend was persistent throughout the entire analyzed volume and also loading history, and the gradient in strains was larger than the margin of error associated with strain calculations.

After accounting for the accuracy of DVC strain calculations and global strain gradients due to bending and hole geometry, any axial strain concentration in the stir zone was determined to be small or inconclusive. The absence of a pronounced concentration was consistent with FE simulations of specimens with stiff stir zones (Section 6), although the magnitude of these gradients was anticipated to be small due to the limited size of the stir zone compared to the bulk material. This suggested that the increased fiber and metal inclusion content contributed to enhanced material stiffness in the stir zone.

The axial strain field appeared continuous at the interface between the stir zone and bulk materials, suggesting continuous material deformation in the axial direction with no interfacial fracture. However, since the interface was primarily aligned with the Z axis, interfacial slip would have manifested as shear strains γ_{yz}while interfacial crack opening would likely appear as ε_{yy} strains. Neither of these trends could be observed with axial strain maps.

Localized bands of high axial compression on the rivet hole surface marked by (*) revealed a nonuniform deformation response in certain areas of the stir zone. These bands demonstrated larger compression by a factor of ~2 compared to the rest of the stir zone (e.g., $\varepsilon_{zz} = -.05$ vs. $\varepsilon_{zz} = -.02$), which was much larger than the margin of error determined in the sensitivity study. These strain concentrations were consistent with kinking caused by localized buckling, which was observed visually in the volumetric reconstructions; these trends are discussed further in Section 5.3.

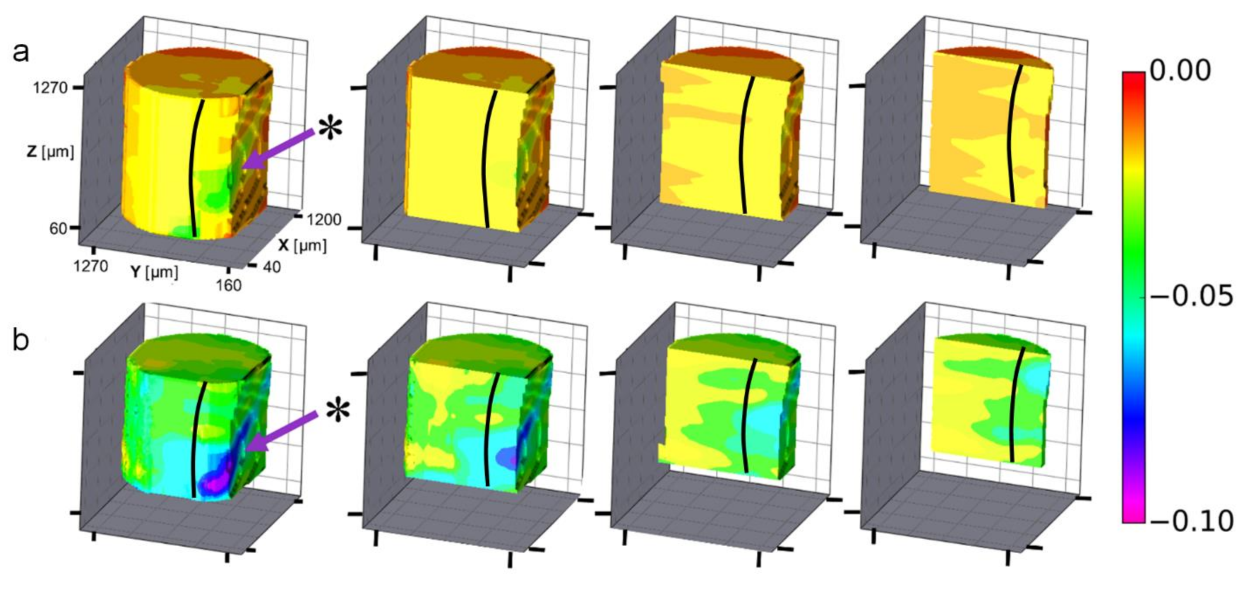

Fig. 5.8. Calculated axial strain ε_{zz} at (a) 22 MPa and(b) 44 MPa compression. The axial strain concentration on the rivet hole surface is marked with (*).

5.2. Shear strain

Shear strain γ_{yz} was similarly calculated for 22 and 44 MPaloads in the rivet hole specimen, with results summarized in Fig. 5.9. With the exception of local strain concentrations, shear strains were small and centrally distributed around $\gamma_{yz} = 0$ at both loads, which was also consistent with FE results (Section 6). In contrast to the average shear response within the bulk material, a large shear strain was observed at the interface between the bulk material and stir zone, which indicated a gradient in axial deformation across this boundary. This gradient was persistent throughout the thickness of each reconstructed volume, as marked by the green and yellow vertical bands observed in the cross-section insets within Fig. 5.9. Importantly, the magnitude of this shear strain increased proportionally to the applied load, with typical values of $\gamma_{yz} = .008$ and $\gamma_{yz} = .017$ for the images acquired at 22 and 44 MPa, indicating a linear elastic response at the interface. Since no visible crack was observed at the interface in the XCT reconstructions, the likely cause of this observed shear strain was genuine shear deformation rather than interfacial slip. In practical terms, this finding suggested that the stir zone was strongly adhered to the bulk material with a thin compliant layer and was unlikely to delaminate under compressive loads.

Additional concentrations were observed on the rivet hole surface, as marked by (†) and (‡) on the figures. The central concentration marked by (†) corresponded with severe local buckling (see Section 5.3), where fiber and material reorientation introduced a large shearing deformation in the YZ plane. Comparison with metal volume fraction measurements indicated that the concentration marked by (‡) occurred below a large metal inclusion (the light blue particles in Fig. 5.10a); this concentration may have been caused by the distribution of proportionally higher load carried by rigid metal inclusion to surrounding CFRP. It was noted that all of these shear strain concentrations were distinct from the axial strain concentrations.

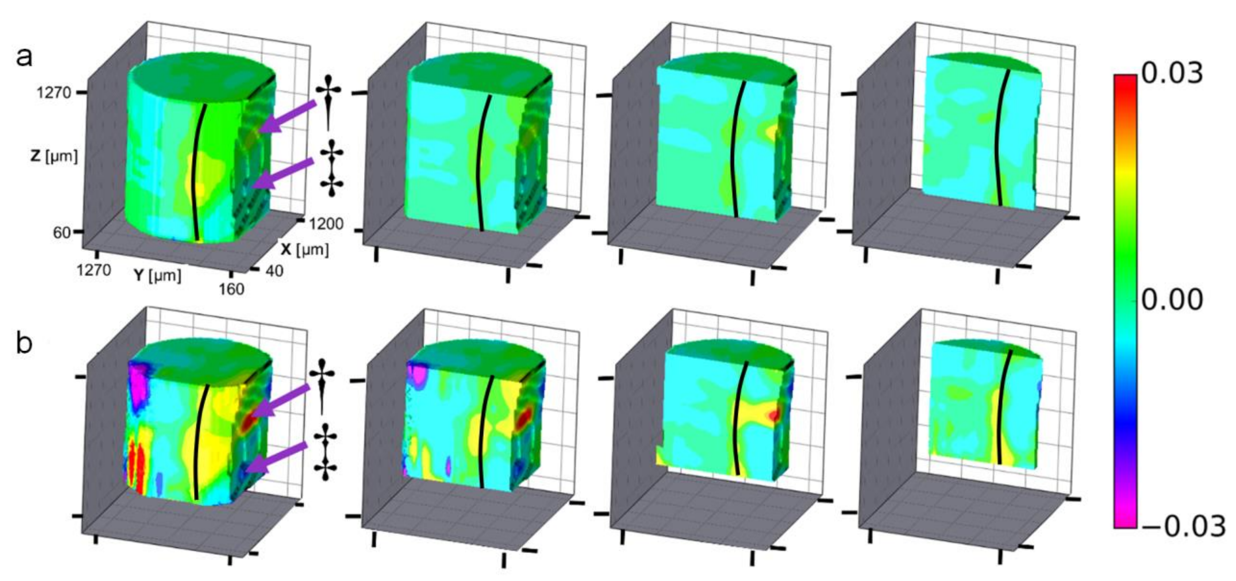

Fig. 5.9. Calculated shear strain ε_{yz} at (a) 22 MPa and (b) 44 MPa compression. Shear strain concentrations on the rivet hole surface are marked with (†) and (‡)

5.3. Microstructural influence on deformation mechanisms

Deformation of initially vertical lines (marked A, B and C) in the stir zone is summarized in Fig. 5.10, where the three lines were analyzed at identical depths from the rivet hole surface. By comparing axial deformation with position, a measure of local stiffness was obtained at these three regions using linear regression of the axial deformation data at 44 MPa compressive load (colored circles). These data showed that the metal particles altered the stiffness of the three lines: material near lines B and C were stiffer than material near line A by factors of $E_B/E_A = 1.05$ and $E_C/E_A = 1.21$. Additionally, the local stiffness of line A changed with Z coordinate, which was higher large Z coordinates ($Z_A > 800$ μm) than lower coordinates ($Z_A < 600$ μm) due to the presence of large metallic particles (bright blue spots in Fig. 5.10a). These relationships suggested local mechanical properties did indeed vary with microstructure, and that assumptions of homogeneity were invalid at local length scales; specifically, material near line C was strengthened by large metal inclusions.

Lateral deflection in Y direction of initially vertical lines A, B, C in (Fig. 5.10c) showed variation in deformation that also corresponded with local metal volume fraction. Since lateral deflection away from the bulk material would be indicative of buckling, variation with respect to microstructure would suggest that buckling was partially controlled by microstructure. The parabolic trend of lines A and C, which were partially strengthened by metal inclusions, were consistent with global bending behavior and resembled the bulk material deformation, while curvature in line B suggested localized buckling distinct from global bending behavior. Importantly, the deformation of line B in the circled region opposed both the rivet hole's natural curvature and the applied bending moment, consistent with the model presented in Fig. 5.2. Given the reduced stiffness of material near line B, the decreased buckling load was consistent with predictions by the model.

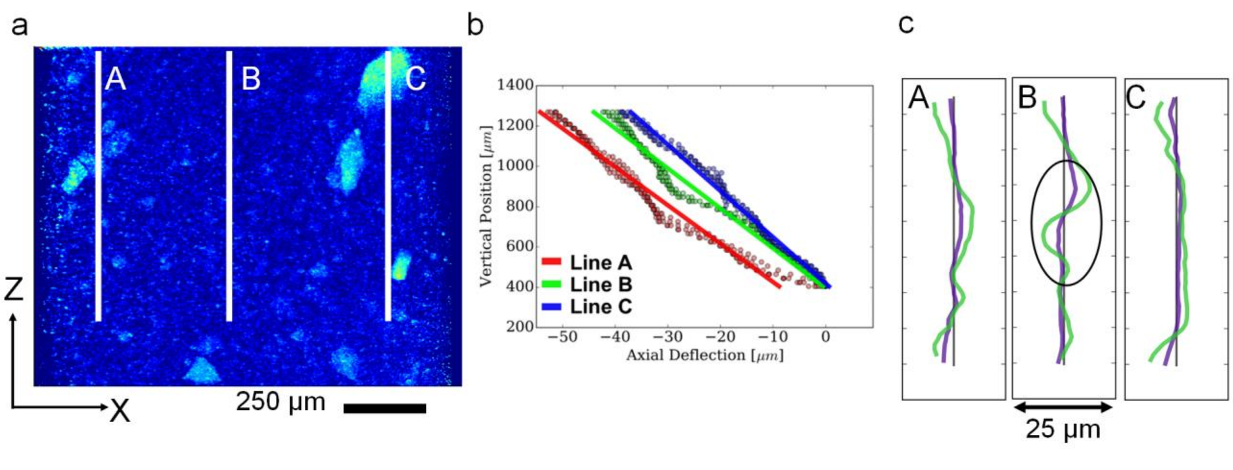

Fig. 5.10. Variation of buckling behavior throughout stir zone. (a) Selection of initially vertical lines in the stir zone at (A) X= 205 µm, (B) 615 µm, and (C) 1070 µm overlaid on map of metal volume fraction; (b) Axial deformation at 44 MPa load at subsets near lines A, B and C, with solid lines representing lines of best fit on the sampled data, represented by colored circles; (c) Y-axis deflection at lines A, B and C in the stir zone at 22 MPa (purple lines) and 44 MPa load (green lines).

Following this observation, it was anticipated that failure would similarly occur due to locally high, bending-induced stresses on the buckled stir zone surface, which was indeed demonstrated in Fig. 5.11a. The curvature of line B in Fig. 5.10c increased with further compression load, and fracture at the apex of curvature was observed in the 68 MPa image. Without local buckling, this location would have been under strong compression forces and would not have fractured in tension. Moreover, regular curvature demonstrated by material near line B demonstrated a wavelength of approximately 250 µm, which was accurately captured using the constrained buckling model (Section 2). In Fig. 5.10c, the model was applied to deformation data near line B using bulk elastic modulus data to approximate stir zone properties, and least-squares methods to optimize the coefficients of the buckling model (A and B in Eq. 5.1). These results confirmed the presence of partially constrained buckling, and support the plausibility of the proposed model.

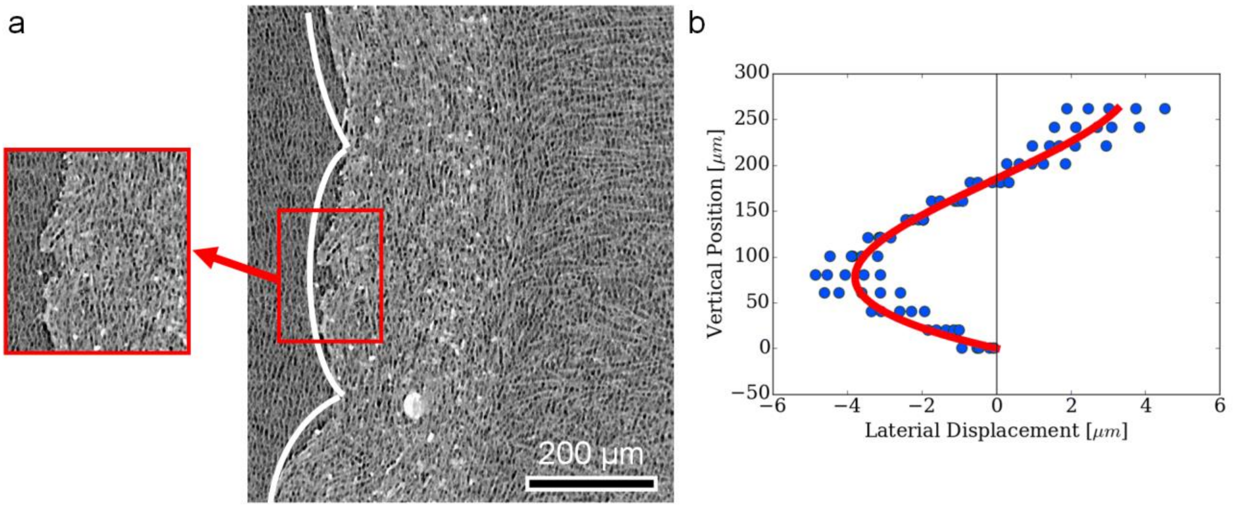

Fig. 5.11. Evidence of constrained buckling model within the stir zone, with data sampled near line B in Fig. 5.10.(a) Demonstration of stir zone buckling and kinking (traced in white) at 400 N load, with fracture at the apex of local buckling (red inset). (b) Application of this model (red line) closely corresponds with observed deformation (blue circles).

6. Finite element simulation of experiment

6.1. Model development

To aid interpretation of the coupled XCT and DVC results, a simplified model of the experiment was simulated using the finite element method (ANSYS R16.0) to evaluate general trends such as strain concentrations, interfacial strains and combined axial-bending deformation response. The two-dimensional, plane-strain FE model (Fig. 5.12a) captured the specimen geometry using a quadrilateral mesh. The model height was 20 mm, and the gage length cross section was $2.25\ mm$ in thickness. The calculations assumed linear elastic, isotropic material behavior; anisotropic effects due to fiber orientation, nonuniform distributions of fibers, porosity and metal inclusions were beyond the scope of this study.

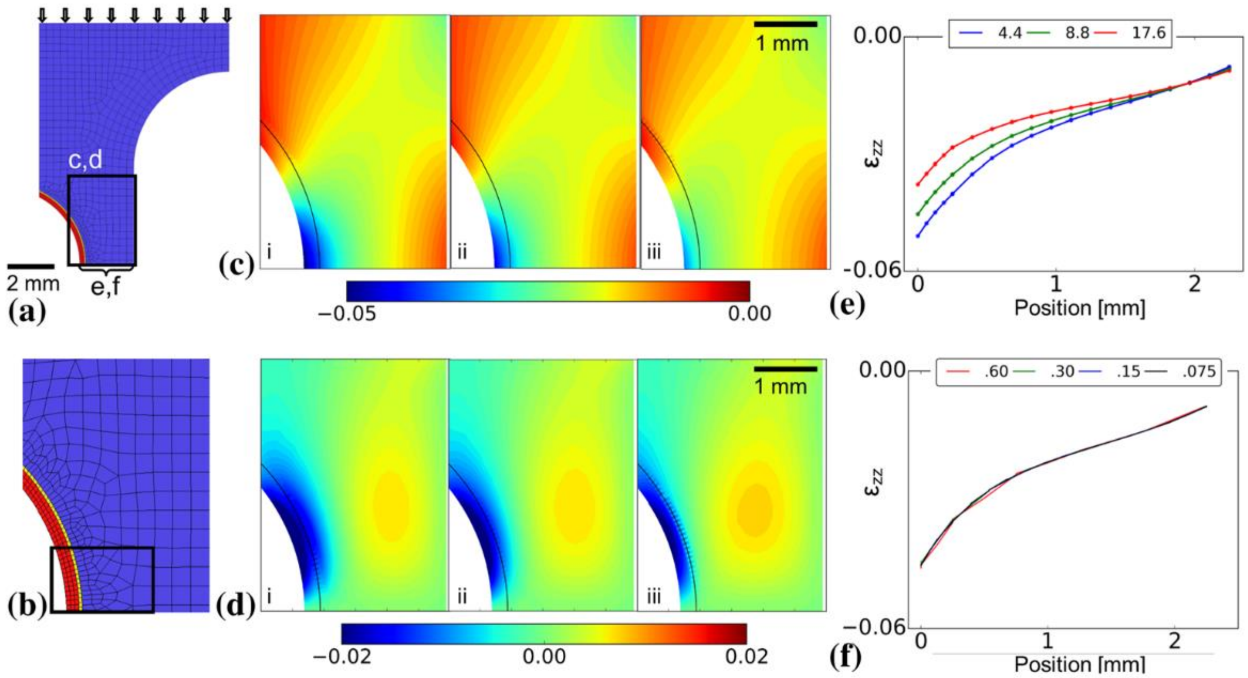

Fig. 5.12. Summary of FE simulations of FSBR compression experiment. (a) Detail of discretized model, with box indicating regions of portrayed data. (b) Magnified view of mesh near the stir zone, with box demarcating the DVC region of interest. (c) Summary of axial strain values ε_{zz} along sample midplane for stir zone stiffness of (i) 4.4 GPa, (ii) 8.8 GPa and (iii) 17.6 GPa. (d) Summary of shear strain values γ_{yz} along sample midplane for stir zone stiffness of (i) 4.4 GPa, (ii) 8.8 GPa and (iii) 17.6 GPa. (e) Extracted axial strain values along path indicated in (a) for different stiffnesses. (f) Summary of model convergence, showing axial strain along path indicated in (a)as a function of element size (in mm). The location of the stir zone is demarcated in (c-d) using a black arc.

The sample geometry incorporated separate volumes for the stir zone and bulk material such that mechanical properties in the 250 µm thick stir zone could be altered independently. The stir zone was further divided into three regions, including an interface layer of 50 µm thickness adjacent to the bulk material, and two symmetric halves of 200 µm thickness. In this sense, both compliance at the interface as well as nonuniform stiffness in the stir zone (*e.g.,* due to metallic particles) could be studied. The interfaces between all regions were assigned a no-slip contact condition. Where possible, symmetry in the sample height was enforced. Uniform axial compression of 0.15 mm was applied to the top and bottom surface of the specimen to produce strains similar in magnitude to experimental results.

To assess convergence, the model initially assigned an elastic modulus of 8.8 GPa (Table 5.1) and Poisson's ratio of $\nu = 0.40$ to both the stir zone and bulk material volumes; these properties were determined from experimental testing on bulk CFRP, and a sensitivity study found that the deformation response was insensitive to changes in Poisson's ratio over a range of 0.30 to 0.45. The convergence study used an initial mesh with nominal element size of 0.60 mm that was refined three times to a nominal element size of 0.075 mm; the finest mesh included 4 elements through the stir zone thickness. Convergence was assessed along the sample midplane marked in Fig. 5.12a. Results shown in Fig. 5.12f indicated minimum axial strains of $\varepsilon_{zz} = -0.045$ for all mesh sizes, revealing that a mesh size of 0.60 mm had already produced a converged answer. However, it was determined that this mesh size was too coarse to extract local strain gradients within the stir zone, so the fully refined mesh with element size of 0.075 mm in the stir zone was used for subsequent analysis.

6.2. Model results

Using the refined mesh, the influence of relative stiffnesses of the stir zone to the bulk material was measured. The objective of this analysis was to identify characteristic features of the strain fields that could be used to deduce the relative stiffnesses of the stir zone and bulk materials from DVC results, which strongly influenced the buckling of the stir zone. The elastic modulus of the stir zone was varied from 4.4 GPa to 17.6 GPa, while the elastic modulus of the bulk material was maintained at 8.8 GPa; thus, relative stir zone stiffnesses of 0.5, 1.0 and 2.0 were studied. The Poisson's ratio of each volume remained 0.40. Geometry and boundary conditions remained identical to those used in the convergence study.

Axial strain ε_{zz} results from this calculation are presented in Fig. 5.12c, while in-plane shear strain γ_{yz} results are summarized in Fig. 5.12d. As indicated in Fig. 5.12b, the DVC volume of interest was smaller still than the plots in Fig. 5.12c-d.

At a high level, these results demonstrated similar strain gradient patterns for each stir zone stiffness, including relatively low compression in the bulk material and higher compression in the stir zone. Trends in both axial and shear strains matched experimental DVC measurements (Figs. 5.8 and 5.9), which showed both combined axial-bending loads and shear strain concentrations on the rivet hole surface. The magnitude of both axial and shear strains within the stir zone decreased with increasing stir zone stiffness, and the decrease in deformation within the stir zone was offset by slight increases in deformation on the opposite face of the bulk material. This result, of course, may be rationalized in that a stiffer material would deform less for identical loads. In terms of interpreting DVC results, a stiffer stir zone material would result in diminished bending gradients throughout the scanned volume. Similarly, smaller shear strain concentrations would indicate a stiffer stir zone.

This subtle difference in experimental strain fields would be difficult to discern without a control sample to serve as a reference strain field, as shown in Fig. 5.12e. Axial strain values were sampled at nodes along the intersection of the two planes of symmetry, which quantified differences in strain fields due to variation in stir zone stiffness (shear strain values were not reported, as they were uniformly trivial due to symmetry conditions). The maximum difference in axial strain between models with stir zone stiffnesses of 4.4 GPa and 17.6 GPa was $\Delta\varepsilon_{zz} = 0.013$, which was similar to the sensitivity of DVC techniques. Although the variation in axial strains was small, this visualization supported the observation that a stiffer stir zone would inhibit bending deformation since the average slope of the strain gradients flattened with increasing stir zone stiffness.

Increasing stir zone stiffness resulted in diminished peak compressive strains, although the decrease in strain was less than the proportional increase in stiffness; for explicitness, the nondimensional loading factor $\sigma_{zz}/E_{stir\ zone}$ increased with stiffness. For example, a doubling of stir zone modulus from 4.4 GPa to 8.8 GPa resulted in a change in axial strain from $\varepsilon_{zz} = -0.045$ to -0.051, or a factor of only 1.12; assuming a linear elastic material response, this amplified the nondimensional loading ratio by a factor of 1.12. Because buckling models (*e.g.*, Eqs. 5.1 and 5.2) are governed by this same nondimensional loading parameter, this relationship implied that stiffer stir zones were more likely to buckle. The presence of stiffening features within the stir zone such as metal inclusions, increased fiber volume and fiber reorientation would further reduce the critical buckling load of the stir zone.

A key difference between the FE simulation with uniform stir zone stiffness and experimental results was the absence of a shear strain concentration at the interface between the stir zone and bulk materials. While the previous simulation assumed no-slip conditions at this interface, the actual specimen likely contained some level of compliance at this boundary. In addition, the experimental interfacial shear strain was asymmetric, with nonzero shear obtained at the sample midplane. The causes of the interfacial shear strain were tested by increasing interfacial compliance and imposing asymmetric stiffnesses in the stir zone; results are summarized in Fig. 5.13. First, the interfacial subvolume (yellow in Fig. 5.13a) was assigned a stiffness of 4.4 GPa while the remaining portions of the stir zone and bulk material were assigned a stiffness of 8.8 GPa. In a second simulation, the top half of the stir zone (red in Fig. 5.13a) was assigned a reduced stiffness of 6.6 GPa and the interfacial region a stiffness of 4.4 GPa, while the stiffness of other subvolumes remained unchanged. In both simulations, the axial strain distribution (Fig. 5.13b) closely resembled results from models without a compliant interface; in the asymmetric model the maximum axial compression increased from $\varepsilon_{zz} =$

-0.045 to $\varepsilon_{zz} = -0.051$, a difference that was smaller than DVC sensitivity. In the asymmetric model, nonzero shear strain of $\gamma_{yz} = 0.012$ was observed near stir zone / bulk material interface (Fig. 5.13c), which closely agreed with experimental results. Surprisingly, the symmetric model with compliant interface resulted in decreased interfacial shear strain. Additional asymmetric simulations without the compliant interface showed no interfacial shear concentration.

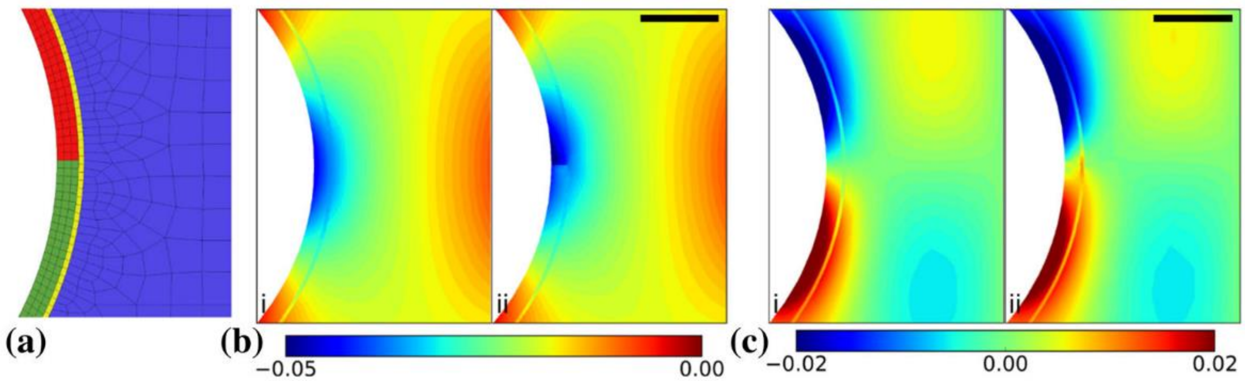

Fig. 5.13. Simulation of shear strain concentration at stir zone / bulk material interface using asymmetric stir zone stiffnesses. (a) Detail of mesh near stir zone, showing compliant interface (yellow) and stir zone subvolumes (red and green). Stiffness in the interface and two stir zone subvolumes were separately manipulated. (b) Axial strain ε_{zz} for model with (i) compliant interface and (ii) compliant interface and asymmetric stir zone stiffness. (c) Shear strain γ_{yz} for model with (i) compliant interface and (ii) compliant interface and asymmetric stir zone stiffness. Scale bar in (b) and (c) is 1 mm.

Based on these results, it was concluded that the interaction of a compliant interface and asymmetric stiffness in the stir zone contributed to the interfacial shear strain concentration. The assumed stiffnesses in these simulations varied from bulk properties by a factor of 2, which could easily be achieved by the heterogeneous distribution of constituents observed in Fig. 5.6. For instance, the asymmetric stir zone stiffness could be caused by nonhomogeneous distribution of stiff metal inclusions as observed in Fig. 5.6, while interfacial compliance could be caused by poor interfacial bonding, increased porosity or low volume fraction of reinforcement.

7. Discussion

7.1. *Modeling of 3D deformation mechanisms with coupled XCT and DVC*

The detection and measurement of localized buckling within the stir zone, as well as calculation of spatially variable mechanical properties, demonstrated the utility of combined XCT and DVC methods, as this deformation could not have been accurately detected with traditional two-dimensional measurement techniques. Specifically, surface measurements could neither distinguish the independent deformations of the stir zone and bulk materials nor identify that buckling was constrained to areas away from rigid aluminum inclusions within the stir zone. Moreover, surface measurement would be hindered by small specimen size and unusual curved geometry. Postmortem cross-section analysis could identify microstructural differences but not elastic deformation. In contrast, sample preparation for XCT analysis was greatly simplified, and the combined XCT and DVC experiment provided much more quantitative data than otherwise possible.

The composite deformation was sensitive to local microstructure. The 250 μm thick stir zone demonstrated distinct behavior compared to the adjacent bulk material, despite nominally similar material compositions. Rather, differences in fiber orientation and porosity contributed to somewhat compliant interface between the stir zone and bulk material and enabled the stir zone to deform uniquely from the bulk material. Even within the stir zone, deformation was dictated by the location of aluminum inclusions, and local buckling demonstrated in the experiment would be difficult to model with bulk material measurements, or even traditional rule-of-mixtures models based on stir-zone measurements. These measurements suggested that assumptions of material homogeneity broke down due to material processing, as local microstructure and deformation mechanisms varied from bulk properties and behavior. In this case, microstructural variation led to unusual buckling deformation that was very different from global behavior. Outside of friction stir processes, one could expect similar heterogeneities due to turbulent flow patterns during injection molding of chopped fiber composites or due to cyclical friction loading, which is well known to reorient molecular chains in polymers.

While direct measurement of stir-zone mechanical properties was precluded by the complex geometry and microstructure, comparison with FE models provided some insight into stir zone properties. In particular, the sample demonstrated only a mild strain concentration near the rivet hole surface due to a bending load, and the sample was absent of widespread shear strain concentration in the stir zone. These findings were consistent with FE simulations containing a stiff stir zone compared to the bulk material, suggesting that the increased fiber volume fraction and metal inclusions locally stiffened the stir zone.

The most glaring difference between experimental and FE simulation results was the presence of shear strain at the stir zone / bulk material interface. Examination of XCT reconstructions did not reveal visible crack opening displacement at the interface. Since the FE model imposed a no-slip condition at this location, the most likely cause of this shear stress would be a compliant interface between the stir zone and bulk materials. With respect to FSBR joint performance, the weak interface could hinder effective load transfer between the rivet and CFRP workpieces.

7.2. Application of DVC to other fiber composites

For the first time, DVC was used to study the deformation of fiber composites by employing fibers as intrinsic markers for displacement calculation, unlike prior DVC efforts that studied materials with either high-contrast additives (*e.g.*, ceramic particles in metal matrix composite [16]) or porous structures. This expands the types of materials that can be studied by DVC to include fiber-reinforced composites.

7.3. Failure characterization of FSBR CFRP joints

It is clear from the fiber orientation and composition measurements that the stir zone had a very different microstructure compared to the bulk material. These changes were caused by intense thermal and mechanical loads in the FSBR process, and must be accounted in mechanical modeling of the FSBR failure process.

From the finite element results and the buckling model, it is clear that any change to the stir zone stiffness compared to the bulk material can alter the failure behavior. These changes were difficult to deduce from the DVC results, since the any change in axial strain would be similar in magnitude to the DVC measurement error. Similarly, this information could not be obtained from inspection of the microstructure: both fiber reorientation as well as metal inclusions in the stir zone would increase the stiffness, but would also be diminished from the increased porosity.

Still, the DVC results and buckling behavior were qualitatively consistent with increased stiffness in the stir zone. In particular, stiffening effects due to aluminum inclusions locally reduced the axial deformation and inhibited buckling compared adjacent pockets of “pure” CFRP material. Since these inclusions were not uniformly distributed throughout the stir zone, the sample demonstrated heterogeneous deformation behavior. Thus, the buckling behavior may be most strongly influenced by the heterogeneous microstructure in the stir zone.

8. Conclusions

Combined XCT and DVC in conjunction with *in situ* mechanical testing were performed on engineered fiber reinforced polymer composites, which enabled accurate, high resolution measurement of local mechanical response in three dimensions. Unique deformation mechanisms such as internal shear and microstructure-dependent local buckling were observed *in situ*, which could not have been detected with traditional two-dimensional measurement techniques. The following conclusions are made:

- Intrinsic microstructural features such as fibers, pores and metal inclusions enabled accurate volumetric strain calculation of dense polymer matrix fiber composites using DVC without the need for high-contrast additives. This method may also be applicable to emerging non-polymer matrix composites with low phase contrast between reinforcements and matrix.
- Deformation calculated with DVC was employed to determine variation of mechanical properties within the FSBR altered stir zone microstructure, which were necessarily impossible to derive from bulk material properties.
- Material processing created a unique microstructure with distinct mechanical behavior compared to bulk material, demonstrating the limitations of extending bulk material properties to microscopic features. Combined XCT and DVC were shown to be effective tools to identify unique microstructures and local deformation behavior within composites.
- While obtaining mechanical properties of the FSBR joint's stir zone in the CFRP workpiece was precluded by complex sample geometry and microstructure, comparison with FE solutions provided some insight into stir zone properties. Experimental trends were consistent with a stiffened stir zone compared to the bulk material, which was ascribed to local increases in fiber volume and embedded metal particles. The FE model also illuminated the source of interfacial shear strain between the stir zone and bulk material, which was caused by a compliant interface and heterogeneous stiffness in the

stir zone. Finally, it was demonstrated that a stiffened stir zone was more susceptible to buckling due to nonlinear increases in compressive stress.

9. *Appendix: SEM composition analysis*

EDS analysis was used to determine the composition of metal inclusions observed in the stir zone. It was found that the most prominent peak for the small inclusions (Fig. 5.14; green circle) was zinc, and for the large inclusion (purple square) was aluminum. The likely provenance of these materials was the zinc coating on the steel rivet and the aluminum workpiece.

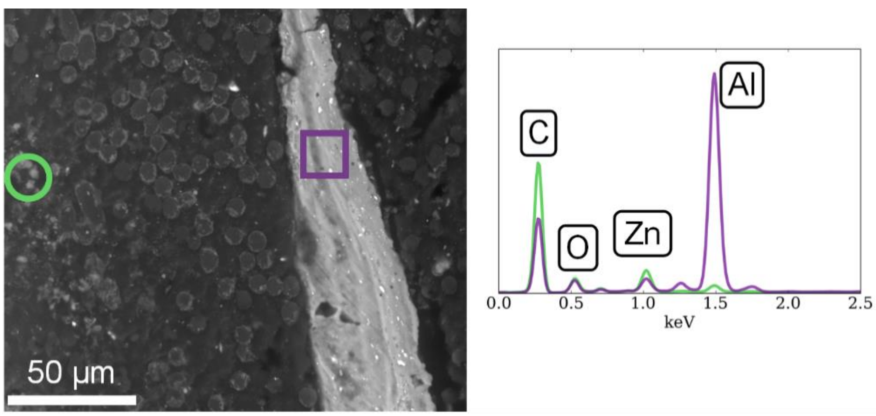

Fig. 5.14. EDS composition analysis of metal inclusions embedded in the stir zone.

10. *Appendix: Accuracy of image segmentation*

10.1. *Assessment of fiber size*

Certainly, the fiber volume and fiber orientation calculations were highly sensitive to fiber dimensions; XCT and SEM images were compared to verify that the thresholded XCT images produced realistic fiber dimensions. Fig. 5.15 compares fiber diameters measured with scanning electron microscopy and thresholded images, and suggests that the thresholded fibers have reasonably accurate dimensions.

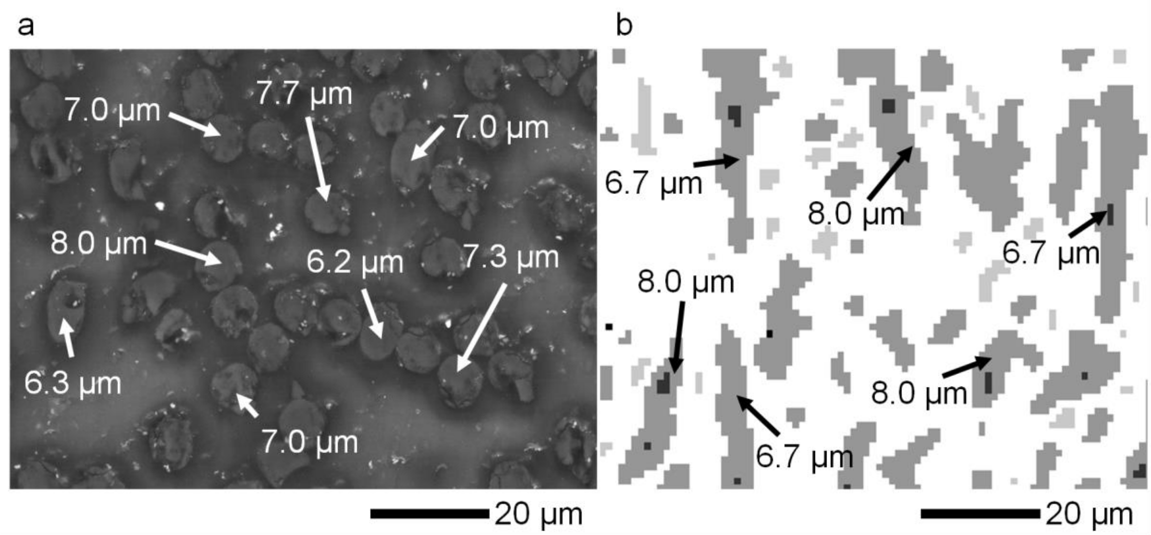

Fig. 5.15. Comparison of CFRP fiber diameters in (a) SEM image and (b) thresholded XCT scan.

10.2. SEM fiber volume vs. XCT fiber volume

A baseline measurement for fiber volume was determined from a scanning electron micrograph of the extracted rivet specimen. Intensity gradients were removed by second-order surface fitting for each region, and the flattened image was thresholded to distinguish fibers and matrix. Calculations in Fig. 5.16 revealed much higher fiber volume fraction in the stir zone than in the bulk material; these measurements closely matched with the XCT calculations presented in Section 4.1.

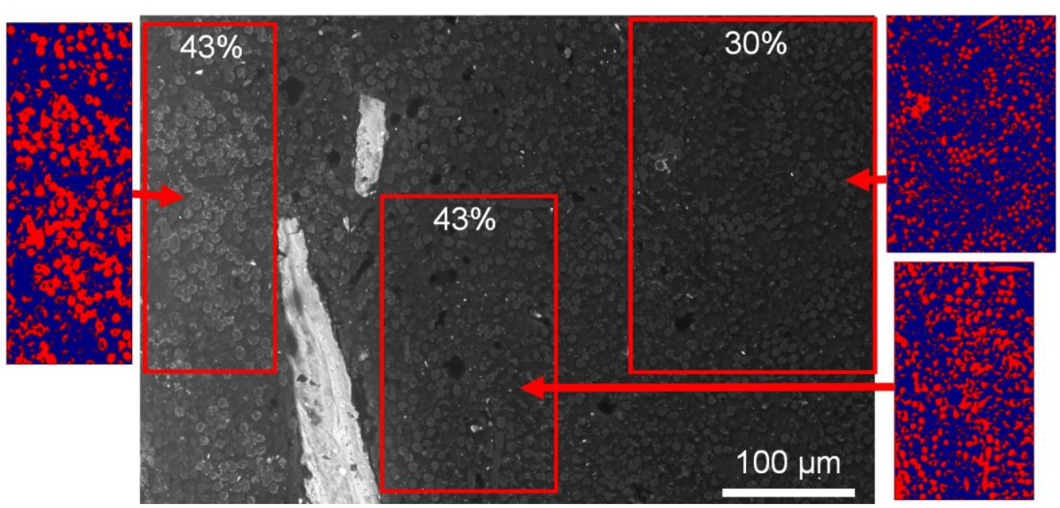

Fig. 5.16. Fiber volume fraction calculation for different CFRP zones using scanning electron microscopy. Thresholded images and fiber volume for (left) interior stir zone, (center) exterior stir zone, and (right) bulk material. Rivet hole is to left of image.

References

[1] S.M. Goushegir, J.F. dos Santos, S.T. Amancio-Filho, Friction Spot Joining of aluminum AA2024/carbon-fiber reinforced poly(phenylene sulfide) composite single lap joints: Microstructure and mechanical performance, Mater. Des. 54 (2014) 196–206. doi:10.1016/j.matdes.2013.08.034.

[2] J. Min, J. Li, Y. Li, B.E. Carlson, J. Lin, W.-M. Wang, Friction stir blind riveting for aluminum alloy sheets, J. Mater. Process. Technol. 215 (2015) 20–29. doi:10.1016/j.jmatprotec.2014.08.005.

[3] J. Min, Y. Li, J. Li, B.E. Carlson, J. Lin, Friction stir blind riveting of carbon fiber-reinforced polymer composite and aluminum alloy sheets, Int. J. Adv. Manuf. Technol. 76 (2015) 1403–1410. doi:10.1007/s00170-014-6364-8.

[4] A. Valenza, V. Fiore, L. Fratini, Mechanical behaviour and failure modes of metal to composite adhesive joints for nautical applications, Int. J. Adv. Manuf. Technol. 53 (2010) 593–600. doi:10.1007/s00170-010-2866-1.

[5] K.W. Jung, Y. Kawahito, M. Takahashi, S. Katayama, Laser direct joining of carbon fiber reinforced plastic to zinc-coated steel, Mater. Des. 47 (2013) 179–188. doi:10.1016/j.matdes.2012.12.015.

[6] S. Katayama, Y. Kawahito, Laser direct joining of metal and plastic, Scr. Mater. 59 (2008) 1247–1250. doi:10.1016/j.scriptamat.2008.08.026.

[7] M.A. Sutton, J.-J. Orteu, H.W. Schreier, Image Correlation for Shape, Motion and Deformation Measurements, Springer US, Boston, MA, 2009. doi:10.1007/978-0-387-78747-3.

[8] B.K. Bay, T.S. Smith, D.P. Fyhrie, M. Saad, Digital volume correlation: Three-dimensional strain mapping using X-ray tomography, Exp. Mech. 39 (1999) 217–226. doi:10.1007/BF02323555.

[9] E. Verhulp, B. van Rietbergen, R. Huiskes, A three-dimensional digital image correlation technique for strain measurements in microstructures, J. Biomech. 37 (2004) 1313–1320. doi:10.1016/j.jbiomech.2003.12.036.

[10] F. Hild, E. Maire, S. Roux, J.-F. Witz, Three-dimensional analysis of a compression test on stone wool, Acta Mater. 57 (2009) 3310–3320. doi:10.1016/j.actamat.2009.03.038.

[11] Y. Wang, A. Cuitiño, Full-field measurements of heterogeneous deformation patterns on polymeric foams using digital image correlation, Int. J. Solids Struct. 39 (2002) 3777–3796. http://www.sciencedirect.com/science/article/pii/S0020768302001762 (accessed January 8, 2015).

[12] H. Toda, H. Sinclair, J.-Y. Buffière, E. Maire, K.H. Khor, P. Gregson, T. Kobayashi, A

3D measurement procedure for internal local crack driving forces via synchrotron X-ray microtomography, Acta Mater. 52 (2004) 1305–1317. doi:10.1016/j.actamat.2003.11.014.

[13] S. Roux, F. Hild, P. Viot, D. Bernard, Three-dimensional image correlation from X-ray computed tomography of solid foam, Compos. Part A Appl. Sci. Manuf. 39 (2008) 1253–1265. doi:10.1016/j.compositesa.2007.11.011.

[14] R. Brault, A. Germaneau, J.C. Dupré, P. Doumalin, S. Mistou, M. Fazzini, In-situ Analysis of Laminated Composite Materials by X-ray Micro-Computed Tomography and Digital Volume Correlation, Exp. Mech. 53 (2013) 1143–1151. doi:10.1007/s11340-013-9730-9.

[15] J.C. Tan, J.A. Elliott, T.W. Clyne, Analysis of Tomography Images of Bonded Fibre Networks to Measure Distributions of Fibre Segment Length and Fibre Orientation, Adv. Eng. Mater. 8 (2006) 495–500. doi:10.1002/adem.200600033.

[16] E. Maire, V. Carmona, J. Courbon, W. Ludwig, Fast X-ray tomography and acoustic emission study of damage in metals during continuous tensile tests, Acta Mater. 55 (2007) 6806–6815. doi:10.1016/j.actamat.2007.08.043.

[17] S. Terzi, L. Salvo, M. Suéry, N. Limodin, J. Adrien, E. Maire, Y. Pannier, M. Bornert, D. Bernard, M. Felberbaum, In situ X-ray tomography observation of inhomogeneous deformation in semi-solid aluminium alloys, Scr. Mater. 61 (2009) 449–452. doi:10.1016/j.scriptamat.2009.04.041.

[18] J. Min, J. Li, B.E. Carlson, Y. Li, J. Lin, Mechanical Property of Al Alloy Joints by Friction Stir Blind Riveting, Procedia Eng. 81 (2014) 2036–2041. doi:10.1016/j.proeng.2014.10.277.

[19] Numpy Community, NumPy Reference, 1 (2011) 1–1146.

[20] M.W. Czabaj, M.L. Riccio, W.W. Whitacre, Numerical reconstruction of graphite/epoxy composite microstructure based on sub-micron resolution X-ray computed tomography, Compos. Sci. Technol. 105 (2014) 174–182. doi:10.1016/j.compscitech.2014.10.017.

[21] M.J. Emerson, K.M. Jespersen, A.B. Dahl, K. Conradsen, L.P. Mikkelsen, Individual fibre segmentation from 3D X-ray computed tomography for characterising the fibre orientation in unidirectional composite materials, Compos. Part A Appl. Sci. Manuf. 97 (2017) 83–92. doi:10.1016/J.COMPOSITESA.2016.12.028.

Chapter 6:
Quantifying the three-dimensional damage and stress redistribution mechanisms of braided SiC/SiC composites by in situ digital volume correlation

1. Introduction

While SiC fiber-reinforced, SiC matrix ceramic matrix composites (SiC/SiC CMCs) have attracted great interest for their superior strength and toughness at elevated temperatures, their intrinsically brittle constituents can fracture suddenly and unpredictably. The composite's mechanical behavior is strongly influenced by irregularities in the microstructure, including porosity, nonuniform tow-tow contact and variation in tow size, placement and orientation [1,2]. These defects often lead to failure initiation within the sample interior, which hinders direct observation and quantification of the damage mechanisms. Even in cases when failure initiates at a visible surface feature, full-field deformation measurements of the exterior surfaces (*i.e.*, 3D digital image correlation; 3D-DIC) [3] are insufficient as the response still depends on the concealed, underlying structure. To unravel the complex failure mechanisms of CMCs, it is therefore desirable to obtain simultaneous three-dimensional strain and microstructural measurements of internal features before, during and after damage initiation.

Unfortunately, this is not feasible with conventional experimental approaches, so the effects of microstructural variation have been studied with "virtual experiments" using finite element simulations of experimentally-measured or statistically generated composite geometries [4,5]. Computational results are commonly compared to surface strain and damage maps obtained by 3D-DIC [3,4], but it remains unclear if the models accurately capture the internal behavior of *thick* composites, or for complex geometries with inaccessible surfaces. This concern is particularly valid for tubular nuclear cladding geometries, which commonly fail due to hoop stress on the internal surface. Therefore, new measurement techniques are required to truly validate virtual experiments.

Several test methods have been developed to evaluate the hoop strength of cylindrical samples, including internal pressurization via hydraulic fluid [6,7], or, more commonly, compression of an elastomeric insert in an "expanding plug" test [8,9]. Radial deformation u_r is typically measured on the external surface at select locations via dilatometer, which can be converted to hoop strain $\varepsilon_{\theta\theta}$ and hoop stress $\sigma_{\theta\theta}$ by the isotropic thick-walled cylinder equations,

$$u_r = \frac{P_i r}{E(r_o^2 - r_i^2)}\left[(1-\nu)r_i^2 + \frac{(1+\nu)r_i^2 r_o^2}{r^2}\right] \tag{6.1}$$

$$\varepsilon_{\theta\theta} = \frac{u_r}{r} \tag{6.2}$$

$$\sigma_{\theta\theta} = \frac{P_i}{r_o^2 - r_i^2}\left(r_i^2 + r_i^2 r_o^2 / r^2\right) \tag{6.3}$$

where r is the radial coordinate, r_i and r_o are the internal and outside radii of the cylinder, E and ν are the stiffness and Poisson's ratio of the cylinder, and P_i is the internal pressure. However, due to the *anisotropic* mechanical properties and heterogeneous microstructure of SiC/SiC CMCs as well as small number of composite layers [10], it is unclear if the through-thickness deformation profile predicted by the *isotropic* thick-walled cylinder equations remains valid; this is a key question that can be answered with volumetric deformation measurements.

One promising technique is coupled *in situ* micro-X-ray Computed Tomography (XCT) and Digital Volume Correlation (DVC) testing, which has been widely used to reveal with ~10 µm resolution the otherwise-inaccessible internal deformation/failure mechanisms of porous bone, foams and particle-reinforced composites [11–14]. Recent work by the authors have demonstrated that the contrast between fibers, pores and other microstructural features in dense fiber-reinforced polymer composites enables robust and highly sensitive DVC measurements of internal elasto-plastic deformation and microstructure-controlled buckling mechanisms [15]. The ability to correlate tomograms of polymer composites implies that similar measurement capabilities can be achieved for CMCs, especially in light of recent XCT measurements of microstructure and damage in SiC/SiC CMCs [16,17]. Indeed, coupled XCT / DVC techniques have recently been used as a benchmark for finite element simulations of deformation and damage in SiC/SiC CMCs [18,19].

2. Materials and methods

In this work, coupled XCT and DVC approaches are applied to *in situ* expanding plug tests of triaxially-braided SiC/SiC composite cladding tubes produced by a CVI process (provided by General Atomics). These specimens were in the as-fabricated condition (showing surface roughness caused by the underlying fiber architecture), and were not smoothed or polished. The composite specimens featured an axial height of 12.5 mm, an outer radius of 5.5 mm and a nominal wall thickness of 1.2 mm with 3 layers of braided tows. The fiber architecture was selected to provide similar strengths in axial and hoop directions, and resulted in a composite elastic modulus of 190 GPa in the hoop direction [7]. Using a custom loading stage (Fig. 6.1a), an incompressible Shore 95A polyurethane plug [20] was axially compressed within the sample to perform an expanding plug test; radial dilation of the plug loaded the interior surface of the specimen, contributing to deformation and failure by hoop stress.

Tomograms with 500 x 500 x 500 voxels and voxel resolution of 15.6 µm were acquired throughout the deformation of four composite samples (XRadia MicroXCT-200). While the field of view for each scan was only 7.8 mm in diameter, overlapping XCT scans recorded the mechanical response of the entire specimen at each load increment (Fig. 6.1b-c). Representative *in situ* reconstructions are shown in Fig. 6.1b-c after failure of a single tow at 2400 N and after specimen fracture at 2630 N, which clearly illustrate prominent microstructural features such as tow geometry and large voids (> 50 μm), as well as matrix microcracks and fracture surfaces. Tomograms were smoothed with a 3D Gaussian filter before correlation with commercial DVC software (Vic-Volume, Correlated Solutions), which removed noise and has been shown to improve image correlation accuracy [21,22]. In this way, the volumetric mechanical response and damage mechanisms (*e.g.,* matrix microcracking, tow failure, etc.) could be related to the underlying composite microstructure, and key questions about (1) the validity of homogeneous thick-wall cylinder elasticity assumptions, (2) tow failure mechanisms, and (3) stress redistribution could be answered.

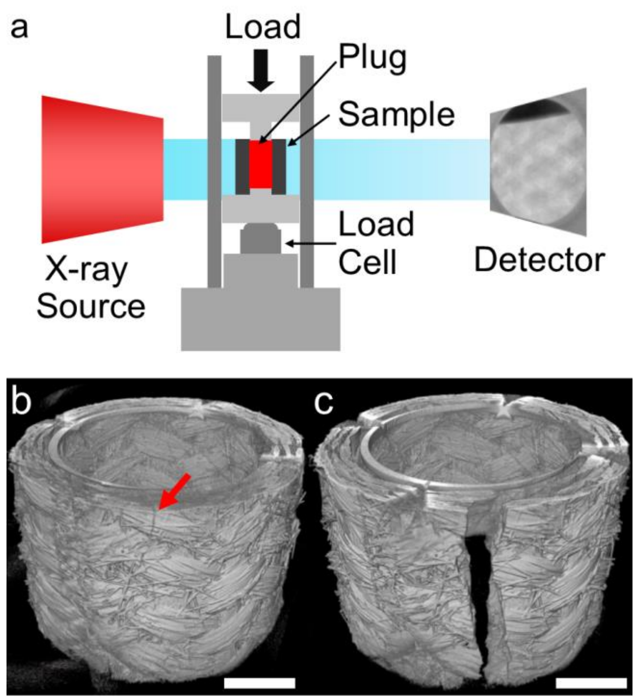

Fig. 6.1. Coupled XCT and DVC setup. (a) Experimental apparatus, showing in situ expanding plug loading stage. (b-c) Representative in situ tomograms after (b) sub-critical tow failure on exterior surface (highlighted by arrow) at 2400 N, and (c) after failure at 2630 N. The rubber plug and aluminum indenter are hidden to show interior composite microstructure. Scale bars in (b-c): 3 mm.

3. Results and discussion

Representative DVC results are presented in Fig. 6.2, which shows the hoop stress on the *interior* and *exterior* surfaces of the composite at various loads before specimen fracture at 2950 N. As evidenced by prominent strain concentrations, it is clear that mechanical response is strongly regulated by microstructure. In the pre-damage loading regime up to 2500 N, we observed localized strain concentrations of $\varepsilon_{\theta\theta} = 0.25 - 0.35\%$ that corresponded to tow crossovers on both the interior and exterior surfaces. These regions naturally exhibited the highest stress/strain response, as they distribute load between overlapping tows [23]. Strain away from contact regions was somewhat lower, $\varepsilon_{\theta\theta} = 0.15\%$, and even negative at some locations; highly heterogeneous and locally negative strains have been observed in both surface DIC measurements and associated finite element simulations of stochastic woven CMCs, and are attributed to microstructural variation and defects [24]. Some strain concentrations on the interior surface (one of which is marked by inset in Fig. 6.2c) were proximate to the location of tow failure at 2700 N, potentially indicating that failure initiated from these inter-tow contacts.

The hoop strain distributions on the interior and exterior surfaces were not strongly related; that is, the regions with highest deformation varied through the thickness. Rather, the location of strain concentrations was governed by the immediate tow architecture rather than more distant microstructural features. This was particularly true in the elastic loading regime before microstructural damage, as inferred from strain maps at 2100 and 2500 N (b and c in Fig. 6.2). A notable exception to this trend occurred after tow failure on the interior surface, which produced a large stress redistribution to tows on the exterior surface (Fig. 6.2d). Therefore, surface strain measurements were only indicative of large interior damage but were not sensitive to elastic strains on the interior surface.

Comparison of the interior and exterior strain profiles revealed that the interior surface displayed several minor hoop strain peaks away from tow-contact regions, but these were not apparent on the exterior surface. This was probably caused by boundary conditions imposed by the expanding plug. For instance, variation in local plug-composite contact stress as the elastomer conformed to the interior surface could produce highly three-dimensional and irregular loading conditions. Local loading effects were dissipated through the composite thickness via St. Venant's principle, resulting in a "cleaner" strain distribution that only showed strain concentrations at inter-tow contacts. It is possible that grinding of the interior surface to remove tow roughness or the addition of an inner monolithic SiC layer could produce a more uniform stress distribution.

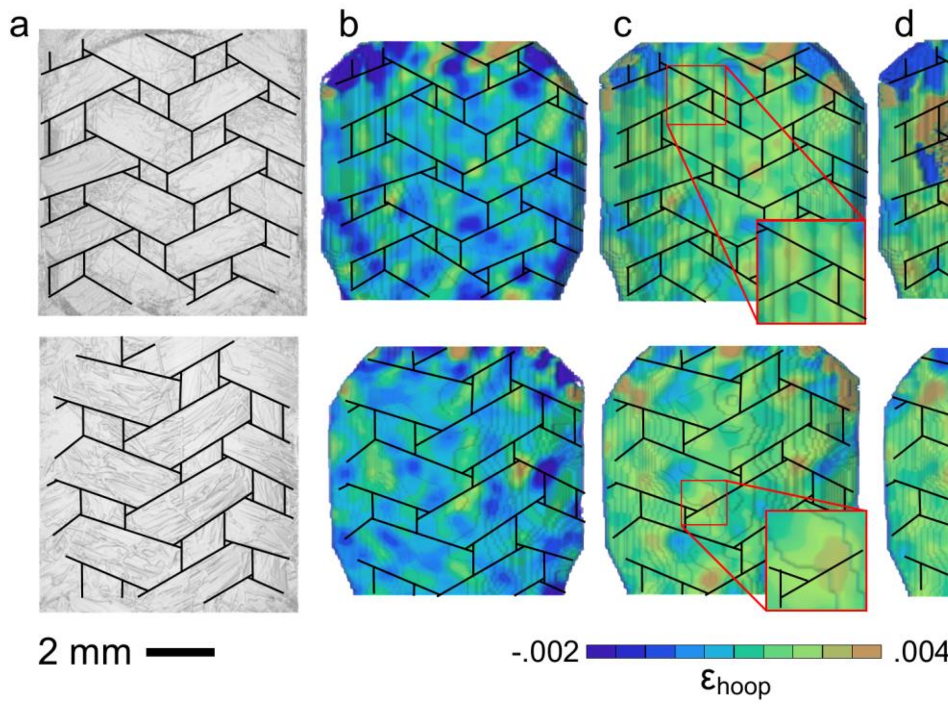

Fig. 6.2. DVC computed hoop strain $\varepsilon_{\theta\theta}$ on interior (top) and exterior (bottom) surface. (a) Tomogram at 0 N load, with tows outlined in black. (b-d) $\varepsilon_{\theta\theta}$ measurements acquired within the elastic regime at (b) 2100 N and (c) 2500 N, and (d) after interior tow failure at 2730 N, which appears as levels of high strain. The specimen failed completely at 2950 N. Prominent strain concentrations at 2500 N are highlighted by inset.

Although it was clear that the microstructure contributed to elevated strains at the tow overlaps, why did failure initiate at the particular location? How did failure propagate from the damaged tow? Detailed inspection of the tow architecture in Fig. 6.3 identified a large inter-tow spacing of $0.86\ mm$ at the point of failure initiation, which was 25-60% larger than in similar regions. Based on this, we could expect an increased length of biased tow that was not supported by underlying material. The radial pressure exerted by the elastomeric plug resulted in the maximum bending moment at the tow overlap, analogous to the stress distribution on a cantilever beam (Fig. 6.3b). In this scenario, the maximum principal stress – the relevant failure criteria for brittle SiC constituents – would occur at the root of the biased tow, which was indeed where tow failure occurred. This natural stress concentration was enhanced by the increased unsupported length and by load transfer at the tow contacts. Although the small specimen size restricted the number of tow-spacing measurements, these results suggested that tow spacing must be tightly controlled to produce a uniform mechanical response. Further experiments are required to quantify the specific contribution of tow spacing to failure compared to other defects such as porosity, tow misorientation and variable matrix thickness.

Analysis of the fracture surface of a different specimen (Fig. 6.3c) confirmed that this fracture mechanism prevailed along the entire interior surface. The jagged fracture path along the interior surface connected nearly all points of contact with underlying axial or biased tows (Fig. 6.3d). In each of the four samples, the fracture path was constrained between two axial tows, and the cracks never bridged an axial tow on the interior surface to propagate laterally; this indicated that the axial tows fully arrested and/or deflected the propagating cracks, and that failure was dominated by hoop stress. In addition, the fractured samples exhibited microcracks parallel to the final fracture surface (Fig. 6.3c-d) with similar crack deflection characteristics. While it could not be confirmed whether these cracks formed before, during or after sample rupture, SEM and XCT measurements revealed that the supplemental microcracks only appeared within 3 mm of the final fracture surface, suggesting that their initiation was closely related to the fracture process. Therefore, it was believed that the elevated hoop stresses that contributed to sample rupture also created parallel microcracks through a crack bridging mechanism.

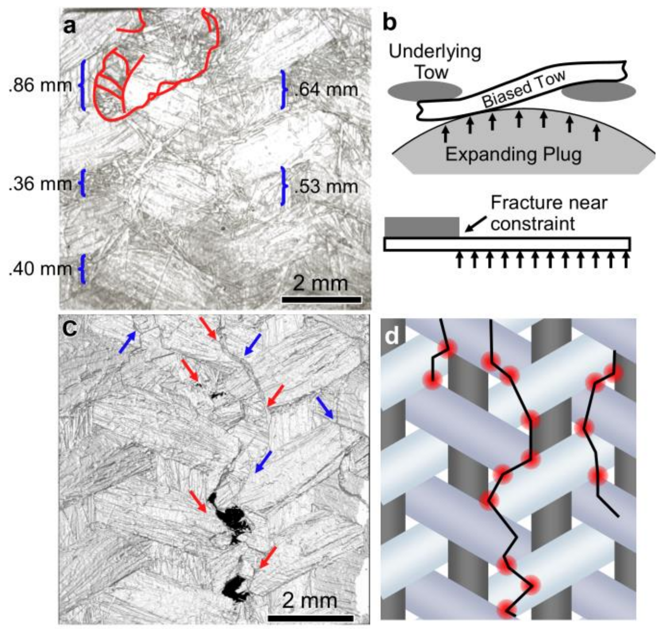

Fig. 6.3. Tow failure is regulated by microstructural variation. (a) Measurements of inter-tow spacing. The tow fracture pattern (evident as region of large hoop strain in Fig. 6.2) is traced in red for clarity. (b) Schematic of biased tow failure mechanism. (c) Fracture pattern on interior surface (different specimen), showing biased tow failure at overlap with axial tows (red arrows) and other biased tows (blue arrows). (d) Schematic of fracture and microcrack paths visible in (c), showing alignment with tow overlaps (highlighted in red).

With new insight into the mechanisms of subcritical tow failure, we now seek to understand the redistribution of stress around damaged regions. The damage observed in Fig. 6.3 was constrained to the interior layer, leaving two intact layers of load-bearing tows outside the damaged region. Analysis of the hoop strain in two regions before and after tow fracture revealed complex deformation and nonuniform stress redistribution behavior (Fig. 6.4). Before tow fracture, the average strain in regions “b” and “c” at 2100 N closely resembled the theoretical profile predicted by Eqs. 6.1-6.3 (dashed line in Fig. 6.4b-c), yet the two regions demonstrated unique variations in hoop strain on the interior surface. At 2100 N, region "b" exhibited a range from $\varepsilon_{\theta\theta}^{2.5\%} = 0.02\%$ to $\varepsilon_{\theta\theta}^{97.5\%} = 0.23\%$ (strains at 2.5$^{\text{th}}$ and 97.5$^{\text{th}}$ percentiles) on the interior surface, compared to a range of $\varepsilon_{\theta\theta}^{2.5\%} = -0.10\%$ to $\varepsilon_{\theta\theta}^{97.5\%} = 0.35\%$ in region "c". The large variation in region "c" was indicative of widespread microcracking, as crack opening displacements would create large pseudo-strains and simultaneously unload adjacent material to create small strains.

After tow fracture at 2730 N, the hoop strain evolved differently in the two regions, supporting a conclusion of anisotropic stress redistribution. In both regions, the average (through-thickness) hoop strain increased to a value of $\varepsilon_{\theta\theta}^{avg} = 0.163\%$, which constituted a relatively larger increase in region "c" than in region "b" and suggested that stress was preferentially redistributed axially rather than radially. The average strain increased uniformly through the thickness in region "c", which maintained a deformation gradient consistent with Eqs. 6.1-6.3. In contrast, the average strain increased preferentially on the outside of region "b", resulting in a uniform strain distribution that varied little with radial position. As a result, both the average and maximum values of $\varepsilon_{\theta\theta}$ on the interior surface were higher in region "c" than in region "b", and these values in region "c" approached the critical fracture strain for individual tows [25]. Subsequent loading to 2950 N resulted in fracture propagation along the axial direction, consistent with this analysis.

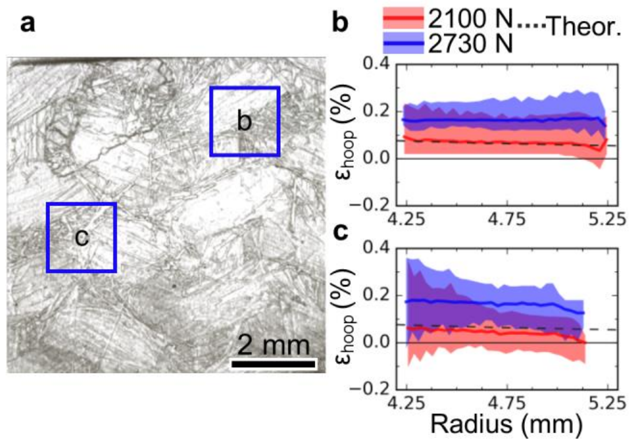

Fig. 6.4. Stress redistribution associated with tow failure. (a) Tomogram of Specimen 4 after failure of interior tow. (b-c) DVC measured through-thickness hoop strain at loads before and after tow failure corresponding to regions (b) to right and (c) beneath failed tow. Dark colored lines represent mean strain response, while colored bands encapsulate 95% of strain measurements. Data is compared to theoretical hoop strain at 2100 N via thick-wall cylinder equations (dashed line). Radial thicknesses of the two regions are different due to microstructural variation.

4. Conclusions

In conclusion, coupled XCT / DVC measurements of *in situ* expanding plug tests provided unprecedented access to the internal deformation and failure mechanisms of SiC/SiC composites. This new experimental technique achieved quantitative tow-level strain measurements, which were cross-referenced to high-resolution 3D microstructural images to elucidate the processing-microstructure-deformation-failure relationships of as-fabricated braided SiC/SiC composites. These measurements revealed key differences between internal and external deformation trends, and found that surface-based measurements only rarely corresponded to internal strain distributions. Rather, the strain distribution and failure of the braided composite was most strongly predicted by the local tow architecture. Comparison between strain distributions, composite microstructure and failure mechanisms confirmed that large local tow spacing increased peak strain at adjacent inter-tow contacts and facilitated composite failure, which implies that tight control of tow alignment is necessary for good composite-level mechanical properties. These novel measurements revealed that tow failure at inter-tow contacts was the primary damage mechanism for this particular braided tow architecture, which was facilitated by load transfer between tows and stress distributions analogous to cantilever beams. Based on these measurements, tow spacing is believed to strongly influence the failure properties of braided SiC/SiC composites.

Finally, the current technique provides meaningful one-to-one comparison for FE simulations of statistically-generated composite models, and is therefore anticipated to be an essential tool for model validation. The coupled XCT/DVC approach successfully captured the nonlinear deformation, damage, stress redistribution and failure characteristics of braided CMCs, which is the central objective of virtual experiments. Since tow failure initiated on the sample interior, and DVC measurements suggested that exterior measurements were not sensitive to *internal deformation and damage*, these results prove that surface-based measurements (as from 3D-DIC, etc.) are insufficient experimental benchmarks for the simulations. Although results were only demonstrated for four samples, and further testing is required to assess the robustness of DVC measurements, the results indicate that three-dimensional XCT-based measurements are suitable and essential to validate FE models for thick, multi-ply composites.

References

[1] H. Bale, M. Blacklock, M.R. Begley, D.B. Marshall, B.N. Cox, R.O. Ritchie, Characterizing Three-Dimensional Textile Ceramic Composites Using Synchrotron X-Ray Micro-Computed-Tomography, J. Am. Ceram. Soc. 95 (2012) 392–402. doi:10.1111/j.1551-2916.2011.04802.x.

[2] M.N. Rossol, T. Fast, D.B. Marshall, B.N. Cox, F.W. Zok, Characterizing in-plane geometrical variability in textile ceramic composites, J. Am. Ceram. Soc. 98 (2015) 205–213. doi:10.1111/jace.13275.

[3] V.P. Rajan, M.N. Rossol, F.W. Zok, Optimization of Digital Image Correlation for High-Resolution Strain Mapping of Ceramic Composites, Exp. Mech. 52 (2012) 1407–1421. doi:10.1007/s11340-012-9617-1.

[4] B.N. Cox, H.A. Bale, M. Begley, M. Blacklock, B.-C. Do, T. Fast, M. Naderi, M. Novak, V.P. Rajan, R.G. Rinaldi, R.O. Ritchie, M.N. Rossol, J.H. Shaw, O. Sudre, Q. Yang, F.W. Zok, D.B. Marshall, Stochastic Virtual Tests for High-Temperature Ceramic Matrix Composites, Annu. Rev. Mater. Res. 44 (2014) 479–529. doi:10.1146/annurev-matsci-122013-025024.

[5] R.G. Rinaldi, M. Blacklock, H. Bale, M.R. Begley, B.N. Cox, Generating virtual textile composite specimens using statistical data from micro-computed tomography: 3D tow representations, J. Mech. Phys. Solids. 60 (2012) 1561–1581. doi:10.1016/j.jmps.2012.02.008.

[6] K. Mosley, The stressing for test purposes of materials in tubular form using elastomeric inserts—experimental and theoretical development, Arch. Proc. Inst. Mech. Eng. 1847-1982 (Vols 1-196). 196 (1982) 123–139. doi:10.1243/PIME_PROC_1982_196_014_02.

[7] L.H. Alva, X. Huang, G.M. Jacobsen, C.A. Back, High Pressure Burst Testing of SiCf-SiCm Composite Nuclear Fuel Cladding, in: H. Jin, C. Sciammarella, S. Yoshida, L. Lamberti (Eds.), Adv. Opt. Methods Exp. Mech. Vol. 3 Proc. 2014 Annu. Conf. Exp. Appl. Mech., Springer International Publishing, 2015: pp. 387–393. doi:10.1007/978-3-319-06986-9_46.

[8] T.S. Byun, E. Lara-Curzio, R.A. Lowden, L.L. Snead, Y. Katoh, Miniaturized fracture stress tests for thin-walled tubular SiC specimens, J. Nucl. Mater. 367–370 A (2007) 653–658. doi:10.1016/j.jnucmat.2007.03.014.

[9] H. Jiang, J.A.J. Wang, Methodology for mechanical property testing of fuel cladding using an expanding plug wedge test, J. Nucl. Mater. 446 (2014) 27–37. doi:10.1016/j.jnucmat.2013.11.026.

[10] Q.D. Yang, K.L. Rugg, B.N. Cox, D.B. Marshall, Evaluation of Macroscopic and Local Strains in a Three-Dimensional Woven C/SiC Composite, J. Am. Ceram. Soc. 88 (2005) 719–725. doi:10.1111/j.1551-2916.2005.00156.x.

[11] E. Maire, P.J. Withers, Quantitative X-ray tomography, Int. Mater. Rev. 59 (2014) 1–43. doi:10.1179/1743280413Y.0000000023.

[12] J.Y. Buffiere, E. Maire, J. Adrien, J.P. Masse, E. Boller, In Situ Experiments with X ray Tomography: an Attractive Tool for Experimental Mechanics, Exp. Mech. 50 (2010) 289–305. doi:10.1007/s11340-010-9333-7.

[13] B.K. Bay, T.S. Smith, D.P. Fyhrie, M. Saad, Digital volume correlation: Three-dimensional strain mapping using X-ray tomography, Exp. Mech. 39 (1999) 217–226. doi:10.1007/BF02323555.

[14] E. Verhulp, B. van Rietbergen, R. Huiskes, A three-dimensional digital image correlation technique for strain measurements in microstructures, J. Biomech. 37 (2004) 1313–1320. doi:10.1016/j.jbiomech.2003.12.036.

[15] B.P. Croom, W.-M. Wang, J. Li, X. Li, Unveiling 3D Deformations in Polymer Composites by Coupled Micro X-Ray Computed Tomography and Volumetric Digital Image Correlation, Exp. Mech. 56 (2016) 999–1016. doi:10.1007/s11340-016-0140-7.

[16] H.A. Bale, A. Haboub, A.A. MacDowell, J.R. Nasiatka, D.Y. Parkinson, B.N. Cox, D.B. Marshall, R.O. Ritchie, Real-time quantitative imaging of failure events in materials under load at temperatures above 1,600 °C, Nat. Mater. 12 (2013) 40–46. doi:10.1038/nmat3497.

[17] D. Frazer, M.D. Abad, D. Krumwiede, C.A. Back, H.E. Khalifa, C.P. Deck, P. Hosemann, Localized mechanical property assessment of SiC/SiC composite materials, Compos. Part A Appl. Sci. Manuf. 70 (2015) 93–101. doi:10.1016/j.compositesa.2014.11.008.

[18] L. Saucedo-Mora, M. Mostafavi, D. Khoshkhou, C. Reinhard, R. Atwood, S. Zhao, B. Connolly, T.J. Marrow, Observation and simulation of indentation damage in a SiC-SiCfibre ceramic matrix composite, Finite Elem. Anal. Des. 110 (2016) 11–19. doi:10.1016/j.finel.2015.11.003.

[19] L. Saucedo-Mora, T.J. Marrow, Multi-scale damage modelling in a ceramic matrix composite using a finite-element microstructure meshfree methodology, Philos. Trans. R. Soc. London A Math. Phys. Eng. Sci. 374 (2016). doi:10.1098/rsta.2015.0276.

[20] G.M. Jacobsen, J.D. Stone, H.E. Khalifa, C.P. Deck, C.A. Back, Investigation of the C-ring test for measuring hoop tensile strength of nuclear grade ceramic composites, J. Nucl. Mater. 452 (2014) 125–132. doi:10.1016/j.jnucmat.2014.05.002.

[21] P. Mazzoleni, F. Matta, E. Zappa, M.A. Sutton, A. Cigada, Gaussian pre-filtering for uncertainty minimization in digital image correlation using numerically-designed speckle patterns, Opt. Lasers Eng. 66 (2015) 19–33. doi:10.1016/j.optlaseng.2014.08.004.

[22] B. Pan, Bias error reduction of digital image correlation using Gaussian pre-filtering, Opt. Lasers Eng. 51 (2013) 1161–1167. doi:10.1016/j.optlaseng.2013.04.009.

[23] M.N. Rossol, V.P. Rajan, F.W. Zok, Effects of weave architecture on mechanical response of 2D ceramic composites, Compos. Part A Appl. Sci. Manuf. 74 (2015) 141–152. doi:10.1016/j.compositesa.2015.04.003.

[24] M. Blacklock, J.H. Shaw, F.W. Zok, B.N. Cox, Virtual specimens for analyzing strain distributions in textile ceramic composites, Compos. Part A Appl. Sci. Manuf. 85 (2016) 40–51. doi:10.1016/j.compositesa.2016.02.030.

[25] C. Chateau, L. Gélébart, M. Bornert, J. Crépin, D. Caldemaison, C. Sauder, Modeling of damage in unidirectional ceramic matrix composites and multi-scale experimental validation on third generation SiC/SiC minicomposites, J. Mech. Phys. Solids. 63 (2014) 298–319. doi:10.1016/j.jmps.2013.09.001.

Chapter 7: Summary and recommendations

In this dissertation, coupled *in situ* X-ray Computed Tomography (XCT) mechanical testing and Digital Volume Correlation (DVC) measurement techniques are extended to study the damage mechanisms of glass microballoon (GMB) reinforced syntactic foams with elastomer matrices, fiber-reinforced polymer, and ceramic-matrix composites. While the microstructures in these composites contain many fiducial markers that are theoretically amenable to accurate displacement measurements, they violate commonly held beliefs that speckle patterns for DVC measurements should be high-contrast, random, isotropic, and durable; the fiber-reinforced composites and syntactic foams violate the principles of isotropy and durability, respectively. Instead, I have demonstrated that these assumptions can be relaxed in certain scenarios without sacrificing measurement accuracy. The validated XCT/DVC technique is subsequently used to quantify the interactions between microstructure and damage mechanics in these three types of composites, whose internal deformation was previously inaccessible with conventional metrology.

1. Key contributions

In Chapter 2, the accuracy of DVC for fragile specimens was proven using error analysis of both experimental and numerically-generated images, with the goal of validating the use of DVC for fragile specimens such as syntactic foams and brittle composites. These measurements showed that both displacement and strain error were proportional to the severity of degradation in the material's microstructure: Below a critical level of degradation, displacement and strain error remained near a noise floor of $0.05\ voxels$ and $100\ \mu\varepsilon$, respectively. Above this threshold, error rapidly increased to unacceptable levels exceeding above 0.2 voxels and $10{,}000\ \mu\varepsilon$. For low levels of damage, the error due to speckle pattern degradation was insignificant compared to other sources of error, including image noise and distortion. This transition occurred after 30% to 40% of all speckles in the image disappeared. These analyses support the use of DVC to study the deformation mechanisms in syntactic foams, which previously was believed to be impossible due to violation of the principle of grayscale conservation.

In Chapter 3, *in situ* XCT compression and the newly-validated DVC technique was used to quantify the damage mechanisms in syntactic foams with elastomer matrices. High-resolution tomograms revealed that both the initiation and propagation of GMB collapse depended on the local clustering of GMBs, leading to the formation of pseudo-crush bands in the composite. The dispersed, weakly localized damage behavior in syntactic foams with elastomer matrices contrasted strongly localized damage behavior in syntactic foams with rigid thermoset matrices. This unique damage mechanism produced bands of axial strain variation that grew to several millimeters in length as revealed by DVC. A new mechanism based on stress redistribution around collapsed GMBs was proposed to explain the damage propagation, which was supported by finite element analysis and successfully captured the effects of cluster orientation on the observed damage.

In Chapter 4, the *in situ* XCT / DVC approach was used to further study the role of GMB volume fraction and particle clustering on the internal damage mechanisms of elastomer-matrix syntactic foams. Image processing and digital volume correlation techniques identified very different damage mechanisms compared to syntactic foams with brittle matrices. In particular, the mechanism seamlessly transitioned from dispersed GMB collapse at low volume fraction to clustered GMB collapse at high volume fraction. Moreover, damage initiated and propagated earlier in closely-packed regions for all specimens. Statistical analysis of GMB damage also identified a consistent, inverse relationship between the probability of survival and the local coordination number ($N_{neighbor}$) across all specimens. While damage is shown to increase with both the GMB volume fraction and $N_{neighbor}$, these trends are somewhat independent: in other words, syntactic foam models must incorporate effects of both global volume fraction and local particle clustering.

The validity of these techniques was also proven for the first time in anisotropic materials using friction-stir processed polymer-matrix composites in Chapter 5 and later in braided ceramic matrix composite tubes in Chapter 6. These measurements demonstrated high spatial resolution and strain sensitivity, and were able to detect localized damage in context of key microstructural features. DVC is therefore shown to provide accurate deformation measurements in anisotropic and fragile microstructures, which expands the class of materials suitable for DVC measurement to include a wide variety of composites. For instance, DVC shear-strain maps revealed a strain concentration at the stir zone / bulk material interface in the FSBR-processed composite sample, indicating a weakened interface between the two regions. Similarly, analysis of the CMC tube loaded via expanding plug showed elevated hoop strain at tow-crossover locations in the CMC, which is indicative of matrix cracking at these locations. This provides experimental confirmation of elevated damage at tow-crossovers in a variety of CMC materials. In both materials, the strain hot spots were detected at low loads, and were able to forecast specimen failure at higher loads. In the PMC, bands of axial strain variation on the rivet hole surface corresponded with the wave-like buckling pattern of the stir zone. However, superposition of the deformation on the microstructure revealed that the buckling was locally controlled by 100 μm metallic inclusions embedded in the composite. Similarly, the fracture of a tow in the CMC occurred at one of the tow crossovers, which precipitated catastrophic failure of the composite at the next loading increment. Together, these results indicate that heterogeneous deformation initiated at low loads in these composite systems, and that DVC is an appropriate tool to detect this deformation as a precursor to damage. These measurements provide one-to-one experimental comparison to numerical calculations, and are thus an essential tool to validate numerical models.

2. Recommendations for future work

The current dissertation has developed DVC as a new quantitative, full-field deformation measurement technique to study the internal damage mechanisms composite materials. The nature of the XCT measurement technique allows direct superposition of these deformation / damage measurements on the underlying composite microstructure, permitting modeling of the intimate microstructure-processing-deformation-damage relationships in these materials. Future work in this area should focus on the following aspects of this measurement technique:

2.1. Reconciliation with standard DIC/DVC error models

This dissertation has shown that accurate DVC measurement is possible in cases of anisotropic and/or fragile microstructures, which cannot be reconciled with current models of DVC error. Initial efforts for modeling the error associated with fragile speckle patterns are presented in Chapter 2. Error analysis in this chapter introduced a concept related to the quantity of retained information in each subset after damage, which appeared to accurately predict the onset of DVC instability. In other words, accurate correlation required a minimum number of intact speckles within each subset. These results should be incorporated into existing models of DVC error. Current image correlation models cannot predict error due to fragile microstructures, since most well-regarded models look strictly at the *initial speckle geometry* and do not account for subsequent degradation to the speckle pattern. Indeed, other authors have noted similar degradation to DVC error at large deformation [1], which causes speckles to collapse. The current findings, however, were only tested for spherical speckles under limited conditions. Future work should explore the role of other speckle geometries, degradation modes and noise characteristics.

Similar efforts should be initiated for anisotropic materials. Almost all error models have been developed for DIC applications, for which it is easy to generate round, uniform and high-contrast speckles. No error model has been rigorously tested on composite-like, anisotropic speckle patterns common to DVC experiments. The error was associated with the limited image gradients along the fiber direction, so a model based on the "Sum of Subset Squared Image Gradients" (SSSIG) can conceptually effects of anisotropy [2]. However, recent analysis of carefully designed speckle patterns have shown an unaccounted error component due to speckle anisotropy [3], which cannot be accounted for in the SSSIG model.

In both of these cases, the image generation scheme presented in Chapter 2 provides a means to support the development and validation of improved DIC/DVC error models. One strategy is to numerically generate images of model anisotropic materials, as in Fig. 7.1; this volume was generated by generating 2D speckle patterns and then "extruding" the images in different directions to imitated a composite microstructure. By varying the layer thickness and orientation in proportion to the subvolume size, it will be possible to control the degree of anisotropy. Similar volumes could be manufactured with ellipsoidal rather than spherical speckles, which provides another route to control the specimen anisotropy.

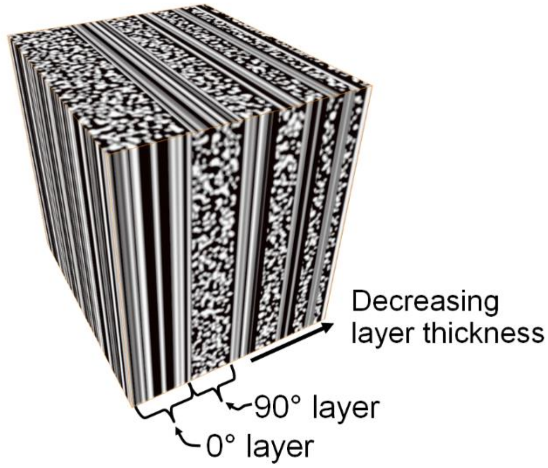

Fig. 7.1. Model system to study DVC accuracy in anisotropic solids.

2.2. Integration with finite element and micromechanics models

The enclosed experiments have unequivocally demonstrated the importance of microstructural variation on the strength and failure of composites. An alternative, non-experimental way of capturing these effects has been to develop intricate numerical models with statistically representative composite microstructures, which are enabled by advancements in massively parallel computation.

These so-called "virtual experiments" [4] generate realistic composite microstructures using experimental data, and then computationally model their mechanical behavior. The microstructural data has been provided by image-based measurements at multiple length scales, *i.e.,* to use XCT with $\sim 1\ \mu m$ resolution to resolve the unit-cell geometry of woven composites [5–7] or individual fiber trajectories in unidirectional / laminated [8–10] composites, and DIC-based measurements of long-scale structural variation at the centimeter scale [11,12]. These are integrated with mathematical descriptions of the composite architecture [13,14] to generate the numerical model.

While these models are based on realistic microstructures, it remains unclear how closely their output resembles the experimental results. In particular, the models may be affected by defects that are too small to be captured in either the images used to generate the microstructure statistics, or the microstructure generator used to produce the model. Thus, DVC is an appealing strategy to "close the loop" by providing a one-to-one comparison to the numerical results. Early efforts in this direction have been attempted using image-based computational models for braided CMC tubes [15] and woven CMC panels [16], though neither paper provided detailed an assessment of quality of virtual microstructure nor a validation of the local deformation and damage.

References

[1] A.K. Landauer, M. Patel, D.L. Henann, C. Franck, A q-Factor-Based Digital Image Correlation Algorithm (qDIC) for Resolving Finite Deformations with Degenerate Speckle Patterns, Exp. Mech. 58 (2018) 815–830. doi:10.1007/s11340-018-0377-4.

[2] B. Pan, H. Xie, Z. Wang, K. Qian, Z. Wang, Study on subset size selection in digital image correlation for speckle patterns, Opt. Express. 16 (2008) 7037. doi:10.1364/OE.16.007037.

[3] R.B. Lehoucq, P.L. Reu, D.Z. Turner, The Effect of the Ill-posed Problem on Quantitative Error Assessment in Digital Image Correlation, Exp. Mech. (2017) 1–13. doi:10.1007/s11340-017-0360-5.

[4] B.N. Cox, H.A. Bale, M. Begley, M. Blacklock, B.-C. Do, T. Fast, M. Naderi, M. Novak, V.P. Rajan, R.G. Rinaldi, R.O. Ritchie, M.N. Rossol, J.H. Shaw, O. Sudre, Q. Yang, F.W. Zok, D.B. Marshall, Stochastic Virtual Tests for High-Temperature Ceramic Matrix Composites, Annu. Rev. Mater. Res. 44 (2014) 479–529. doi:10.1146/annurev-matsci-122013-025024.

[5] H. Bale, M. Blacklock, M.R. Begley, D.B. Marshall, B.N. Cox, R.O. Ritchie, Characterizing Three-Dimensional Textile Ceramic Composites Using Synchrotron X-Ray Micro-Computed-Tomography, J. Am. Ceram. Soc. 95 (2012) 392–402. doi:10.1111/j.1551-2916.2011.04802.x.

[6] I. Straumit, S. V. Lomov, M. Wevers, Quantification of the internal structure and automatic generation of voxel models of textile composites from X-ray computed tomography data, Compos. Part A Appl. Sci. Manuf. 69 (2015) 150–158. doi:10.1016/j.compositesa.2014.11.016.

[7] F. Desplentere, S. V. Lomov, D.L. Woerdeman, I. Verpoest, M. Wevers, A. Bogdanovich, Micro-CT characterization of variability in 3D textile architecture, Compos. Sci. Technol. 65 (2005) 1920–1930. doi:10.1016/j.compscitech.2005.04.008.

[8] M.W. Czabaj, M.L. Riccio, W.W. Whitacre, Numerical reconstruction of graphite/epoxy composite microstructure based on sub-micron resolution X-ray computed tomography, Compos. Sci. Technol. 105 (2014) 174–182. doi:10.1016/j.compscitech.2014.10.017.

[9] M.J. Emerson, K.M. Jespersen, A.B. Dahl, K. Conradsen, L.P. Mikkelsen, Individual fibre segmentation from 3D X-ray computed tomography for characterising the fibre orientation in unidirectional composite materials, Compos. Part A Appl. Sci. Manuf. 97 (2017) 83–92. doi:10.1016/J.COMPOSITESA.2016.12.028.

[10] N.Q. Nguyen, M. Mehdikhani, I. Straumit, L. Gorbatikh, L. Lessard, S. V. Lomov, Micro-CT measurement of fibre misalignment: Application to carbon/epoxy laminates manufactured in autoclave and by vacuum assisted resin transfer moulding, Compos. Part A Appl. Sci. Manuf. 104 (2018) 14–23. doi:10.1016/J.COMPOSITESA.2017.10.018.

[11] M.N. Rossol, J.H. Shaw, H.A. Bale, R.O. Ritchie, D.B. Marshall, F.W. Zok, Characterizing weave geometry in textile ceramic composites using digital image correlation, J. Am. Ceram. Soc. 96 (2013) 2362–2365. doi:10.1111/jace.12468.

[12] F.M. Heim, B.P. Croom, C. Bumgardner, X. Li, Scalable measurements of tow architecture variability in braided ceramic composite tubes, J. Am. Ceram. Soc. (2018). doi:10.1111/jace.15564.

[13] M. Blacklock, H. Bale, M. Begley, B. Cox, Generating virtual textile composite specimens using statistical data from micro-computed tomography: 1D tow representations for the Binary Model, J. Mech. Phys. Solids. 60 (2012) 451–470. doi:10.1016/j.jmps.2011.11.010.

[14] R.G. Rinaldi, M. Blacklock, H. Bale, M.R. Begley, B.N. Cox, Generating virtual textile composite specimens using statistical data from micro-computed tomography: 3D tow representations, J. Mech. Phys. Solids. 60 (2012) 1561–1581. doi:10.1016/j.jmps.2012.02.008.

[15] Y. Chen, L. Gélébart, C. Chateau, M. Bornert, C. Sauder, A. King, Analysis of the damage initiation in a SiC/SiC composite tube from a direct comparison between large-scale numerical simulation and synchrotron X-ray micro-computed tomography, Int. J. Solids Struct. 161 (2019) 111–126. doi:10.1016/J.IJSOLSTR.2018.11.009.

[16] V. Mazars, O. Caty, G. Couégnat, A. Bouterf, S. Roux, S. Denneulin, J. Pailhès, G.L. Vignoles, Damage investigation and modeling of 3D woven ceramic matrix composites from X-ray tomography in-situ tensile tests, Acta Mater. 140 (2017) 130–139. doi:10.1016/j.actamat.2017.08.034.